UNIVERSITEIT VAN PRETORIA
UNIVERSITY OF PRETORIA
YUNIBESITHI YA PRETORIA
Faculty of Engineering, Built Environment and Information Technology

Investigation of a new UAV configuration with non-elliptic lift distribution

Ankit Sharma
14333288
Supervisor: Dr. Lelanie Smith
University of Pretoria
Co-supervisor: Dr. Mudassir Lone
Cranfield University

MIR-890 Dissertation

Submitted in partial fulfillment of the requirements for the degree
Masters of Engineering (Aeronautical Engineering)

in the

Department of Mechanical and Aeronautical Engineering
Faculty of Engineering, Built Environment and Information Technology

UNIVERSITY OF PRETORIA
November 2021

Abstract

Title: Investigation of a new UAV configuration with non-elliptic lift distribution

Author: A. Sharma

Student number: 14333288

Study Leader: Dr. L. Smith

Co-supervisor: Dr. M.M. Lone

The development of an alternative wing-body-tail configuration is investigated using the AREND UAV as a baseline. The proposed configuration, inspired from bird wings, assumes that all stability requirements are achieved through the main wing and there is no need for an empennage. The potential here is not only a reduction in structural weight, but also a reduction in drag that leads to an increase in fuel efficiency. This study uses the AREND wing with elliptic loading and compares its characteristics to the new wing design that has a non-elliptic lift distribution (NELD) using the method developed by Prandtl in 1933. Both the AREND and NELD wings are analysed using computational fluid dynamics to investigate the aerodynamics and flight mechanics benefits of the NELD configuration. The AREND and NELD comparison shows that the NELD configuration increases the aerodynamic efficiency by 9.87% due to the higher lift to drag ratio and the removal of the empennage. Further benefits include weight reduction and a wider CG range. A smaller wake region was also found due to the wing being fully blended with the fuselage. Upwash was seen to occur at $2y/b = 0.85$ indicating the presence of induced thrust as predicted and shown by Prandtl and the Horten Brothers. The change in lift distribution over the wing due to sideslip also shows that the NELD configuration exhibits proverse yaw and therefore, can indeed perform a coordinated turn.

Acknowledgments

I would like to convey my thanks to Dr. Lelanie Smith for allowing me considerable freedom throughout the research, for her insightful observations and motivating me to do my best.

Dr. Mudassir Lone for providing assistance, direction, and placing substantial knowledge at my disposal. The Cranfield University DSCG group, who treated me like family. I would like to express my gratitude to Estela Bragado for her research advice. Thank you to the Lone family and O'Connell's for hosting me in the United Kingdom.

I would like to thank Prof. Walter Meyer for his unwavering support throughout the years, whether it was giving me a place to stay, driving me to and from the Dr's rooms, mentoring me on my path and motivating me to be my best self. I would also like to thank Dr. Jannie Pretorius for assisting me with setting up simulations on the HPC (Department of Physics) and Prof. Rosemary Gray for storing my baggage and providing transportation to and from the Gautrain when I traveled to the United Kingdom.

I would like to thank my close friends for never giving up on me. Lastly, I would like to thank my parents and my younger brother for continuous support. This work is dedicated to my Grandfather who passed away this year.

Finally, I would like to quote Prof. Walter Meyer "By helping others, we further the opportunities and love god has bestowed upon us".

Contents

List of Figures

List of Tables

Nomenclature

AR	Aspect ratio
b	Span (m)
c	Chord (m)
$\overline{c}$	Mean aerodynamic chord (m)
c_d	Sectional drag coefficient
C_{di}	Local induced drag coefficient
C_{Di}	Induced drag coefficient
c_l	Sectional lift coefficient
C_l	Roll moment coefficient
C_L	Lift coefficient
$C_{L\alpha}$	Lift curve slope
C_m	Pitch moment coefficient
C_{mac}	Pitch moment coefficient about the aerodynamic chord
C_n	Yaw moment coefficient
c_{root}	Chord at the root of the wing (m)
c_{tip}	Chord at the tip of the wing (m)
C_Y	Side force coefficient
D	Drag (N)
D_i	Induced drag (N)
l	Length (m)
L	Lift (N)
m_0	Local lift slope
M	Bending moment (N-m)
q	Dynamic pressure (Pa)
r_P	Radius of inertia for the lift distribution (m)
S	Surface area (m^2)
t	Thickness (mm)
t/c	Thickness to chord ratio
T	Thrust (N)
U	Air speed (m/s^2)
U_x	Air speed in x direction (m/s^2)
U_z	Air speed in z direction (m/s^2)
w_i	Downwash induced by wake (m/s)
W	Weight (N)

Greek Symbols:

α	Angle of attack (deg)
α_e	Effective angle of attack (deg)
α_i	Induced angle of attack (deg)
α_{L0}	Zero-lift angle of attack (deg)
β	Side slip angle (deg)
$\gamma(TE)$	Strength of Vortex sheet at trailing edge
Γ	Circulation distribution (m^3/s)
Γ_0	Circulation at origin (m^3/s)
Γ_{max}	Maximum circulation (m^3/s)

δ	Boundary layer thickness (mm)
ε	Relative error
λ	Taper ratio
μ	Dynamic viscosity (Pa.s)
μ_l	Local dynamic viscosity (Pa.s)
μ^*	Friction velocity (m/s)
μ_P	Shape of distribution
ν	Flow velocity
ϕ	Potential flow
ρ	Air density (kg/m^3)
τ_w	Wall shear stress (Pa)
Λ	Sweep angle (deg)

Abbreviation:

AC	Aerodynamic chord
AREND	Aircraft for Rhino and ENvironmental Defense
CFD	Computational Fluid Dynamics
LE	Leading edge
LLT	Lifting line theory
LSB	Laminar separation bubble
MAC	Mean aerodynamic chord
max	Maximum
min	Minimum
NELD	Non-elliptic lift distribution
TE	Trailing edge
UAV	Unmanned aerial vehicle

1 Introduction

National Aeronautics and Space Administration's (NASA) Environmentally Responsible Aviation (ERA) project, The European Commission's New Aircraft Concepts Research (NACRE) and Clean Aviation are some well-known organizations heading research on green aircraft development. Due to growing environmental concerns the aviation industry is putting immense effort to find new configurations that are superior to the conventional configuration in terms of performance.

An alternative wing-body-tail configuration was proposed by Huyssen et al. (2012). The proposed configuration, inspired from bird wings, assumes that all stability requirements are achieved through the main wing and there is no need for an empennage (Huyssen et al., 2012). Some work has been done towards the development of the fuselage and potential revised design requirements (Smith et al., 2017, 2019), however the only work towards the wing to this date has been pilot feedback on the handling of an alternative wing (Agenbag et al., 2009). The potential here is not only a reduction in structural weight, but also a reduction in drag that leads to an increase in fuel efficiency.

The application of an alternative wing-body-tail configuration is investigated using the AREND UAV as a baseline. Project AREND, a UAV for environment and rhino defense started in 2014 and was developed and successfully flown in 2018 (Koster et al., 2016; Smith et al., 2018). Southern Africa is home to the Big 5 that include rhino and elephants. According to the Department of Environmental Affairs, South Africa has a total rhino population of approximately $20,000$ (Molewa, 2021) (more than 80% of the world's total population). Kruger National Park is home to almost 40% of the world rhino population and is protected by forest rangers. From 2007 to 2014, rhino poaching increased by 9,000% and the rhino population has decreased by 60% since 2013. On average every 22 hours a rhino is killed in South Africa (Modise, 2021; Pereira, 2021).

AREND was developed to aid in aerial surveillance to assist the park rangers in anti-poaching operations. The first iteration of AREND UAV is designed with inverted V-tail configuration which followed a conventional configuration as fuselage, wing and empennage. But removing the empennage results in an unstable UAV due to reduced directional stability. Without it, the UAV would not respond appropriately to disturbances in side-slip (Bragado Aldana and Lone, 2019).

According to Prandtl's (1933) paper, the UAV can be made stable without the tail. In the paper Prandtl talks about reducing induced drag and structural weight by having a bell shaped lift distribution through wing twist. This non-elliptic lift distribution provides proverse yaw and has positive stability effects. With the right wing twist distribution and sweep, a self stabilizing wing can be developed.

The primary motivation for the development of flying wings or tailless configurations is to create the ideal aerodynamic configuration by excluding any components not necessary for lift generation (Torenbeek, 2013). Aerodynamic efficiency may be increased by 20% to 25%, empty weight reduced, and operational expenses reduced as compared to the conventional configuration (Denisov and Bolsunovsky, 1998). Advocates of flying wing configurations say that it has the ability to eliminate the majority of parasite drag generated by the main components other than the wing, resulting in at least a 20% increase in aerodynamic efficiency in a single aircraft generation (Nickel and Wohlfahrt, 1994). The stable wing can then be combined with a low drag fuselage to produce an efficient aircraft.

The anticipated overall effect should be a reduction in empty weight and up to a 30% reduction in the amount of fuel needed to fly long distances, as well as a considerable reduction in the take-off gross weight for a certain design payload/range capability. Additionally, engines with less thrust or fewer engines may be fitted. These attributes can result in much lower operational costs (Torenbeek, 2013).

Due to limited computational resources and time, a full scale analysis will not be possible here. Thus, the AREND UAV project will be used to test this method. In this study the AREND UAV model is used to perform the CFD (computational fluid dynamics) analysis as a benchmark.

The wings with NELD (non-elliptic lift distribution) is designed and attached to the AREND fuselage without the empennage. A CFD analysis is performed and the aerodynamic and flight dynamic parameters are evaluated.

1.1 Importance of proposed work

The proposed work will be a step towards an alternative aircraft configuration that is more aerodynamically efficient. The application of this work can provide a diverse range of benefits to both aerodynamic and stability characteristics of the wing. To start with, reducing the overall induced drag improves the lift-to-drag ratio, thus increasing the aerodynamic efficiency. Moreover, the upwash created at the tips by the bell shaped lift distribution could lead to induced thrust or proverse yaw, which has the potential to enhance the controllability and flight dynamics of the aircraft achieving a coordinated flight. In addition, lift is reduced at the tips, further protecting it from flow separation, being theoretically ensured at all tapers with the bell-distribution (Bragado Aldana and Lone, 2019). All these benefits can lead to the conceptual elimination of the vertical tail, giving the possibility of tailless aircraft designs that would provide significant structural weight reduction.

1.2 Aim and Objectives

The aim of this project is to redesign the AREND UAV using Prandtl (1933) approach as the basis for wing design and to quantify potential benefits in flight dynamics and aerodynamic performance. In doing so, a tailless configuration for the AREND UAV is developed. The main objectives of this thesis are:

- Perform a literature survey on relevant phenomena and engineering processes focusing on aerodynamics, flight mechanics and aircraft design.
- A benchmark CFD study is performed on 2D and 3D wing geometries to establish CFD workflow.
- Use the CFD workflow to analyse the aerodynamic and stability performance of the AREND UAV.
- Apply Prandtl (1933) wing design approach (NELD) to develop an alternative wing that satisfies the AREND performance targets.
- Assess the aerodynamic performance along with stability characteristics of the alternative wing design relative to the original AREND configuration.

1.3 Scope

This research focused on cruise aerodynamic performance only and was limited to steady simulations in both CFD and AVL. Propeller effects were also ignored in CFD and AVL simulations. Aspects such as dynamics during manoeuvers and when the UAV is subjected to atmospheric disturbances were not assessed. Consequently, this study cannot be used as a basis for the design of airframe structure and a separate study is required to estimate potential weight benefits. Moreover, the detail design of control surfaces and flight control systems were deemed to be beyond the scope of this study.

1.4 Overview

The report is divided into the following 8 chapters:

- Chapter 1 gives a brief background of the thesis.
- Chapter 2 is the literature study where relevant information on aerodynamics, aircraft design, flight mechanics and CFD aspects are presented.
- Chapter 3 serves as a validation study for a NACA0012 airfoil and wing. Analysis is performed at comparable Reynolds number to establish the right domain and turbulence models that are used in the main study.
- Chapter 4 contains the benchmark AREND UAV CFD analysis and is used to get the aerodynamic and flight dynamic parameters which are used as requirements for NELD configuration.
- Chapter 5 forms the basis for the NELD design. It contains the requirements for the new NELD wing, airfoil selection and the Prandtl's computational code for wing design. The end result is a NELD wing with suitable wing twist distribution and sweep which is stable in AVL.
- Chapter 6 contains the CFD analysis of NELD configuration which provides the aerodynamic and flight dynamic parameters which are used for comparison.
- Chapter 7 is where a comparison is drawn up between the AREND and NELD configurations.
- Chapter 8 contains the overall conclusions of the study.

2 Literature Study

2.1 Introduction

This chapter contains an overview of aerodynamics, airfoil design and flight static stability theory specific to tailless configuration. It is written to provide the reader with the necessary background in order to understand the discussion in the later chapters. For brevity, fundamental concepts in aerodynamics are not discussed in detail and the reader is referred to Anderson's "Introduction to Aerodynamics" (Anderson Jr, 2010).

The focal point of this thesis is the flying wing and the design of its aerodynamic surface. There are no distinctions between the design processes used for developing a finite wing for a flying wing configuration and a conventional configuration. The initial proceeding consists of searching the airfoil for the desired aircraft configuration. Thereafter, the following phase refers to designing the wing geometry. The characteristics of the airfoil and wing geometry are dependent on the required configuration. Therefore, both steps of the design choices are made after taking into consideration the various aspects for the flying wing as well as the conventional configuration. The following paragraphs consist of the overall influence of specific flying wing design choices on aircraft properties.

2.2 Basic definition in Aerodynamics

The following conventional aerodynamic terms are defined as:

- Reynolds number (Re) is the ratio of inertial forces to viscous forces within a fluid calculated as follows:

$$Re = \frac{\rho U c}{\mu} \tag{2.1}$$

  where ρ is air density, U is velocity, c is the wing chord length and μ is dynamic viscosity. If $Re < 5 \times 10^5$ then the flow is considered laminar, otherwise it is turbulent (White, 2011).

- Lift (L) of an airfoil is defined as the force acting perpendicular to the direction of motion through the air and is calculated as follows:

$$L = \frac{1}{2}\rho U^2 S c_l \tag{2.2}$$

  where S represents the reference area of the wing section and c_l is sectional lift coefficient.

- Drag (D) is defined as a force acting in the opposing direction of motion. Drag is the result of friction and pressure differences in the air and is computed as follows:

$$D = \frac{1}{2}\rho U^2 S c_d \tag{2.3}$$

  where c_d is sectional drag coefficient.

- The pitching moment m (or torque) on an airfoil is created by the aerodynamic force exerted at the aerodynamic center of the airfoil is calculated as follows:

$$m = \frac{1}{2}\rho U^2 S c_m c \tag{2.4}$$

  where c_m is sectional pitching moment coefficient.

- Coefficient of Pressure (C_p) is the ratio of the difference between the local pressure and the the free stream pressure and the dynamic pressure, defined as follows:

$$C_p = \frac{P - P_\infty}{\frac{1}{2}\rho U^2} \tag{2.5}$$

  where P is pressure on wing section and P_∞ is ambient pressure.

- The center of pressure is that point on an airfoil, wing or aircraft, where the pitching moment is zero. The location of this point is not constant as a function of angle of attack, even when all the other variables remain the same.

- The aerodynamic center (AC) is that point on an airfoil or wing, where the pitching moment is independent of the angle of attack when all other variables remain the same.

2.2.1 Flow around a finite wing

For 3D wings, there is a component of flow in the spanwise direction. The pressure difference between the top and bottom surfaces create a curl around the tips. The air moves from the high pressure zone at the bottom, to the low pressure zone above. This flow produces a circulatory motion downstream of the wing, resulting in the formation of a wing-tip vortex at each wing tip as shown in Figure 2.1 (Anderson Jr, 2010).

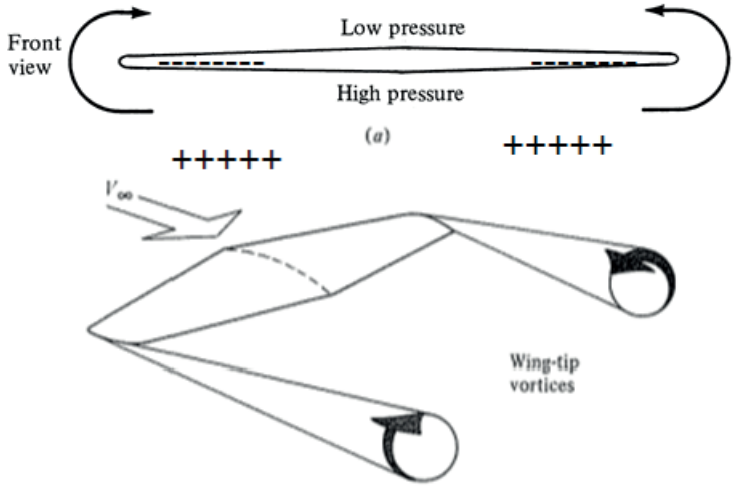

Figure 2.1: Trailing vortices on a finite wing (Anderson Jr, 2010).

By pulling the surrounding air with them, wing tip vortices generate a modest downward component of air velocity near the wing and this effect is referred to as downwash, w. The local vector of lift is shifted backwards and this results in another component acting parallel to the incoming wing; which is called induced drag (Anderson Jr, 2010).

2.2.2 Circulation and Potential Theory

The circulation theory is based on vortices. It consists of two kinds of vortices: bound and free. A vortex bounded to a body which moves relative to the flow along the body is called a Bound vortex. The bound vortex line has the same length as the body and moves against the free stream air. Therefore, creating a force on the body which is proportional to the free stream velocity (U), density of the fluid (ρ), the length (l) of the vortex and a constant circulation (Γ) of the vortex. This is defined as:

$$L = \rho U l \Gamma(y) \tag{2.6}$$

A free vortex induces a velocity on the flow around it. The induced velocity of a segment of a vortex filament can be described by the Biot-Savart Law for two points in space:

$$dU = \frac{\Gamma}{4\pi} \frac{dl \times r}{\mid r \mid^3} \tag{2.7}$$

where r is radius vector, such that:

$$U = \frac{\Gamma}{4\pi h} \tag{2.8}$$

where h is the perpendicular distance. As soon as the flow begins to circulate around the airfoil, it tends to curl around the trailing edge. Due to the very high velocity at the trailing edge, large viscous forces act on the air next to the trailing edge, resulting in the formation of a powerful vortex on the top of the airfoil, near the trailing edge. As the airfoil starts to move, a high vorticity region is pushed downstream which is known as the starting vortex. Since the circulation along a curve that includes both the vortex and the airfoil must still be zero (Helmholtz's third theorem), this leads to a counterclockwise circulation around the airfoil as shown in Figure 2.2 (Anderson Jr, 2010).

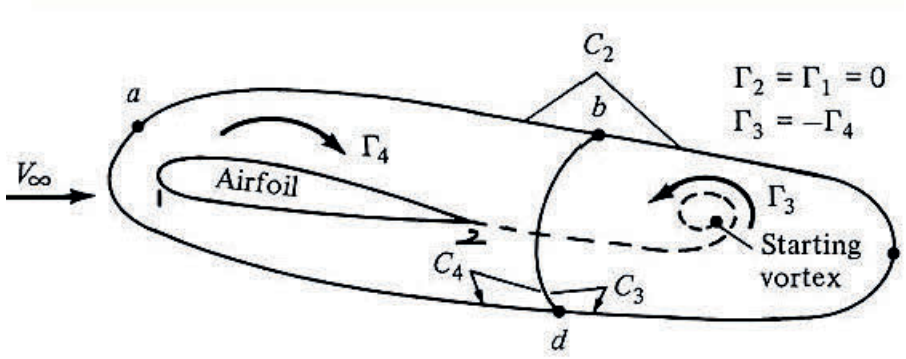

Figure 2.2: Circulation around an airfoil (Anderson Jr, 2010).

Kutta condition is applied at the trailing edge, therefore

$$\gamma(TE) = U_1 - U_2 = 0 \tag{2.9}$$

where $\gamma(TE)$ strength of vortex sheet at trailing edge, U_1 is the velocity at the top of the airfoil and U_2 is the velocity at the bottom of the airfoil. The most simple mathematical description of the vortex-distribution along the wing span is that given in Prandtl's lifting line theory (Prandtl, 1923).

2.3 Non-Elliptic Lift Distribution

2.3.1 Prandtl's Lifting Line Theory

Lifting line theory is based on the following assumptions: (1) three dimensional, (2) steady, (3) incompressible, (4) potential flow (inviscid and irrotational) with (5) high aspect ratio (AR) wing and (6) a low sweep angle (Λ). In effect it is valid for thin airfoils at low angles of attack (α) with little crossflow along the wingspan (b). In effect, local airflow is assumed to be close to two-dimensional. A vortex filament of strength Γ attached to a fixed point in a flow encounters a force $L' = \rho U \Gamma$ according to the Kutta-Joukowski theorem (Anderson Jr, 2010). The wing span is replaced with bound vortex filament extending from $y = -b/2$ to $y = b/2$. Helmholtz's vorticity theorem states that a vortex filament cannot terminate in a fluid, hence it continues as two free trailing vortices from the wing tips to infinity (Anderson Jr, 2010). This phenomenon is referred to as a Horseshoe Vortex as shown in Figure 2.3.

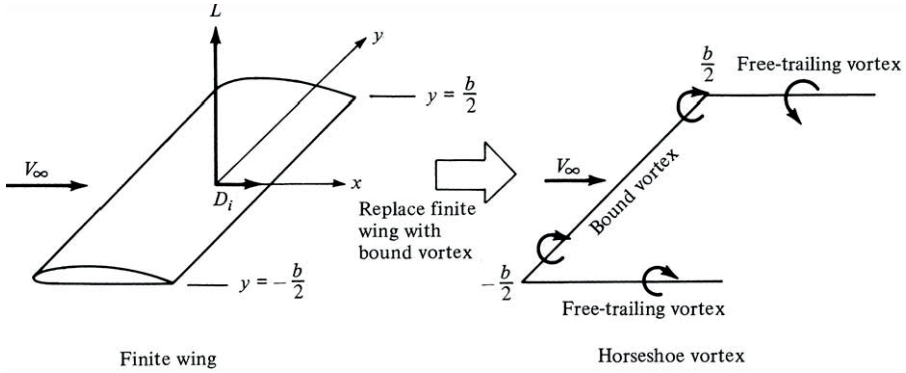

Figure 2.3: Horseshoe vortex (Anderson Jr, 2010).

The lifting line theory is based on the concept of representing a wing as a collection of horseshoe vortex lines as shown in Figure 2.4. Here, each have a distinct length of bound vortex but all converge on a single line. This is referred to as a lifting line and there is no limit to the number of horseshoe vortices that may be superimposed along it (Anderson Jr, 2010).

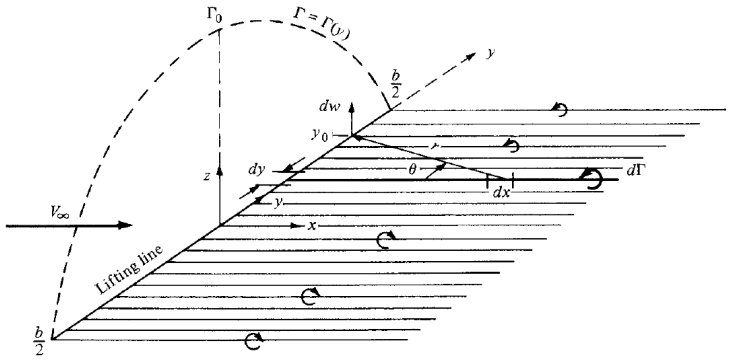

Figure 2.4: Lifting line (Anderson Jr, 2010).

Now consider a continuous distribution with $\Gamma = \Gamma(y)$, and $\Gamma = \Gamma_0$ at the origin. The trailing vortices have merged into a single vortex sheet (parallel to U). The vortex strength around the wing is zero as it is composed of a pair of trailing vortices which are equal in strength but opposite in direction. $d\Gamma = (d\Gamma/dy)dy$ is the change in circulation over dy and the strength of trailing vortex at y must equal the change in circulation $d\Gamma$ along the lifting line (Anderson Jr, 2010). Consider any point y_0 along the lifting line segment dx, this will induce a velocity at y_0 which

is given by Biot-Savart law. Velocity dw at y_0 induced by the entire semi-infinite trailing vortex at y is:

$$dw = -\frac{\left(\frac{d\Gamma}{dy}\right) dy}{4\pi\,(y_0 - y)} \tag{2.10}$$

Total velocity induced (w) at y_0 by the entire trailing vortex sheet can be found by integrating from –$b/2$to $b/2$ (Anderson Jr, 2010):

$$w = -\frac{1}{4\pi}\int_{-b/2}^{b/2} \frac{\left(\frac{d\Gamma}{dy}\right)}{(y_0 - y)} dy \tag{2.11}$$

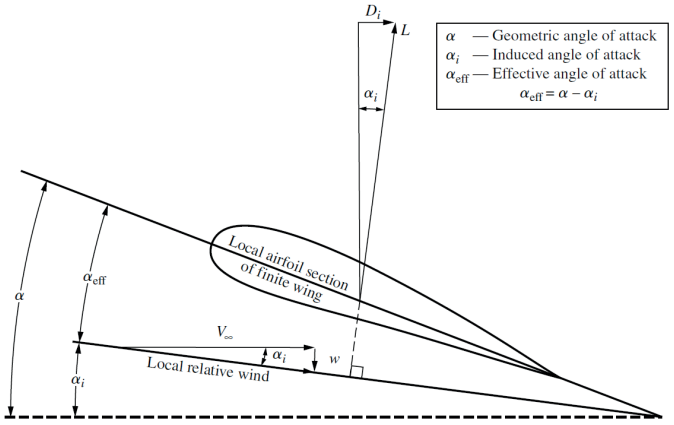

Figure 2.5: Induced downwash (Anderson Jr, 2010).

The induced angle of attack, α_i as shown in Figure 2.5 can be computed as:

$$\alpha_i = \frac{-w_i(y)}{U} \tag{2.12}$$

For an elliptical wing the downwash is given by:

$$w_i = -\frac{\Gamma_0}{2b} \tag{2.13}$$

and the induced angle of attack is:

$$\alpha_i = \frac{\Gamma_0}{2bU} \tag{2.14}$$

Using Kutta-Joukowski theorem we get:

$$L = \frac{\pi}{4} b\rho U\Gamma_0 \tag{2.15}$$

$$\alpha_i = \frac{1}{2bU} \times \frac{2USC_L}{\pi b} = \frac{SC_L}{\pi b^2} \tag{2.16}$$

where C_L is the lift coefficient. Now, assuming $sin(\alpha_i) = \alpha_i$, then induced drag (D_i) is:

$$D_i = L\alpha_i \tag{2.17}$$

$$C_{Di} = \frac{C_L^2}{\pi eAR} \tag{2.18}$$

where e is the oswald factor. In conclusion, an elliptical lift and circulation distribution has the lowest induced drag coefficient (C_{Di}). This is the lowest induced drag at the same condition as any other wing planform with the same wingspan and area. For an untwisted wing, this lift-distribution is achieved by an elliptical planform. This finding illustrates that when aspect ratio increases, the induced drag reduces. With these new variables, the C_L can be rewritten as:

$$C_L = \frac{2\pi}{\frac{2}{AR} + 1}(\alpha - \alpha_{L0}) = C_{L\alpha}(\alpha - \alpha_{L0}) \tag{2.19}$$

where α_{L0} zero-lift angle of attack and $C_{L\alpha}$ is the three-dimensional wing lift slope, which decreases with b (an increase in b leads to a decrease in AR) as shown in the Figure 2.6. For a two-dimensional wing or an infinite wing, this variable is equal to 2π.

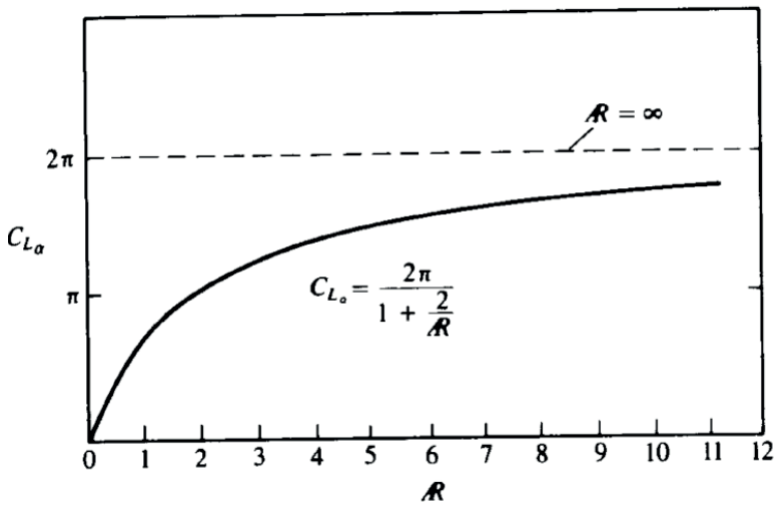

Figure 2.6: Variation of the lift curve slope against aspect ratio for thin elliptic wing (Katz and Plotkin, 2001).

For a three-dimensional finite wing, as the effective angle of attack α_e is reduced by the induced angle of attack α_i, more incidence is required to achieve the same C_L if b increases, as shown in the Figure 2.7.

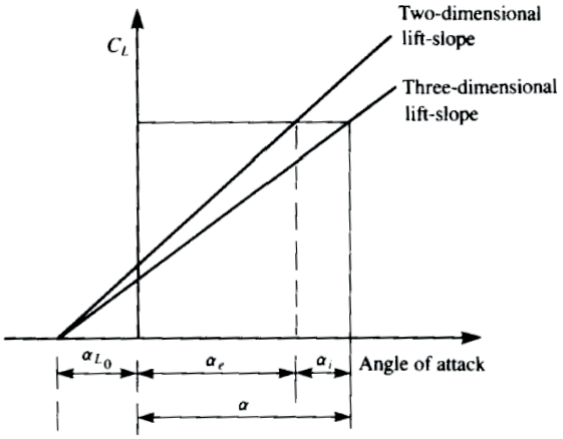

Figure 2.7: Reduction of the lift slope for three- dimensional wings (Katz and Plotkin, 2001).

2.3.2 Prandlt's Alternative for the Elliptical Spanload (1933)

The elliptic lift distribution on a wing has been considered most efficient thus far, as it provides minimum induced drag. Some fundamental assumptions were made by Prandtl, of which the most important one was the fact that the span must be specified and restricted in advance to obtain an optimal result. This conclusion was based on a constrained design space since the design of an aircraft is not always limited by a span restriction (Prandtl, 1932, 1935). On the other hand, it is also true that certain restrictions must be made to the span to avoid excessive structural weight. Hence, there is a valid span range in which it is possible to optimize the design while minimizing the induced drag.

A first approximation to this matter could pose the idea of another design methodology where the weight of the structural parts equal to the lift is specified, and this is used to seek a wing planform that reduces the total drag to a minimum (Prandtl, 1935). However, this would require a great number of variables to be solved. Thus, Prandtl proposed a simpler solution to this approach, where a rational result for the span is obtained through the added predetermination of the moment of inertia of the lift Lr_P^2 , together with the lift of the wing. In this case, r_P being the radius of inertia of the lift distribution. The moment of inertia is obtained by assuming that the weight of the spars at every point is proportional to the bending moment M acting at that point, where the spar section is considered constant along its length, and the weight of the web negligible compared to that of the angle. Another assumption must be made, where $\int_{-b/2}^{b/2} = Mdy$ is limited for the wing too. Thus maintaining the weight within reasonable limits. Using the Kutta-Joukowski theorem, Prandtl defines an expression for induced downwash as:

$$w_i = \rho \int (\Gamma w dy) \tag{2.20}$$

The fact that the radius of inertia r must have a defined value implies that the mean chord dimension must be definite too. However, the shape of the wing tips remain undetermined. Now, the variable problem can be solved by stating the lift distribution procedure that has to be applied. Then, the optimisation can be performed, where a minimum solution is found within a permissible range for the arbitrary span value with the requirement of minimum drag possible. The solution to the first step is found by A. Betz's theory, where it is stated that it is allowed to apply a variation of a secondary wing rather than to the case wing itself. This auxiliary wing is placed backwards at a distance where its reaction forwards is negligible, and which is also subjected to a downwards velocity $2w$. Hence, if the required circulation is $\Gamma(y)$, any variation of w_i must disappear with the addition of this variation, which complies with Helmholtz's theorem. This satisfies the secondary conditions stated above. Following, the condition where the variations of lift, moment of inertia of lift, and induced downwash are equal to zero must be stated.

$$\delta L = \int \delta \Gamma dy = 0$$

$$\delta \left(Lr_P^2 \right) = \int \delta \Gamma y^2 dy = 0$$

$$\delta w_i = 2 \int (\delta \Gamma w dy) = 0$$

And a typical solution for a differential equation for the downwash, w is proposed to satisfy this conditions

$$w = c_1 + c_2 y^2 \tag{2.21}$$

With this, a solution is found for the circulation, that corresponds to the solution of w referring back to Prandtl's early paper (Application of Modern Hydrodynamics to Aeronautics

(Prandtl, 1923)). Here, the circulation is defined as a series expansion and with this, the value for the constants in w is found and the problem is solved such that:

$$\mathit{\Gamma} = \left(\Gamma_0 + \mathit{\Gamma}_2\xi^2\right)\sqrt{1-\xi^2} \tag{2.22}$$

where ξ is equivalent to $y = b/2$. Next step is to find the optimum value for the circulation parameters in this solution, which must be consistent with the conditions of the problem. Defining a ratio $\mu_P = -\Gamma_2/\Gamma_0$ between these two circulation parameters, it can be applied with the constants solved previously, and to the secondary conditions. Now, dividing these expressions, the radius of inertia r_P or the span b can be found as follows:

$$b = 4r_P\sqrt{\frac{1-\mu_P/4}{1-\mu_P/2}} \tag{2.23}$$

Introducing the span into the lift equation, an expression of the circulation Γ_0 can be obtained. Furthermore, equating w and this final expression for circulation, the parameterized expression for the induced downwash w_i is found as follows:

$$w_i = \frac{L^2}{8\pi\rho U^2 r_P^2}\frac{(1-\mu_P/2)\left(1-\mu_P/2+\mu_P^2/4\right)}{(1-\mu_P/4)^3} \tag{2.24}$$

This function is analyzed for the parameter, where the minimum lies on $\mu_P = 1$. This is the critical point, since for values greater than 1 the function ceases to provide rational values. This is because negative lift appears at the wing tips, and consequently also negative bending moments, which make no physical sense with the premise that the moment is proportional to the spar weight, which cannot be negative. So, from Prandtl's point of view, in this case the absolute value of the moment should be taken for the integral instead. Thus, the highest rational value of μ_P, before these incoherent results arise, is the optimum value. For values smaller than 1, the results start being inferior. Finally, when $\mu_P = 0$, which is equivalent to the elliptic distribution, the results obtained are notably worse, since the downwash is the greatest of all the results, with also the smallest values for Γ_0 and b. These results can be seen in Table 2.1. Moreover, Figure 2.8 shows the curves for circulation and downwash for μ_P values of $0, 1/3$ and 1.

Table 2.1: Span, circulation and induced downwash results for different values of μ_P (Prandtl, 1935).

μ_P	$b/4r_P$	Γ_0	w_i
0.00	1	1	1
0.25	1.0351	1.0305	0.9458
0.50	1.0801	1.0581	0.9096
0.75	1.1402	1.0795	0.8921
1.00	1.2247	1.0887	0.8889

From this, it can be concluded that this distribution provides a minimum induced drag, more optimal than the elliptical spanload distribution, which corresponds more to tapered wings. The induced drag becomes 11% lower than with elliptic distribution for a given total lift and a given moment of inertia of the total lift.

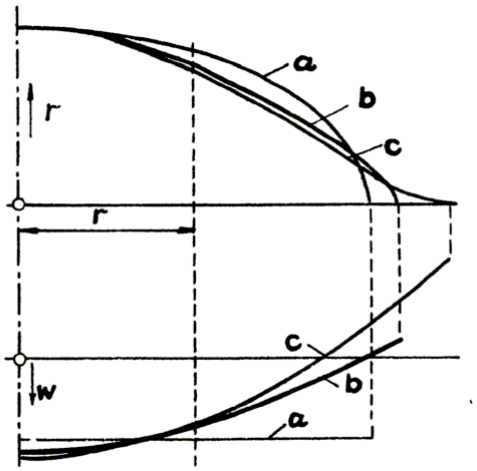

Figure 2.8: Curves for circulation and downwash. (a) Elliptical distribution: $\mu = 0$. (b) Intermediate case: $\mu = 1/3$. (c) Optimum distribution: $\mu = 1$ (Prandtl, 1935).

The methodology used in this work to develop a wing with non-elliptic lift distribution (later referred to as NELD) was that of Bragado Aldana and Lone (2019) and is described in detail in Chapter 5. However, it should be noted that this MATLAB based algorithm relies on lifting line theory (LLT) and therefore, is limited to simplified aerodynamic models.

2.3.3 Horten's Studies on Flying Wings

During the 1940s, Horten brothers studied a lot of new wing designs. They realised independently of Prandtl that the elliptic lift distribution could not be the more efficient one due to the span constraint. In the paper, Horten studies the distribution which gives the minimum induced drag for a given span and a constant structural weight using the lifting line theory. However, in the horseshoe theory, the downwash becomes infinite at the wingtips, which is not physically possible. To solve this Prandtl stated that if the circulation varies in a form of the ellipse, the downwash stays constant along the wing, tips excluded. So this solution results in a minimum induced drag but at the wingtips the circulation was considered null and the downwash unknown. Therefore, the concept of lift distribution with zero-tangent at the wingtip was studied. Horten named it bell-distribution and defined it as a function of sin^3.

In comparison with the elliptical distribution, the bell distribution has less lift at the outer wing (near the tips) and more lift at the root. In the design of flying wings, the zero-tangent distribution is important to avoid flow separation at the tips (Horten and Horten, 1984). Horten also observed that bell distributions provide proverse yaw, which means that a coordinated turn could be performed without the addition of a rudder, or at least with a minimization of its size. However, Horten found negative lift coefficients at the wingtips, and further investigations were needed to study the influence of this problem on the controllability of the aircraft.

Horten applied this distribution to real wings and found a decreasing circulation over the span and so a decreasing induced angle of attack. He observed that the induced angle of attack became negative at tip, but the lift remained positive. Thus the wing received thrust in that region, but it could not prove that this thrust was enough to provide proverse yaw. He also found analytically that the washout needed for the wing span decreased with the increase of the taper of the wing, so it helped to prevent flow separation. However, Horten found that for the same span, the bell distribution provided an induced drag 33% higher than with an elliptic distribution. To have the same induced drag, an increase in span of 16% must be added. Finally, the Horten's work shows that a more efficient lift distribution exists, be it with some caveats. For example, this distribution will be useful for wings with significant tapering and high aspect-ratios.

2.3.4 Bowers' progress on Prandtl Wings

Bowers et al. (2016) aimed to present a unifying theory of Prandtl (1933) alternative theory to minimize drag combined with Horten brothers (1984) solutions for flying wings. To understand this alternative theory, comparisons can be made between the elliptical and the so-called bell-shaped distributions on the forces exerted on a wing during flight. The elliptical spanload, as it has been described, provides the wing with a uniform downwash through all the trailing edge. At the wingtip, a sharp discontinuity is produced, where suddenly an upwash appears, causing a high strength vortex at that point. On the other hand, the bell spanload causes the wing to have a strong downwash at the root, which tapers outboard until it ends an in exion point near the wingtip where upwash appears.

In terms of aerodynamic forces, this means that the induced drag changes sign at that exion point, becoming induced thrust at the tips, since the resultant aerodynamic force tilts forward into the relative wind. Nevertheless, for the same span, the total net drag is greater than that given in an elliptical spanload. The theoretical direct benefit of such a result is proverse yaw. This means that a wing with such characteristics could be able to manoeuver in flight without the need of a vertical stabilizer, since adverse yaw would not occur, but a thrust into the desired yawing direction would appear. In the case of the bell-shaped distribution, the function pictures a smooth and continuous curve along the span, leading to a similar function for the downwash. With this distribution, the upwash at the wingtip blends with the upwash in the freestream in a gradual way than in the elliptical spanload, where an abrupt change from downwash to upwash is found. The solution to this theory posed by Bowers is approached in the following way. The lift distribution follows the curve:

$$L = \left(1 - y^2\right)^{3/2} \tag{2.25}$$

where L is the non-dimensional local load, which can be also expressed as Γ, and y is the span location between 0 and 1. Therefore, the non-dimensional downwash can be written as:

$$w = \frac{3}{2}\left(y^2 - 1/2\right) \tag{2.26}$$

With this, the lift and its slope as a function of the span approach to zero at the wingtip

$$\lim_{0 \to b/2} L\left(y\right) = 0 \tag{2.27}$$

$$\lim_{0 \to b/2} \frac{dL\left(y\right)}{dy} = 0 \tag{2.28}$$

Finally, the slope of the downwash, or upwash at the wingtips, is equal on both sides at this point:

$$\lim_{0 \to b/2} \frac{dw\left(y\right)}{dy} = \lim_{0 \to b/2} \frac{dw\left(y\right)}{dy} \tag{2.29}$$

To validate this simple approach, Bowers and his team compared the theoretical results obtained from this distribution to the experimental results collected from a radio-controlled wing designed to achieve this bell-shaped distribution of circulation, by means of adding twist at the wingtips, shown in Figure 2.9.

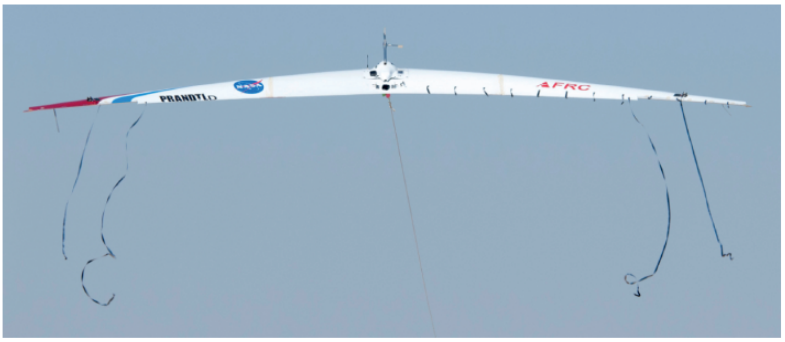

Figure 2.9: NASA's PRANDTL-D flying wing (Preliminary research aerodynamic design to lower drag) during experimental tests (Bowers et al., 2016).

The planform was based on Prandtl's theory and on the Horten H Xc aircraft. The objective of this experimental flights was to prove co-ordinated flight with the implementation of proverse yaw and no vertical surfaces. The results were compared in unitary terms to those of an elliptical spanload, giving the following values shown in Table 2.2:

Table 2.2: Elliptical and bell spanload comparison of parameters (Bowers et al., 2016).

Spanload parameter	Elliptical spanload	Bell spanload
$b/2$	1	1.2247
C_{d_i}	1	0.8889
e	1	0.8889

It is seen that a bell spanload provides better results in all this parameters, so for a flying wing of the same structural weight with a larger span than an elliptical spanload wing, a smaller induced drag coefficient is obtained. Also, the effect of induced thrust in side-slip resulting from a yawing moment is show for three different angles in Figure 2.10. It can be seen that a greater area of induced thrust on one side than on the other results in a large yawing moment, where the blue line is for -5°, the red line is 0° and the green line is $+5^{\circ}$.

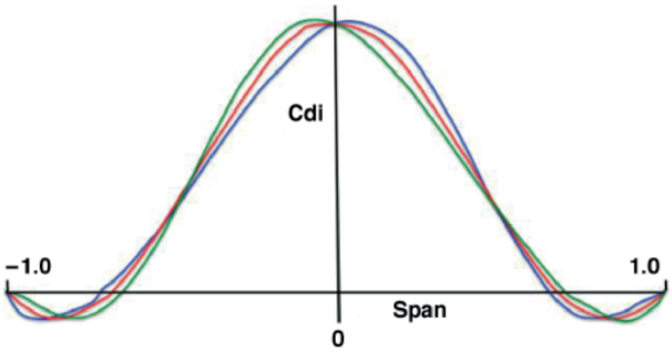

Figure 2.10: Effect of side-slip on bell spanload with twist (0° and ±5°) (Bowers et al., 2016).

Other positive results were obtained from the data trace of the angular rates. In Figure 2.11, it can be seen that the yaw rate follows the same motion and in the same sign as the roll rate, proving that proverse yaw is occurring.

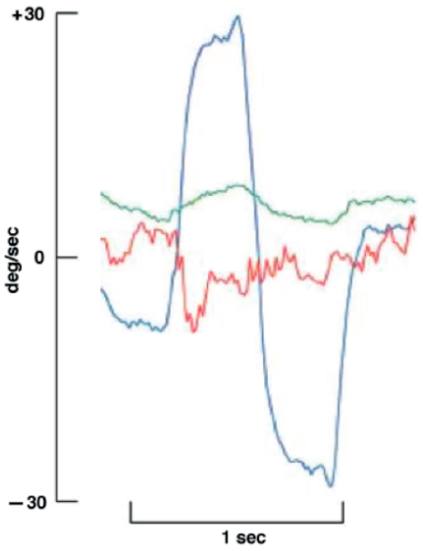

Figure 2.11: Data trace of proverse yaw: the green curve represents yaw rate, blue is roll rate and red is pitch rate (Bowers et al., 2016).

The yawing moment due to aileron deflection coefficient $Cn_{\delta a}$ was extracted from the experimental data. The results, shown in Figure 2.12, conclude in a positive value for the $Cn_{\delta a}$ with a trend of positive slope when plotted against the lift coefficient C_L, which also confirmed the expectations of the bell-shaped spanload. With all these results, it can be concluded that the bell spanload maximizes aerodynamic efficiency with a given structure and provides a coordinated roll-yaw motion, in the same way birds without a vertical stabilizer. This can be beneficial for improving aircraft designs and their efficiency, specially in flying wings or blended wing body aircraft. These benefits can be also applied in conventional aircraft, improving their aerodynamics from the approach of minimum structure. The results obtained also prove that proverse yaw can be achieved through a bell-shaped spanload, and that there is a better and optimal solution that integrates minimum drag and minimum structure that solves, at the same time, yaw control and stability problems in flying wings.

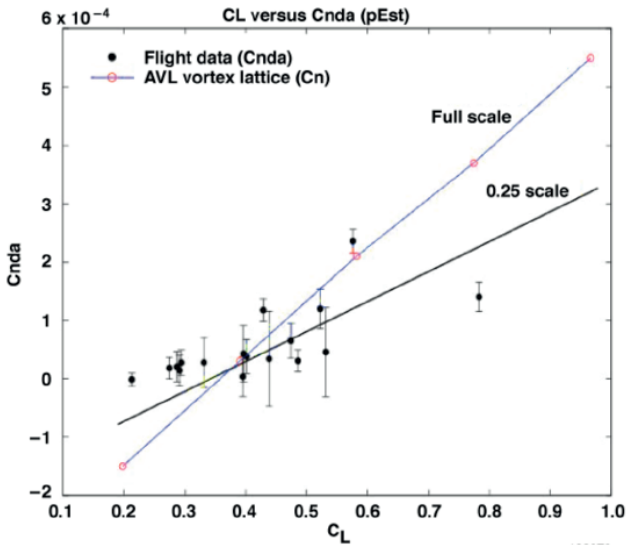

Figure 2.12: Yawing moment due to aileron deflection coefficient $Cn_{\delta a}$ against C_L (Bowers et al., 2016).

2.4 Boundary Layer Fundamentals

When a real fluid flows past a solid body or a wall, the fluid particles adhere to the boundary condition that no slip occurs. This means the velocity of the fluid at the boundary will be zero with respect to the surface. The velocity of the fluid increases from zero to $0.99U$ (free stream velocity) in the direction perpendicular to the flow. This region of varying velocity is called the boundary layer where the velocity gradient exists and hence, exerts a shear stress on the wall in the direction of flow (Bansal, 2005).

2.4.1 Effect of pressure gradients

When the static pressure increases in the direction of flow that is when $\frac{dp}{dx} > 0$ is called Adverse pressure gradient. This positive pressure gradient in the boundary layer increases the potential energy of the fluid therefore decrease in the kinetic energy of the fluid which results in retarding flow (Bansal, 2005). As shown in Figure 2.13 this slowing down of flow results in the flow getting separated from the surface. This separation of the flow causes eddies formation or recirculation of the flow which greatly effects the lift and drag characteristics of the airfoil. Turbulent boundary layers tend to be more stable than laminar boundary layers in adverse pressure gradients. Turbulent boundary layer has a zig-zag motion that is fluid layer gets mixed up which transport kinetic energy to the low momentum layer near the surface hence delaying the separation (McLean, 2012).

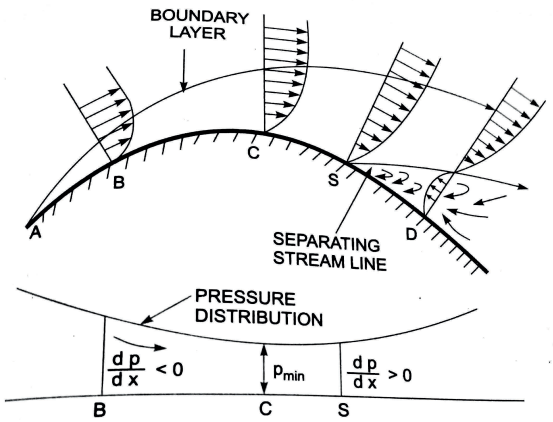

Figure 2.13: Effect of pressure gradient on boundary layer (Bansal, 2005).

2.4.2 Point of separation

The separation point S is determined from the condition:

$$\left(\frac{\partial u}{\partial y}\right)_{y=0} = 0 \tag{2.30}$$

Table 2.3 provides the nature of flow on the surface for different conditions of velocity gradient.

Table 2.3: Criteria For Boundary Layer.

Condition	Result	Boundary Layer
$\left(\frac{\partial u}{\partial y}\right)_{y=0}$	Positive	Flow attached to the surface
$\left(\frac{\partial u}{\partial y}\right)_{y=0}$	Zero	Flow on the verge of separation
$\left(\frac{\partial u}{\partial y}\right)_{y=0}$	Negative	Flow has separated

2.4.3 Laminar separation bubbles

One of the primary objectives of airfoil design is to minimize profile drag, which is composed of two components: friction drag and form drag. Immersed bodies exposed to a freestream with a Reynolds number less than 10^6 encounter laminar separation bubble (LSB) drag. Due to the unfavorable pressure gradient that produces the LSB, a turbulent transition occurs inside the separated shear layer, followed by a turbulent reattachment. After the reattachment point, LSB has a greater impact on the pressure distribution and behaves more predictably. When Re is more than 1.5×10^5, the LSB often dominates the entire drag. The LSB increases drag proportionally to the average mass deflected (Drela, 1989).

2.5 Design of wings

2.5.1 Design lift coefficient

The design lift coefficient is the first factor to consider when selecting an initial airfoil. The drag coefficient of a well-designed airfoil in subsonic flight is just slightly more than the skin friction drag when the airfoil is flying at its design C_L. To enhance the aerodynamic efficiency, the UAV should cruise at the design C_L. A first approximation can be made by assuming $C_L = C_l$ and in level flight the lift must be equal to weight therefore,

$$W = L = qSC_L \simeq qSc_l \tag{2.31}$$

$$c_l = \frac{1}{q}\left(\frac{W}{S}\right) \tag{2.32}$$

where q is dynamic pressure and is a function of velocity and altitude. W is weight and S is the wing area. (W/S) is also called wing loading. The wing loading decreases during flight as fuel is burned hence, the dynamic pressure should be reduced by climbing to a higher altitude. A wing maximum lift coefficient is (Raymer, 2012),

$$C_{L,max} = 0.9c_{l,max}cos\Lambda_{0.25c} \tag{2.33}$$

2.5.2 Stall

Stall characteristics are critical in airfoil selection. During a stall, certain airfoils lose lift gradually, whereas others lose lift abruptly, followed by a quick shift in C_m. This distinction indicates the presence of three distinct forms of airfoil stall as shown in Figure 2.14.

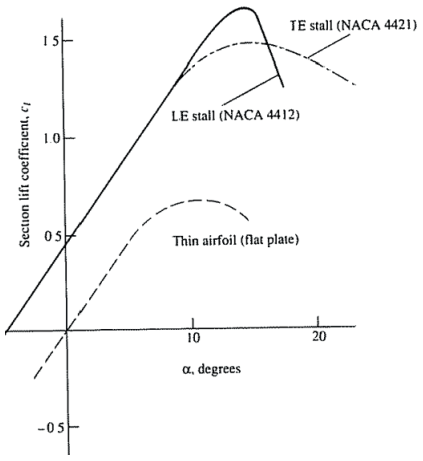

Figure 2.14: Effect of different stalls on lift gradients (Anderson Jr, 2010).

Leading edge stalls exhibit a sharp decline in lift near $C_{L,max}$ and a t/c of around $6-14\%$ (Raymer, 2012). At $C_{L,max}$, trailing edge stalls exhibit progressive bending-over of the C_L curve, a soft stall, and a t/c larger than 14%. The flat plate stall has the worst behaviour, exhibiting early stalling. The progression of the separation is seen in Figure 2.15. Washout, or reducing the α of the tip airfoils relative to the root, may cause the wing to stall first at the root. Even a wing with a bad stalling airfoil has a progressive stall. It will also shake the horizontal tail, warning the pilot that a stall is near. Similarly, the designer may choose to employ distinct airfoils at the root and tip, with the tip airfoil stalling at a greater α. This allows effective roll control at an α when the root is stalled.

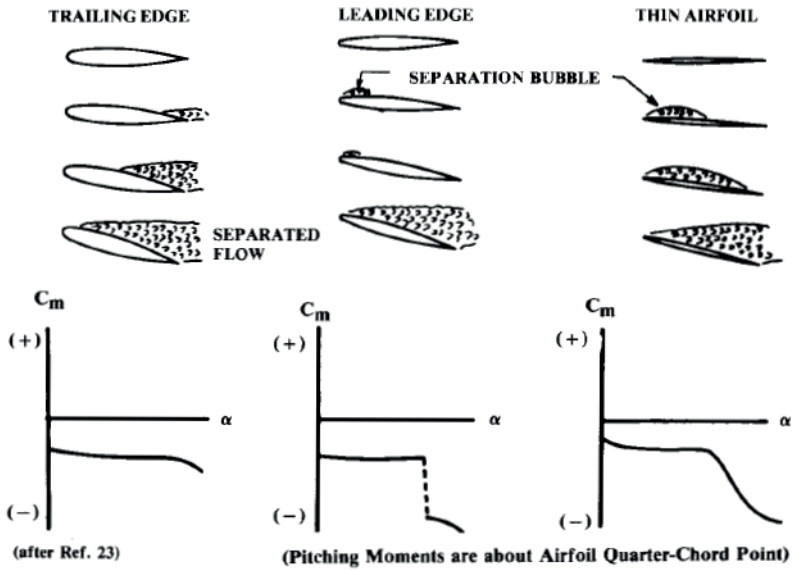

Figure 2.15: Types of stall (Raymer, 2012).

Airfoil choices must also take into account the plane's C_m. The C_m has to be close to zero for a stable tailless or flying-wing aircraft to function properly. An "S"-shaped camber with an upward reflex at the trailing edge is often required. When compared to an airfoil that was not subject to this limitation, reflexed airfoils have a worse L/D ratio. As a result of their smaller wetted surface area, flying wings lose part of their efficiency. Computerized flight control systems may eliminate the need for natural stability, allowing a non reflexed airfoil (Raymer, 2012).

2.5.3 Wing planform parameters

A high AR wing has tips further apart than an equivalent size low AR wing. So a high AR wing is less influenced by the tip vortex than a low AR wing, and the tip vortex intensity is lessened. A high AR wing loses less C_L and gains less C_D than a low AR wing of equivalent area.

Stability is enhanced by wing Λ but has little impact on aircraft dynamics at low subsonic airspeeds. A swept wing naturally exhibits a dihedral effect therefore a zero dihedral is used to prevent excessive stability (Raymer, 2012).

Taper ratio, λ is the ratio of the tip chord to the centerline root chord. The majority of swept wings have a taper ratio of about $0.2-0.3$ (Raymer, 2012). Taper has an effect on the lift distribution throughout the wing's span.

Wings are typically twisted between 0° and 5° in most cases (Raymer, 2012). The change in airfoil angle of incidence, generally measured with respect to the root airfoil, is known as geometric twist. Wash-out refers to a wing with a negative (nose-down) angle on the tip airfoil relative to the root airfoil. It is the distance from the root airfoil that alters a wing's twist angle.

The incidence angle of the wings is set to decrease C_D during a certain operating state, often cruise. The incidence angle is adjusted such that while the wing is at the right α for the specified design condition, the fuselage is at the lowest possible α.

2.6 Aircraft static stability

The term flight static stability is inclusive of the static longitudinal stability as well as the lateral directional stability of an aircraft. Static stability characterizes the ability of an aircraft to return to its original trim position after a disturbance such as a gust. This applies to both longitudinal and directional axis (McCormick, 1995).

2.6.1 Longitudinal static stability

In order to gain a better understanding of static stability, two points of forces need to be defined. The point for the force due to gravity is represented by CG. All aerodynamic forces at the aerodynamic center (AC). In most cases, the CG and AC are not in the same position on the longitudinal axis as shown in Figure 2.16. Equilibrium flight can only be achieved once the forces and moments cancel each other out:

$$T = D \tag{2.34}$$

$$L = W \tag{2.35}$$

Additionally, trim requires that the summation of pitching moments about the center of gravity must be zero, thus:

$$m = m_{ac} - l_w L = 0 \tag{2.36}$$

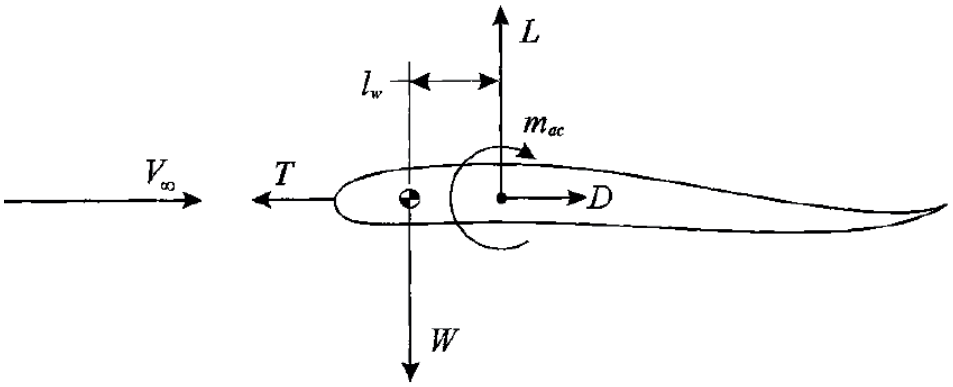

Figure 2.16: Longitudinal static equilibrium airfoil (Phillips, 2004).

where l_w is the distance that the aerodynamic center of the wing is aft of the center of gravity. Applying the lift and moment coefficient definitions, we can write:

$$C_m = C_{m,ac} - \frac{l_w}{\bar{c}} C_L = 0 \tag{2.37}$$

The moment coefficient about the aerodynamic center is fixed by the wing geometry, thus for a given weight and airspeed:

$$l_w = \frac{C_{m,ac}}{C_L} \bar{c} \tag{2.38}$$

Since the lift coefficient is positive and the moment coefficient about the aerodynamic center of a simple cambered wing is negative, we see that trim requires $l_w < 0$. Thus, in order to maintain static equilibrium, the aerodynamic center must be behind the center of gravity.

If the static equilibrium state is pitch stable, then a little increase in angle of attack must result in a negative pitching moment near the center of gravity in order to restore the angle of attack to trim condition. When a modest drop in angle of attack necessitates a positive pitching moment to restore the angle of attack to trim condition, the converse is true. Thus, the pitching moment around the center of gravity must vary with angle of attack in such a way that any change in angle of attack results in a change in the pitching moment about the center of gravity with the opposite sign.The mathematical criterion for pitch stability is then as follows:

$$\frac{\partial M}{\partial \alpha} = 0.5\rho V^2 S_w \bar{c} \frac{\partial C_m}{\partial \alpha} < 0 \tag{2.39}$$

Since the dynamic pressure, the wing area, and the mean chord length are always positive, pitch stability requires that:

$$\frac{\partial C_m}{\partial \alpha} \equiv C_{m,\alpha} < 0 \tag{2.40}$$

which is the general pitch stability criterion for any aircraft, and also known as the pitch stability derivative or pitch stiffness.

$$\frac{\partial C_{m_{ac}}}{\partial \alpha} - \frac{l_w}{\bar{c}} \frac{\partial C_L}{\partial \alpha} < 0 \tag{2.41}$$

$$\frac{\partial C_{m_{ac}}}{\partial \alpha} = 0 \tag{2.42}$$

and thus pitch stability requires that:

$$-\frac{l_w}{\bar{c}} \frac{\partial C_L}{\partial \alpha} < 0 \tag{2.43}$$

Since the change in C_L with α is positive for α less than stall, we see that stability requires $l_w > 0$. This means that for static stability, the aerodynamic center must be aft of the center of gravity. This condition is thus the opposite to that required for static equilibrium. Thus a simple cambered wing is not statically stable in free flight. Using the trim requirement to eliminate the distance l_w from the stability requirement gives the following:

$$-\frac{C_{m_{ac}}}{C_L} \frac{\partial C_L}{\partial \alpha} < 0 \tag{2.44}$$

This is the requirement for stable trim in tailless flying wing. The C_L must be positive to support the weight of the aircraft and the $C_{L\alpha}$ is positive for any wing at α below stall. Thus, a single wing without a tail must constantly create a positive pitching moment coefficient around its aerodynamic center in order to maintain stable trim. To generate a positive C_m around the aerodynamic center, an airfoil section must have negative camber across a significant portion of the chord. In general, flying wings have negative camber along a section of the chord at the trailing edge. An airfoil of this type is known to have a reflexed trailing edge. Flying wing designs are difficult at best and usually do not provide good handling qualities without a significant reduction in performance or the implementation of computer control.

2.6.2 Lateral static stability

Lateral motion deals with the remaining degrees of freedom such as side-slip(β) translation, rotation in roll and rotation in yaw. The Lateral forces and moments are side force Y (positive to the right), yawing moment, n (positive when it will cause the nose to yaw right) and rolling moment, l (positive when it will cause a roll to the right).

Yaw Stability is characterised by a restoring moment after a yaw disturbance, i.e. if the nose of the aircraft deflects to the left this causes a positive β, therefore requiring a positive restoring moment i.e. $\partial n/\partial \beta > 0$ and in nondimensional form $\partial C_n/\partial \beta > 0$. The value of yaw stability derivative($C_{n\beta}$) is estimated by considering the combined effects of the fuselage, propeller as

the vertical tail. The pusher propellers configurations tend to increase the directional stability. If the wings are swept back their contribution are stabilizing in yaw and conversely the wings swept forward have a destabilizing contribution to the yaw stability derivative. If $C_{n\beta}$ is positive the airplane is statically stable in yaw. This is due to the fact that a positive C_n (right-hand convention) is required to restore a positive disturbance in β. Phillips (2004) recommends a value between 0.06 and 0.15 per radian. An ultimate lower limit of 0.03 is suggested, with no actual upper limit.

Roll stability implies that an aircraft has a restoring moment whenever there is a disturbance in the bank angle. Stable aircraft in roll tend to want to fly with level wings when the aircraft is trimmed for no side-slip. The bank angle creates a force imbalance and causes side-slip $\beta > 0$ for a stable aircraft $l < 0$ the criteria states that $\partial l/\partial\beta < 0$ and in non dimensional form $\partial C_l/\partial\beta < 0$. If the roll stability derivative $C_{l\beta}$ is negative the airplane is statically stable in roll. This is due to the fact that a negative C_l (right-hand convention) is required to restore a positive disturbance in bank angle.

The Λ affects $C_{l\beta}$ indirectly because it affects the $C_{L\alpha}$ of the wing which is included in the estimation of the dihedral (anhedral) effect on $C_{l\beta}$; a right-hand rotating propeller has a stabilizing contribution to the $C_{l\beta}$; and a high wing is stabilizing and a low wing is destabilizing in roll. Phillips (2004) recommends a value between 0.0 and -0.1 per radian, but these are very rough guidelines for starting values and should only be used for that purpose.

2.7 Aerodynamic modelling

A crucial aspect of any flight dynamics modelling is the estimation of aerodynamic characteristics of the airframe. A vast amount of theories are available, ranging from simple lifting line to high order Navier-Stokes CFD solvers (Kier, 2005). Kier (2005) presented a comparison of aerodynamic modelling methodologies with respect to flight loads analysis on flexible aircraft structures. He claimed that classical methods derived from potential theory, such as the Vortex Lattice Method (VLM) are generally employed (Kier, 2005). This quasi-steady method results in an aerodynamic influence coefficient (AIC) matrix, thus calculation of the aerodynamic forces and moments reduces to a common matrix multiplication.

2.7.1 The Vortex Lattice Method (VLM)

The Vortex Lattice Method (VLM) is a method mainly used in the aircraft early design stages and for educational purposes. It models lifting surfaces as infinitely thin sheets of distinct vortices in order to compute the lift and the induced drag. The influence of thickness, viscosity and compressibility is generally neglected. This approach is best suited for aerodynamic configurations that primarily consist of thin lifting surfaces at small angles of attack and side-slip. Volumetric bodies are to be modelled with caution and are generally idealized with cruciform shapes. This method has been implemented using AVL software package.

2.7.1.1 Theory VLM relies on potential flow theory and the ideal flow assumption is made: viscosity, turbulence, dissipation, boundary layer and unsteady aerodynamics are not solved when carrying out the computations. The lifting surfaces and their trailing wakes are pictured as single-layer vortex sheets, discretised into horseshoe vortex filaments. When implementing VLM, one can assess lift, induced drag and pitching moment coefficients. In some restricted cases and with special considerations, stall phenomena can be modeled. Practically, the lifting surface is divided into several panels (Rom, 2012). On each of these panels, a box control point is defined. It is located at a 1/4 chord of the panel and the collocation point is placed at 3/4 chord. A collocation point is a point on a panel where the nornal velocity component is zero. A horseshoe vortex is applied at the box control point and the induced velocity vector is evaluated.

2.7.1.2 Limitations

As any CFD method, the VLM has limitations but these must be kept in mind when carrying out any analysis. The flow field is assumed to be inviscid, irrotational and incompressible. Yet, taking advantage of the Prandtl-Glauert transformation, subsonic compressible flow can be modeled. No unsteady aerodynamics phenomenon is modeled and the influence of thickness is neglected. Small angle approximation is made where both the angle of attack and the side-slip angle are assumed to be small.

2.7.2 XFLR5

XFLR5 is an aerodynamics and flight dynamics analysis tool developed by André Deperrois for low Reynolds Number airfoils, wings, and aircraft. It offers capabilities for designing and analyzing wings using the Lifting Line Theory, the Vortex Lattice Method, and a three-dimensional panel method. It implements three different 3-D numerical methods:

1. Non Linear Lifting Line Theory : This method should be used for medium to high aspect ratio wings as it assumes 2-D wing surface. It is best suited for wing with no dihedral and no sweep.

2. Vortex Lattice Method : The VLM as presented before is suitable for low aspect ratio lifting surfaces and can deal with dihedral and wing sweep. It takes advantage of the foil design capability of XFLR5 to predict and model viscous drag.

3. 3-D Panels Method : The 3-D panel method is an extension of the two previous methods as it takes into account the thickness of the lifting surface and provides a 3-D pressure distribution around the wing.

XFLR5 also provides stability analysis capabilities. It can estimate aerodynamic and control derivatives of an aircraft for a given trimmed flight condition based on its mass properties. However, this analysis does not take viscous effects into account. Furthermore, fuselage (bluff bodies) modelling is not recommended within XFLR5 just as with AVL.

2.8 Computational Fluid Dynamics

Computational Fluid Dynamics (CFD) is a high-fidelity modelling method for studying fluid properties in aerodynamic, hydrodynamic, and heat transfer applications, among others. Because the governing equations of fluid dynamics with defined boundary conditions (the Navier-Stokes equations: a coupled system of non-linear partial differential equations) are very difficult to solve analytically, CFD works by numerically solving them. The SST $k-\omega$ turbulence model, $\gamma - Re_\theta$ transition model, wall functions and grid convergence index are presented in this section. The CFD analysis was conducted using the Star-CCM+ V13.04 software package.

2.8.1 Menter's k-ω shear stress transport (SST)

Menter (1994) suggested a hybrid model that uses the $k-\omega$ model in the near wall region but utilises the insensitivity of the $k-\varepsilon$ model in the fully turbulent region away from the wall. The switch between the two models is achieved with a blending function of the model coefficients. The modification of the $k-\omega$ model is meant to improve the prediction of flows with strong adverse pressure gradients and separation (Cebeci, 2004). By design, this model is meant to improve on both the $k-\varepsilon$ and $k-\omega$ turbulence models at the wall and in the freestream. For these reasons, it was chosen as the model to be used throughout this report. The SST $k-\omega$ model also provides a platform where additional turbulence models can be added.

2.8.2 Transition modelling

The $\gamma - Re_\theta$ is a correlation-based transition model and is widely used in the aerospace industry for simulating low Re cases. The transition is from laminar to turbulent boundary layer. The transition model is a coupled extension to the SST and will be responsible for predicting the complicated flow in the boundary layer. The model consists of two transportation equations. One intermittency, γ equation responsible for predicting the percentage of flow that is turbulent and trigger the transition process. The equation relies on the onset momentum thickness Re_θ inside the boundary layer in its predictions (Menter, 1994).

This is a nonlocal operation i.e. these values must be experimentally identified and implemented. The equation then forces the transport variable to follow the value of Re_θ and diffuses this value into the boundary layer using a blending function $F_{\theta t}$. In this way the strong variations of the pressure gradient and turbulence intensity in the freestream will be taken into account, resulting in a transition model suited for predicting flow separation, reattachment and laminar separation bubbles (Langtry, 2006).

2.8.3 Wall y+ condition in the viscous sub-layer

The y^+ wall treatment was used to guarantee that the mesh grid was fine enough to mimic the flow gradients near the wall. The non-dimensional wall distance, y^+, is defined as follows.

$$y^+ = \frac{u^* y}{\mu_l}$$

where

$$u^* = \sqrt{\tau_w / \rho}$$

Where y is the height of the nearest cell to the wall μ_l is the local dynamic viscosity of the fluid. u^* is the friction velocity, τ_w is the wall shear stress and ρ is the density. When using a turbulence model such as the SST $k - \omega$ to predict turbulence is it important that the first cell in the near wall regions is small enough to capture the viscous sublayer. To ensure that the boundary layer is resolved correctly, a wall $y^+ < 1$ criteria was used through out the simulations.

2.8.4 Grid convergence index

Grid convergence index (GCI), a method developed by Roache (1997) compares exact result to the discretized result by using error bars. GCI method requires a minimum of three refinements, where it attempts to minimise discritization error (Roache, 1997). It specifies the connection between consecutive meshes of varying size, where the mesh count is doubled with each refinement. As a result of grid refinement, it is possible to get a Richardson Extrapolation which has a valid asymptotic range for the solution. Three CFD solutions would be developed: G1, G2, and G3, with G1 being coupled to the finest mesh possible. The convergence order, p, may therefore be computed as follows:

$$p = \frac{ln\left(\frac{G_3 - G_2}{G_2 - G_1}\right)}{ln(q)} \tag{2.45}$$

Exact performance parameters (at zero grid spacing) may be estimated using Richardson Extrapolation, which ignores higher-order terms. According to the fine grid, the Grid Convergence Index (GCI) is defined as:

$$GCI_{fine} = F_S \frac{\mid \varepsilon \mid}{q^p - 1} \tag{2.46}$$

Where F_S denotes factor of safety which is 1.25 when three solutions are available. The relative error, ε, is defined as:

$$\varepsilon_{12} = \frac{G_2 - G_1}{G_1} \tag{2.47}$$

After calculating GCI_{12} which is convergence index between fine and intermediate mesh, and GCI_{23} is between intermediate and coarse mesh. Once calculated and if,

$$GCI_{23} = q^p GCI_{12} \tag{2.48}$$

or

$$\frac{GCI_{23}}{q^p GCI_{12}} \approx 1 \tag{2.49}$$

then the solution is in the asymptotic range of convergence and hence, it is assumed that the solution is mesh independent and is enough to capture flow features required for the study.

2.9 Chapter conclusion

In this chapter some aspects of aircraft design, flight mechanics and computational fluid dynamics were reviewed which laid the essential theoretical basis for this work. NELD theory could reduce the induced drag whilst also addressing specific stalling characteristics at the tip, but that is an issue of optimisation/design, and not something that has been uncovered in the literature review of this chapter. A key wing design parameter is aspect ratio and a small wing sweep angle is sufficient to achieve the target aerodynamic performance. Choosing a transitional model is important for accurate estimation of aerodynamic performance especially drag. Now, a benchmark study is required to understand the physics-based models used within the computational software and to validate the workflow that will be used to investigate the AREND UAV (details of this baseline configuration are provided later in Chapter 4). could be reduced

3 Benchmark study of NACA0012

3.1 Introduction

The AREND UAV operates in the transitional regime at a Reynolds number of $Re_c = 5 \times 10^5$. Flow in the transitional regime changes from laminar to turbulent and this gives rise to complexity as the two phases are interacting simultaneously. Prior to undertaking numerical analysis on the full UAV, a benchmark study on a basic airfoil and wing configuration in a similar flow regime is necessary to understand the flow physics. Tank et al. (2017) conducted a computational and experimental investigation of the NACA0012 airfoil and wing at $Re_c = 10^5$. This chapter attempts to compare the numerical analysis to the study conducted by Tank et al. (2017) in order to show reliability of the turbulence models used for further studies.

3.2 Geometry

The benchmark study consists of a 2D NACA0012 airfoil and a 3D wing case. Instead of a sharp trailing edge both models were truncated at $0.99c$ hence giving them a blunt trailing edge which facilitates meshing and convergence.

The 2D model was a NACA0012 airfoil of length c. The domain was represented as a circular plane with a diameter of $16c$. The airfoil LE was located at $8c$ from the inlet and TE was $7c$ from the outlet, as shown in Figure 3.1a.

The 3D geometry is a NACA0012 straight wing with a aspect ratio of $AR = 3.7$ and a chord length, $c = 0.075m$ at a Reynolds number, $Re_c = 10^5$. The domain was represented as a cylinder with a upstream length of $24c$ from LE, total length of $75c$ and a diameter of $18c$, as shown in Figure 3.1b to match numerical domain of Smith (2017).

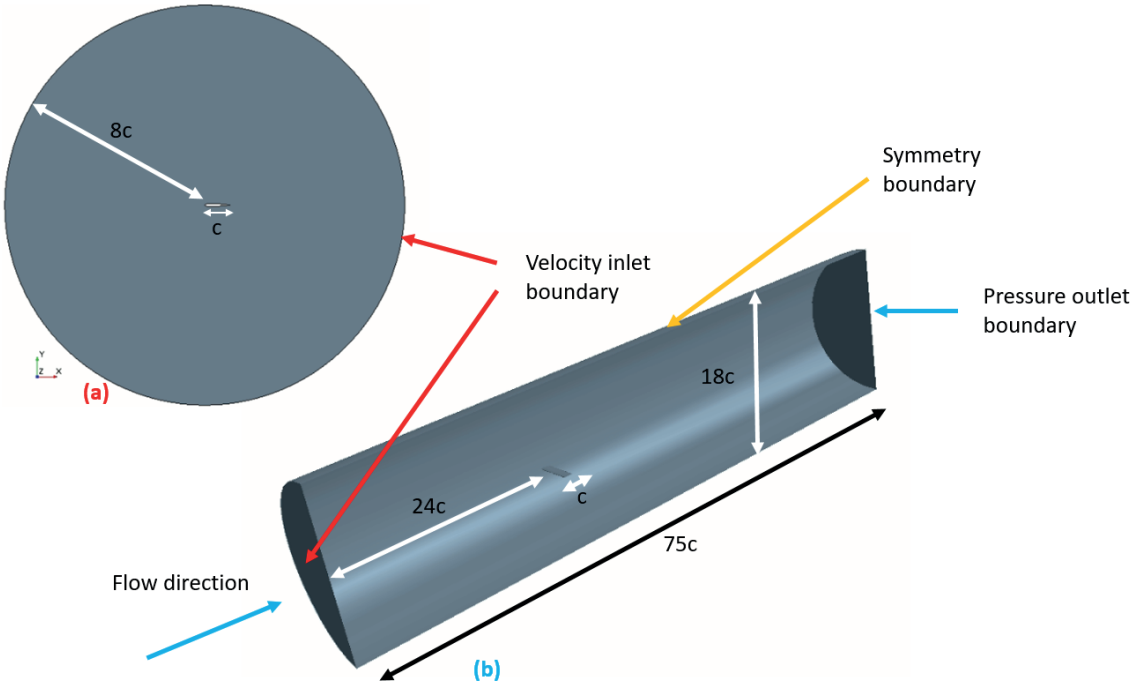

Figure 3.1: Domain for (a) 2D NACA0012 airfoil and (b) 3D NACA0012 wing at $Re_c = 10^5$.

3.3 Defining boundary conditions

The 2D domain was modeled as a velocity inlet boundary condition. The 3D domain consisted of an inlet which was a constant velocity boundary condition, outlet was a atmospheric pressure boundary condition and the outer surface had a symmetric boundary condition. The boundaries

at the surface of the airfoil and wing were specified as viscous wall (no-slip) boundary conditions. The boundaries at the symmetry plane were specified as an inviscid wall boundary condition. The flow is modeled for steady and incompressible conditions.

3.4 Meshing

Mesh independence study is used to ensure that the solution does not depend on the density of the mesh. Volumetric refinements are used around the airfoil and wing bodies to increase the density of the cells to resolve the viscous layers as shown in Figure 3.2. A near body region refines the cells near the body (boundary layer) which gradually increases as the cell is moved away from the body. The refinement regions for the wake and flow over wing tips was refined to capture trailing edge vortices. Additional refinement zones are added to the leading edge and surrounding area as the flow changes are sudden near leading and trailing edges, necessitating the addition of more cells. A cone shape refinement zone is added at the wing tips to capture tip vortices as shown in Figure 3.2(b). The diameter of the cone shaped refinement zone increases as it goes downstream from the leading edge.

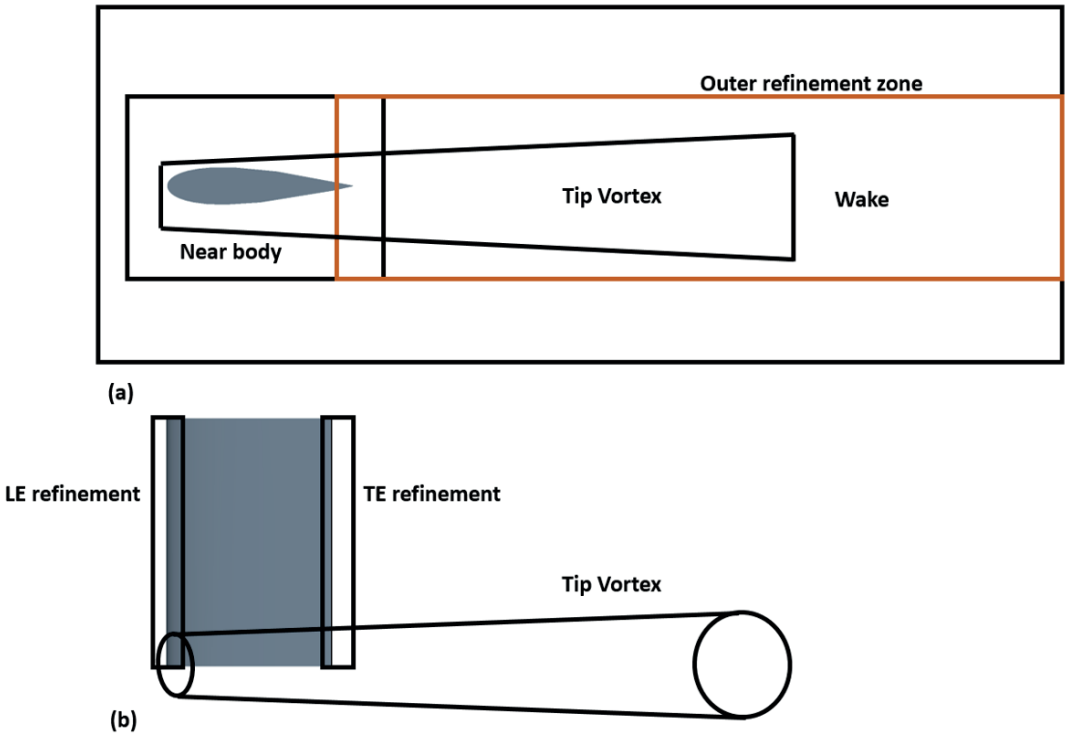

Figure 3.2: Mesh refinement regions (a) wake (b) leading edge, trailing edge refinements with tip vortex refinement region.

The mesh for the NACA0012 airfoil and wing are shown in Figure 3.3 and Figure 3.4 respectively. Both geometries consist of polyhedral cells and prism layer cells to resolve boundary layer. Advancing layer mesher is used to generate prism layers because it prevents prism layer cells from collapsing around sharp corners. Both geometries consisted of 30 prism layer cells across the height of the boundary layer with near field cell size of $0.01mm$ and increasing in geometric progression. Surface growth rate was set to 1.01 which is 10% of the previous mesh size. Wake refinement feature for airfoil is used where a spread angle of 0.3 radians was defined. It generates a triangular wake refinement as seen in Figure 3.3. At low Reynolds numbers especially in the transition flow regime, the flow physics is sensitive to the boundary layer mesh. To ensure that the boundary layer is resolved correctly, a wall $y^+ < 1$ criteria was used throughout the simulations.

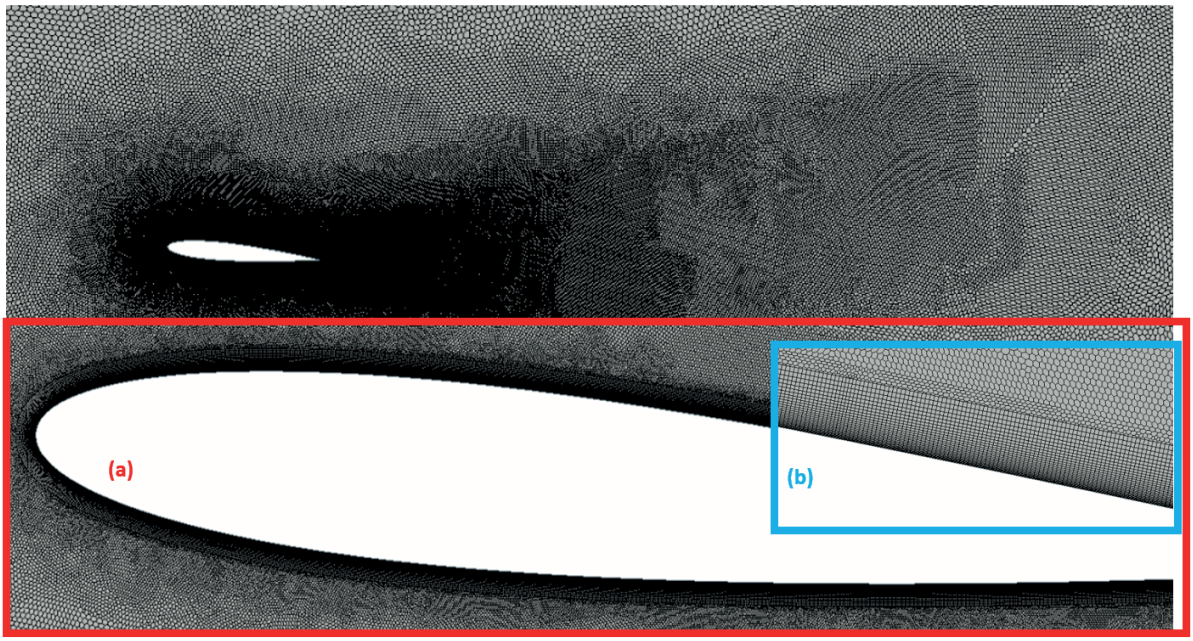

Figure 3.3: NACA0012 mesh far field with triangular wake region (a) enlarged version (b) prism cell at the boundary layer.

Refinements for the 3D wing are shown in Figure 3.4. A wake refinement region extending from the trailing edge to $45c$ downstream. A near body refinement zone is added to capture the flow over the leading edge and surrounding area as the flow changes are sudden near leading and trailing edges, which requires more cells. This region spans $2.5c$ top and bottom, $0.5c$ from the leading and trailing edge respectively. A transition refinement zone extends $1c$ top and bottom, allowing for a smooth transition from nearby body cells. The cone's diameter grows from $0.2c$ at the leading edge to $2c$ at $30c$ downstream to capture tip vortex. Figure 3.4b illustrates refinement along the leading and trailing edges.

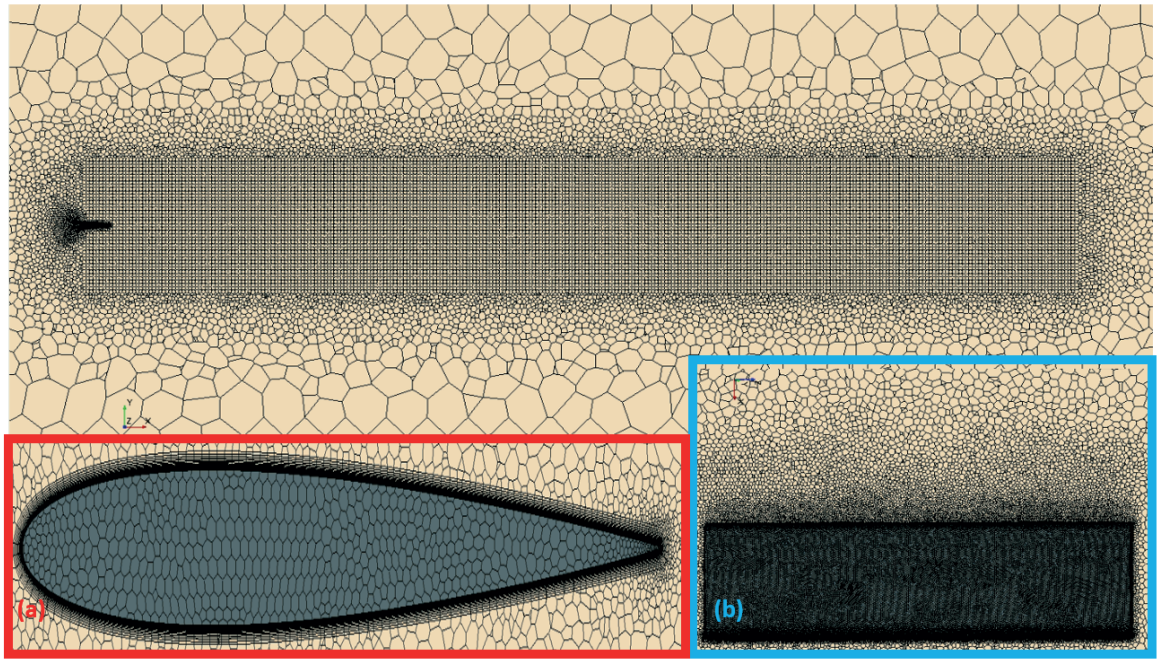

Figure 3.4: NACA0012 wing with wake refinement region (a) prism layer around the wing (b) surface mesh transition towards trailing edge.

3.5 Turbulence modelling

Turbulence modelling in transitional flow regime is difficult due to presence of laminar separation bubble. Steady state SST $k-w$ turbulence models have been used in similar studies due to its reliable prediction of flow separation (Menter, 1994). Figure 3.5 compare the flow over the airfoil with and without transition model. The SST $k-\omega$ turbulence model coupled with $\gamma - Re_\theta$ transitional model is used to predict laminar-turbulent transition bubbles (LSB's) which is expected around this Reynolds number (Menter et al., 2006). A field function, free stream edge is needed which differentiates between boundary layer (highly viscous) and potential flow. It is seen that the turbulence model when coupled with transition model artificially simulates small eddies or separation bubbles as seen in Figure 3.5(b) respectively.

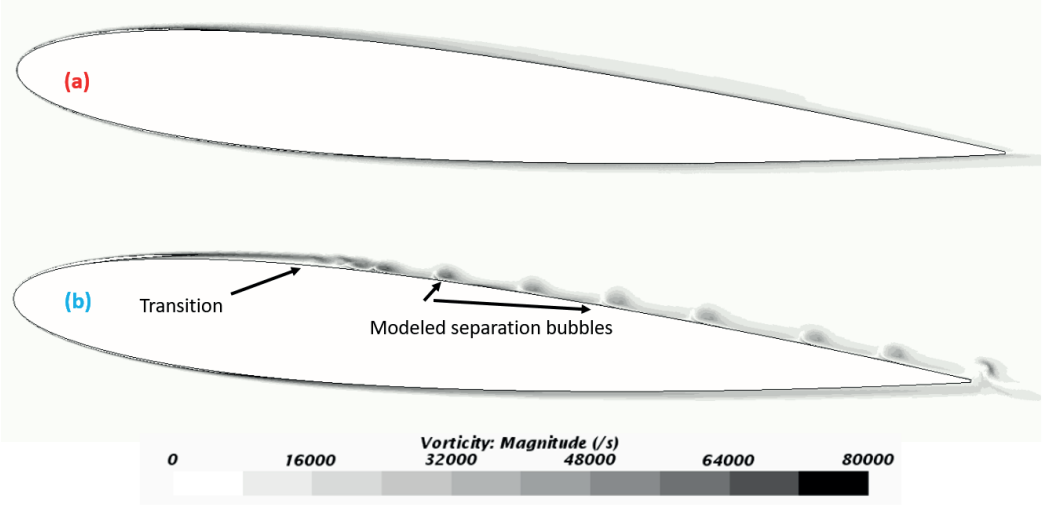

Figure 3.5: Vorticity contours plot at $\alpha = 5°$(a) no transition model (b) applied transition model.

A clear distinction is seen between the flow physics with and without turbulence modelling. The LSB's are only seen when a $\gamma - Re_\theta$ transitional model is used with the RANS SST $k-\omega$ model. But it should be noted that the flow is unsteady and therefore, RANS only provides approximation within variation limits ($\pm 10\%$).

3.6 Mesh independence study

This study follows a method by which the solution is independent of mesh count or mesh density. The error due to discretization of the domain should be minimised and it is done by refining the mesh. As the mesh is refined, there is an exponential increase of the mesh density and it is assumed that as the mesh resolution goes to zero, the solution tend towards the actual flow patterns and results. However, in reality it is not possible computationally, as a result, several ways have been devised that indicates whether or not the mesh is adequate (ASME, 2009). In order to know if the mesh is satisfactory to capture the flow patterns a mesh independence study is performed.

Grid convergence index (GCI), a method developed by Roache (1997) compares exact result to the discretized result by using error bars. GCI method requires a minimum of three refinements, where it attempts to minimise discritization error. It specifies the connection between consecutive meshes of varying size, where the mesh count is doubled with each refinement. As a result of grid refinement, it is possible to get a Richardson Extrapolation which has a valid asymptotic range for the solution.

Figure 3.6, shows the mesh independence achieved using Grid convergence index (GCI) for NACA0012 airfoil and wing. The CFD solutions used in this case were average C_D as the flow

was unsteady the flow has some degree of variance ±10%. The C_D values with standard deviation falls under the limit.

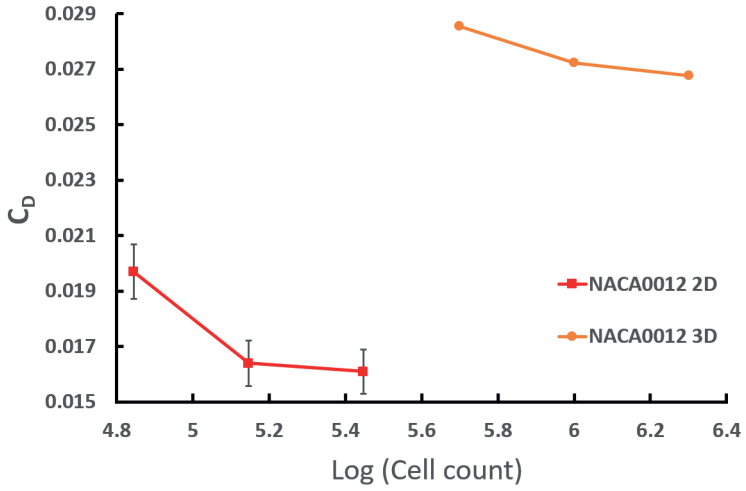

Figure 3.6: C_D against log of cell count for NACA0012 airfoil and wing.

3.7 Comparison of results

3.7.1 Two dimensional results

The NACA0012 airfoil was simulated for a range of angles of attack from $-5° \leq \alpha \leq 8°$. Figure 3.7 shows the lift coefficient with respect to angle of attack. The 2D C_l values are compared to the theoretical $2\pi\alpha$, simulations and experimental work from Tank et al. (2017). For $-5° \leq \alpha \leq -3°$, the experimental and simulation results are similar, from $-2° \leq \alpha \leq 2°$, follow the 2π slope. After $\alpha = 4°$, the $C_{l\alpha}$ is less than 2π and from $4° \leq \alpha \leq 8°$, the simulated results sit in between the numerical and experimental studies as the viscous effects start to dominate. The maximum difference between the simulation and Tank et al. (2017) is 4.7% at $\alpha = 5°$ which can be due to the RANS performance being mostly governed by the boundary layer and model coefficients, and not by the outer potential flow Tank et al. (2017).

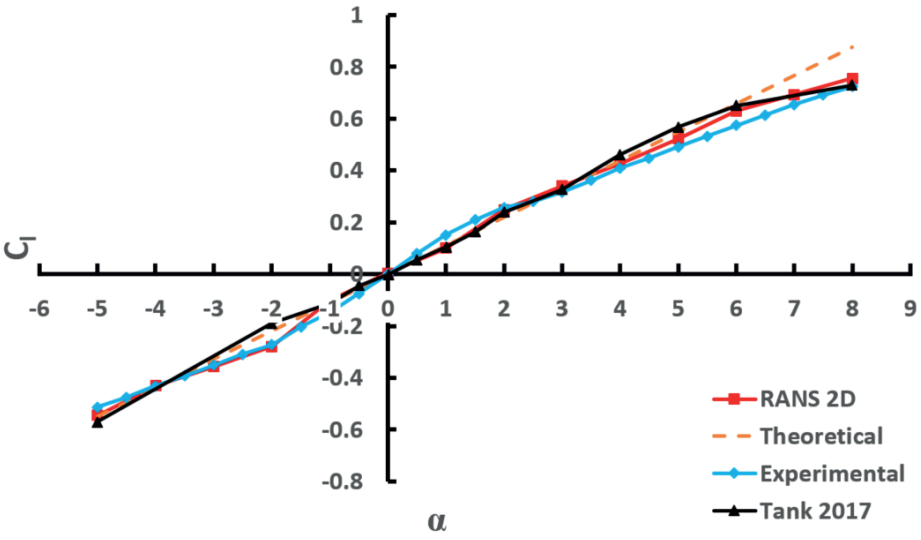

Figure 3.7: C_l against α for NACA0012 airfoil compared with Tank et al. (2017).

The C_d in Figure 3.8 have a closer agreement with the numerical work from Tank et al. (2017)compared to the experimental work. 2D mesh cannot capture laminar separation bubbles

due to their 3D nature which explains the low drag prediction by the CFD studies (Almutairi et al., 2010). The results were calculated by taking an average value of the fluctuating force coefficient keeping in mind the variance or standard deviation.

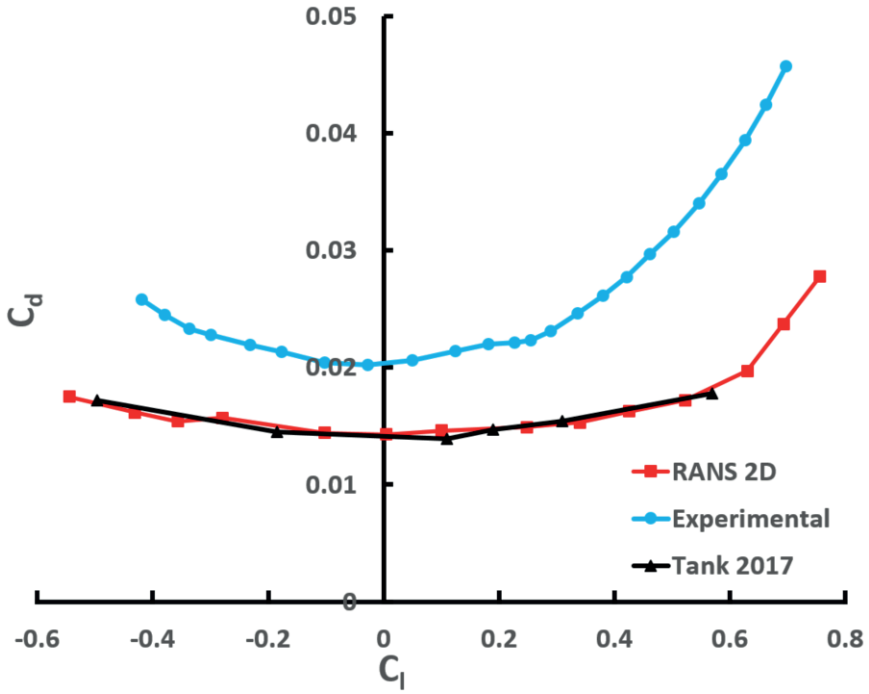

Figure 3.8: Drag polar for NACA0012 airfoil compared with Tank et al. (2017).

3.7.2 3D wing results

The results were compared to the theoretical value $C_L = 2\pi\alpha(AR/(AR+2))$ as shown in Figure 3.9. From $-5° \leq \alpha \leq -3°$, the results are similar whereas between $-3° \leq \alpha \leq 0°$, the CFD results are in between Tank et al. (2017) numerical and experimental results. It is due to the variation in C_L values due to vortex shedding and can also be due to the correct $\gamma - Re_\theta$ boundary prediction (free stream function)(Almutairi et al., 2010). From $0° \leq \alpha \leq 3°$, the results match the experimental results which can predict the flow features in the wind tunnel. This may be due to the spanwise component of LSB's being accurately resolved. Also it can be seen that the C_L is more than the theoretical value due to the unsteady behaviour of the simulation and the variance in the results. From $4° \leq \alpha \leq 8°$, the results are within 5% of the (Tank et al., 2017) numerical study. The solution at small angles depends on trailing edge separation whereas results at higher α are dominated by LSBs. At low Reynolds number, the flow is dominated by viscous layers and their effective resolution using transition models coupled with turbulence model is important because the solution depends on effective resolution of the boundary layer. Furthermore, changes in the residuals were noted, which is often an indicator of an unstable flow. It is seen that LSB's start moving forward covering a large percentage of chord length results in lower $C_{L\alpha}$ (Smith, 2017; Tank et al., 2017). It happens as the pressure fluctuations due to LSBs cannot create enough C_L due to continuous separation and reattachment zones.

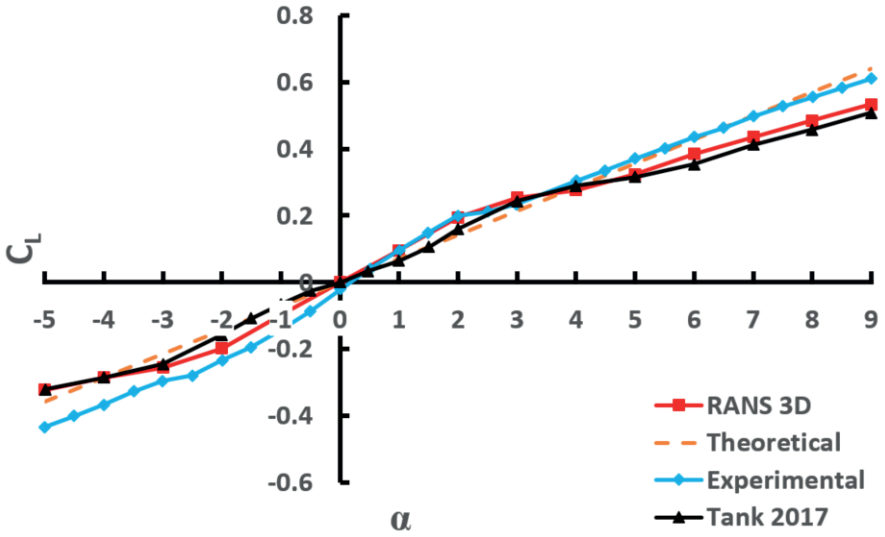

Figure 3.9: $C_L$against α for NACA0012 wing compared with Tank et al. (2017).

The polar curves for the wing at various angles of attack is plotted in Figure 3.10. The C_D differs on average by about 2% between the CFD and Tank et al. (2017) study.

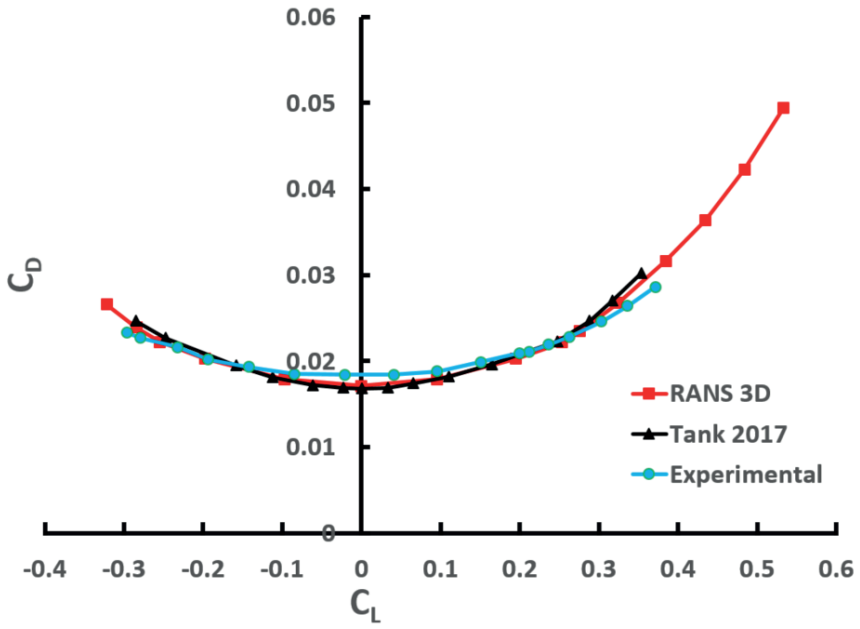

Figure 3.10: Drag polar for NACA0012 wing compared with Tank et al. (2017).

3.8 Chapter conclusion

This chapter is used as a benchmark study at the similar Reynolds number as the AREND UAV. The fluctuations due to vortex shedding suggests that the flow is unsteady and it is difficult to predict the force coefficient with steady RANS simulations. Unsteady analysis should be done to see the upper and lower bounds of the force coefficients. The workflow in this chapter is used to set up a CFD model that will be used for all the remaining analysis in this work. Although the results were within only 5% of Tank et al. (2017) the level of accuracy was deemed acceptable to model the AREND UAV and the NELD configuration which will essentially have similar limitations. Therefore the results can not be seen as ultimately representative, but rather as an approximate prediction towards trends.

4 CFD of AREND UAV

4.1 Introduction

In this chapter, different aspects of the aerodynamic properties of the AREND UAV have been investigated using CFD for a range of angles of attack and side slips. The maximum take off-weight for the UAV is $18kg$ and the cruise speed is $20m/s$. The maximum Reynolds number of the flow over the root of the wing (of chord $0.381m$) was found to be 5×10^5. Since the flow under consideration is low subsonic as well as being a low Reynolds number flow (transitional regime), based on the previous discussions in Chapter 3, RANS modelling approach with $SSTk - \omega$ coupled with $\gamma - Re_\theta$ transition model is employed. The study was done at reference density of $1.18415kg/m^3$ and reference pressure was $101325Pa$, for $0° \leq \alpha \leq 16°$ in $2°$ intervals and $0° \leq \beta \leq 15°$ in $5°$ intervals. The airflow was modeled as steady and incompressible and the wall $y^+ < 1$ criterion was satisfied for all simulations. The objective of this study is to compare the data against AVL code, analyse the aerodynamic and flight dynamic data which serves as the benchmark for the new NELD wing design.

4.2 Geometry

AREND represents a low subsonic UAV with inverted V-tail and pusher propeller configuration. The aspect ratio, $AR = 15$ is a high aspect ratio with wing area, $S_W = 1.21m^2$. At 60% of the wing span, the wing is separated into two halves with inboard wing which has a taper ratio, λ_1 of 0.35 with a twist angle of 0.6° and the outboard wing starts at 60% of the half span with λ_2 of 0.75, a twist of $-1°$ and a dihedral angle of 4°. The wing's airfoil is E214, which has a maximum thickness to chord ratio of 11.1 at 33.1% of the chord. The tailplane (inverted V-tail) has a symmetric HT14 airfoil with a maximum chord to thickness ratio of 7.5% and an inclination angle of 41.5°. Additionally, the UAV's primary dimensions have been projected onto a horizontal plane and measured using Solidworks and are summarized in Table 4.1.

Table 4.1: Defining the geometry of AREND.

Element	Length	Units
UAV length	1743	mm
Wing-Span	4254	mm
Wing Root chord	381	mm
Wing Tip chord	133	mm
Tail root chord	296.7	mm
Mean aerodynamic chord (MAC)	301	mm

Figure 4.1 shows the AREND configuration with fuselage, wing, booms and empennage. The F2-49 fuselage is a low drag body that has been modified to accommodate electronics and to connect the propeller at the rear of the fuselage. The sharp trailing edge for wings and empennage were truncated at $0.99c$ hence giving them a blunt trailing edge which facilitates meshing and convergence. Finally, several assumptions have been made concerning the UAV model. The propeller and control surface were removed.

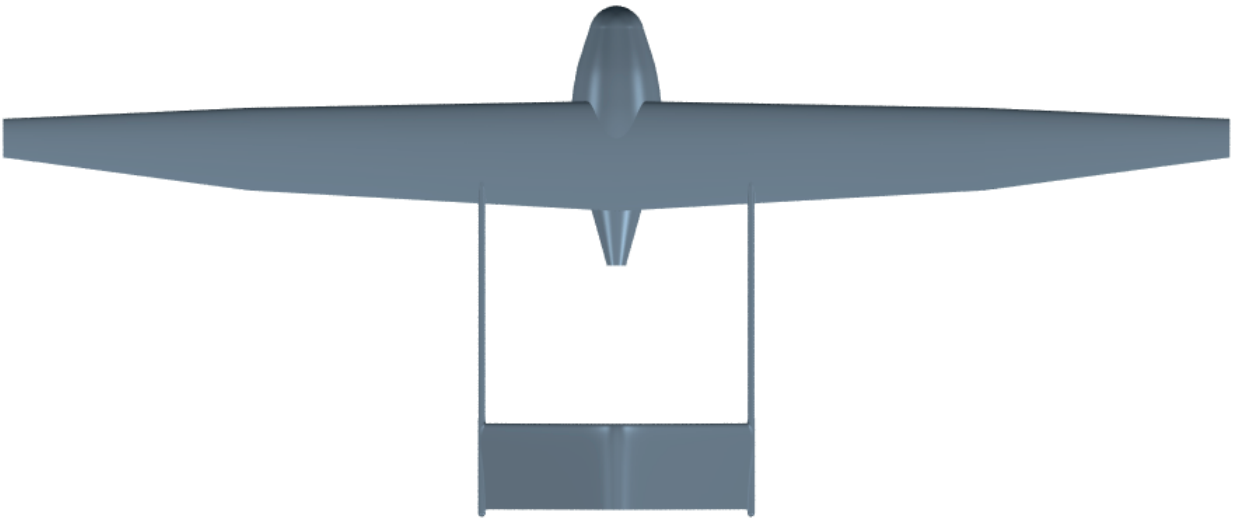

Figure 4.1: AREND configuration after cleaning the geometry.

4.3 Domain sizing and boundary conditions

Domain sizing study aims to provide an optimal domain volume required to capture the flow features without the cost of heavy computational time. The important parameters in the domain were the length upstream and downstream from the wing and the farfield extent of the domain. Domain width was identified as a critically important boundary due to the formation of the wingtip vortices. C_L and C_D were computed for a range of farfield, inlet and outlet lengths as seen in Figure 4.2. The percentage change in lift coefficient at $16c$ and $20c$ domain inlet in Figure 4.2a was 4% and the percentage change in drag coefficient was 1.5%. In Figure 4.2b the percentage change in lift coefficient at $82c$ and $100c$ domain outlet was 0.76% and the percentage change in drag coefficient was 1.73%. For the farfield boundary condition in Figure 4.2c, the percentage change in lift coefficient at $16c$and $20c$ was 0.1% and the percentage change in drag coefficient was 1.2%.

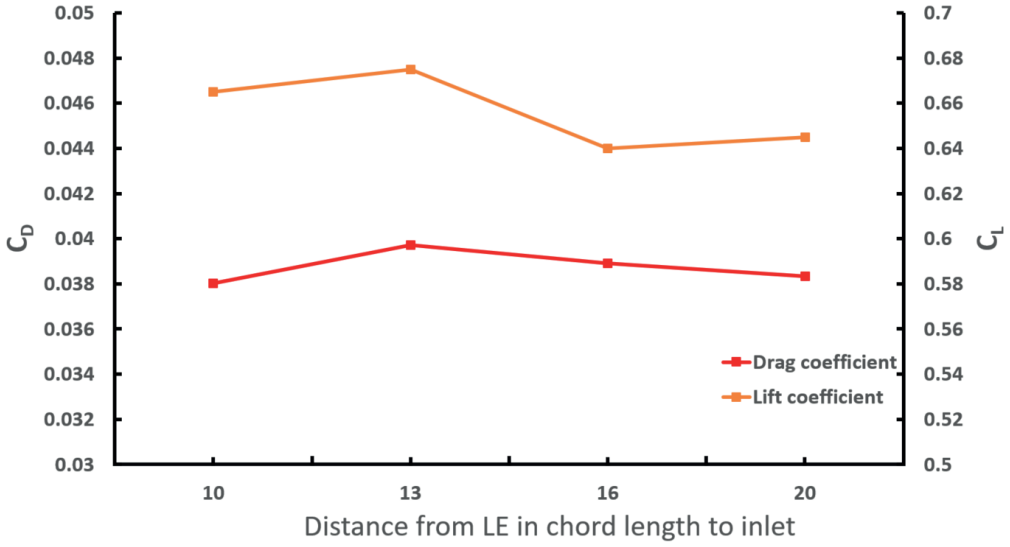

(a)

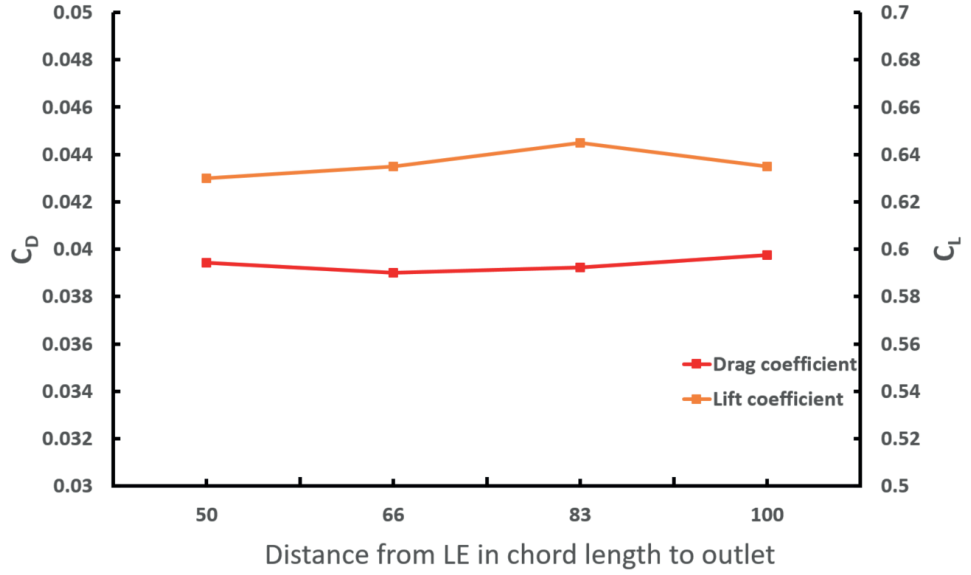

(b)

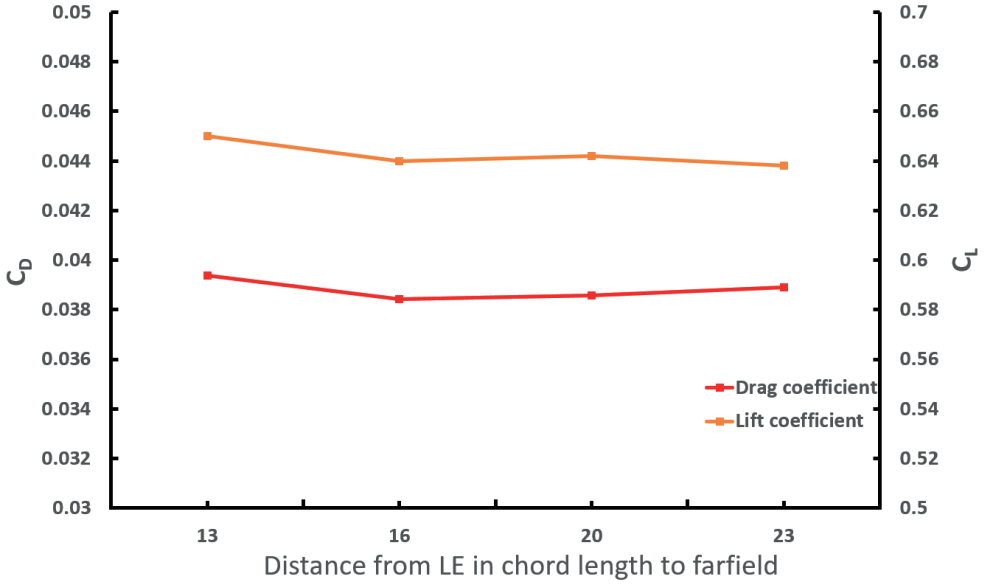

(c)

Figure 4.2: Change in lift and drag coefficients against (a) domain inlet, (b) outlet and (c) width.

A cylindrical domain based on the domain sizing study is used and all the dimensions are measured from the origin of the UAV. The inlet was fixed at around $16c$, the outlet at $65c$ from the end of UAV trailing edge and the farfield was set to $16c$ diameter. The control volume for AREND UAV is shown in Figure 4.3. The domain was defined by a constant velocity inlet boundary condition, outlet was set to atmospheric pressure boundary condition and the outer surface had a symmetric boundary condition. The boundaries at the surface of the UAV were specified as viscous wall (no-slip) boundary conditions. The boundaries at the symmetry plane were specified as an inviscid wall boundary condition.

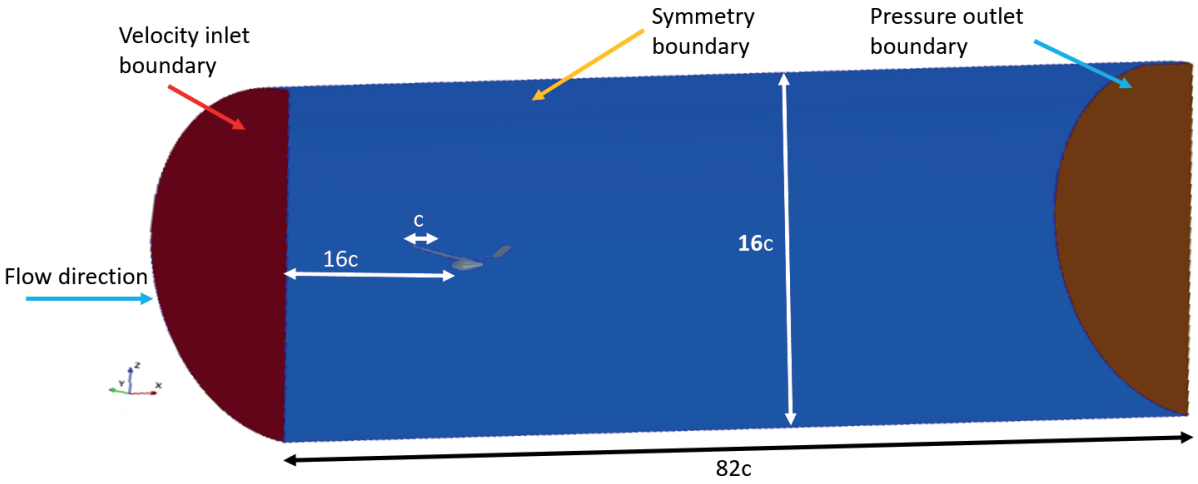

Figure 4.3: AREND configuration in the computational domain.

4.4 Mesh independence study

After the domain sizing, the next step was to determine the mesh size. Given the complex geometry due to interfaces such as wing-fuselage, booms-wing and an inverted V-tail plane-boom. The strategy was to create prism layers over the body of the aircraft to resolve the boundary layer.

Special attention was given to the regions of the flow field where complex flow physics are likely to occur. The important regions are identified to be the wing surface and its leading and trailing edges, booms-inverted V-tail, the wing tip region, the wake behind the wing tips, and the nose of the fuselage. Thus, special mesh density zones are assigned in the flow domain as previously shown in Chapter 3 Figure 3.3.

The wake region refinement which is $5c$ top and bottom of the fuselage and $57c$ down stream. The cells at the interface of the two meshes (prism layer and polyhedral) should have similar aspect ratio. Using the flat plate theory, the displacement thickness at the leading edge resolved using twenty five prism layers with advancing layer mesher, the boundary layer thickness $11mm$ and the size of the first cell is $0.02mm$ ($y^+ = 0.8$, $\Delta s = 0.015mm$ and $\delta = 0.005$). The wall $y^+ < 1$, criterion is the most preferred to capture the viscous sub-layers. The creation of the three dimensional boundary layer with good quality elements over the sharp and acute edges like trailing edges, wing tips, V-tail leading and trailing edges was a considerable challenge as the mesh quality became very poor in those regions.

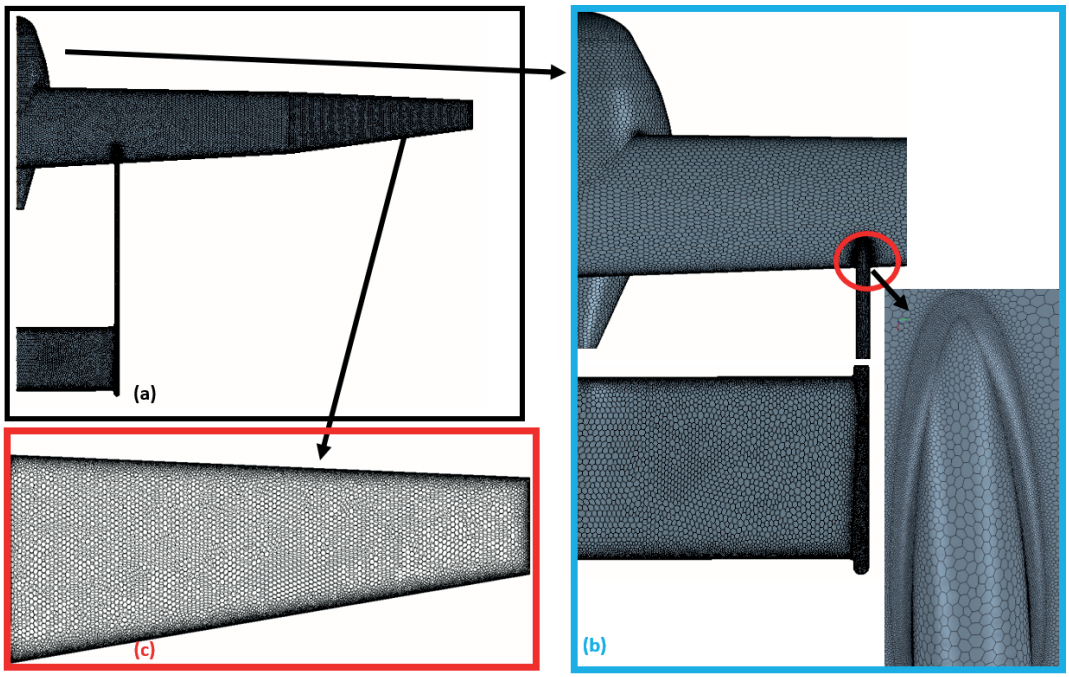

Figure 4.4: Mesh Refinement on the AREND (a) overall surface mesh (b) on outer wing (c) on wing-boom interface.

Figure 4.4 shows the surface mesh on the UAV. Figure 4.4(a) shows the transition of mesh from inboard wing to the outboard wing. The outboard wing cells are smaller and denser in order to capture the tip vortex and it was expected that AREND has tip stall. The wing leading and trailing edge have a finer mesh as compared to the surface of the wing as velocity changes are drastic at the leading and trailing edges. Therefore, more cells are required to capture the information as seen in Figure 4.4(c). Figure 4.4(b) highlights the wing-boom interface and fuselage-wing interface at the leading edge. It also shows the surface mesh on the inverted V-tail for which the leading and trailing edge mesh are much finer.

The mesh independent study is carried out for three different meshes for varying density of elements as in Figure 4.5. It can be seen that the global tendency is for the difference between the results to decrease when refining the mesh. Figure 4.5 details the number of cells and C_D. Equation 2.49 is satisfied hence, it is assumed that the mesh is adequate to capture the key flow features. Therefore, mesh independence is achieved.

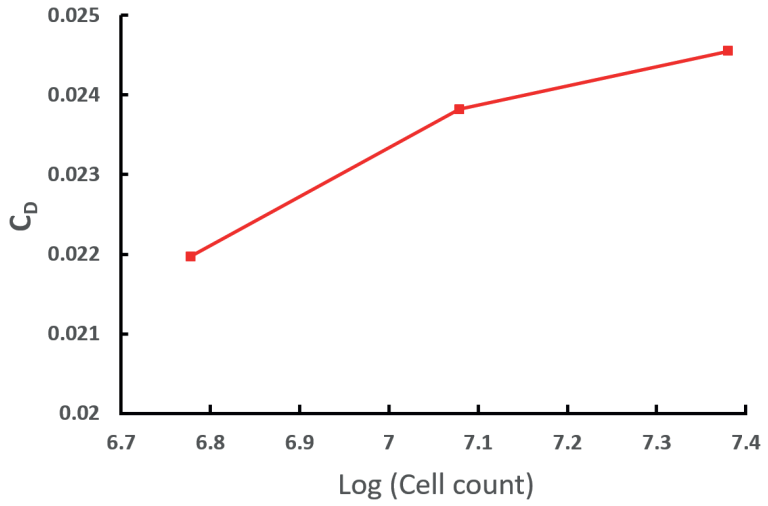

Figure 4.5: C_D against log of cell count for AREND at $\alpha = 0°$.

4.5 Comparison with vortex lattice method

The data obtained from the CFD is compared to outputs from AVL. In Figure 4.6, $C_L - \alpha$ curve shows a relative difference between the CFD data and AVL which is 7.1% at $\alpha = 8°$, and increases to 10.88% before stall. The minimum relative difference of 6.25% can be seen at $\alpha = 0°$. AVL does not take the airfoil thickness effects into account and it also does not resolve the flow separation. Furthermore, the flow is assumed to be inviscid hence, it can be concluded that it fails to predict the aerodynamic behaviour of the UAV in stall conditions and it is only suited for small α (due to the use of small perturbation theory) with little to no separation. The difference of 6.25% at $\alpha = 0°$ is due to fuselage and booms that were not modeled in the AVL. Due to their omission AVL predicts a larger C_L.

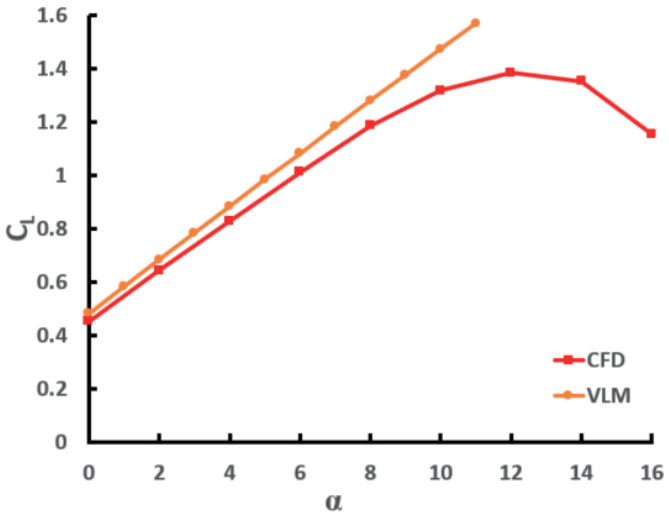

Figure 4.6: Comparison between AVL and CFD results of C_L versus α at $Re = 5 \times 10^5$.

The pitching moment curve $C_m - \alpha$, is plotted in Figure 4.7, The relative difference at $\alpha = 8°$ is 9.1% but this increases to 14.8% at $\alpha = 10°$ as it approaches stall and flow separation occurs. The curves seem to converge to a common point at $\alpha = 0°$. C_m around $\alpha = 0°$ matches the CFD results. Overall, both approaches show $C_{m,\alpha}$ is negative and therefore, the UAV has static longitudinal stability.

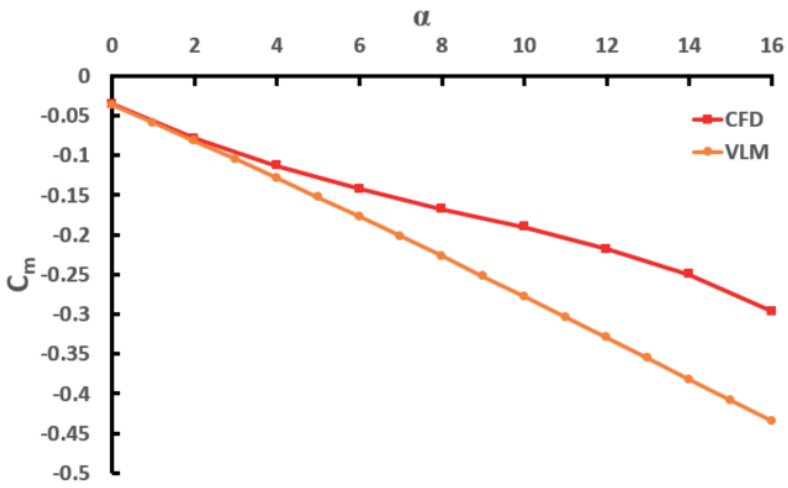

Figure 4.7: Comparison between AVL and CFD results of C_m versus α at $Re = 5 \times 10^5$.

The AREND CFD is within 10% of the AVL results in the linear region for small α before

stall even though the booms and the fuselage were not modeled. As a result both method of modelling, CFD and AVL, verify each other over the α range of interest.

4.6 Flow over fuselage and wings

4.6.1 Wake profile

Normalized streamwise velocity, U_X/U is located on the first prism layer cell in the boundary layer that spans the surface of the body (CD-Adapco, 2016; Smith, 2017). Figure 4.8 shows U_X/U over the fuselage center line showing regions of reverse flow ($U_X/U < 0$). These regions are at $x/l = 0.1$ (due to curvature of the nose geometry), between $x/l = 0.47$ and $x/l = 0.57$ and $x/l = 0.66$ (mainly due to wing and fuselage interaction) and $x/l = 0.78$ (separation at trailing edge of the wing) of fuselage center line. Figure 4.8 also shows the separation regions as negative (reversed) normalized velocities. The following figures use cell relative velocity (which is a function of surface shear stress) to identify flow over wings. Fuselage geometry needs to be optimized to avoid local separations zones, and minimize wing fuselage interaction.

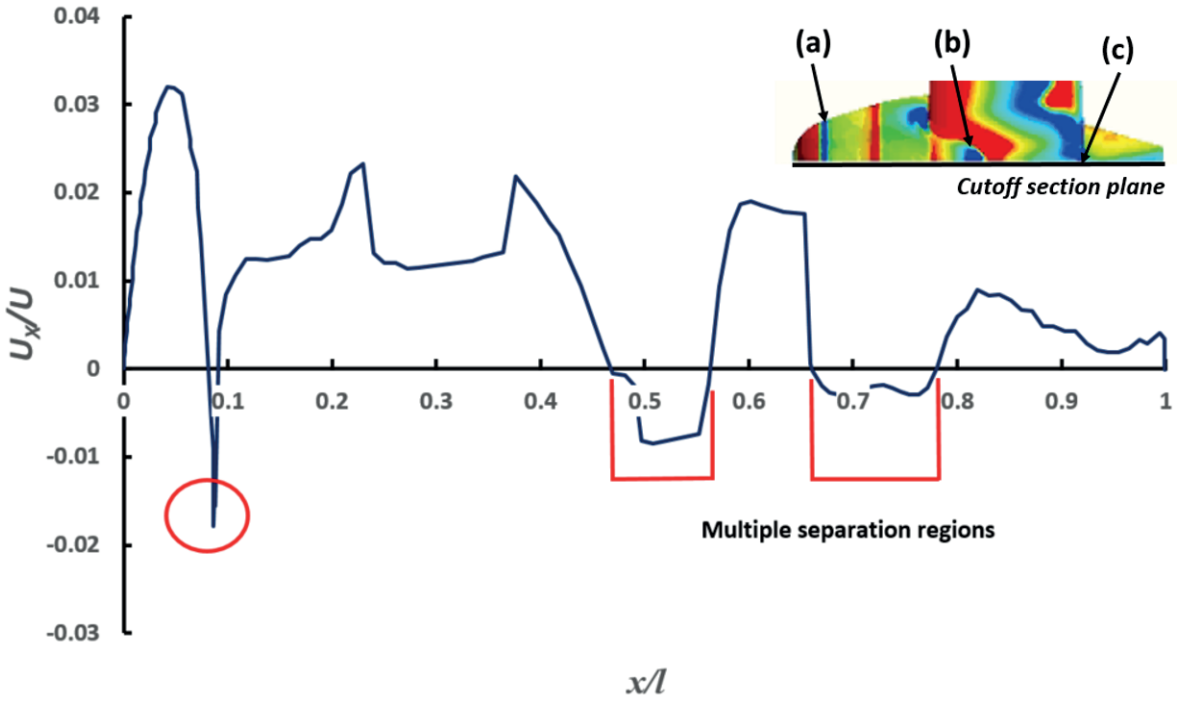

Figure 4.8: Normalised U_X/U velocity plot at fuselage centerline showing separation zones.

Figure 4.9 shows how the airframe undergoes stall. It is seen that the wing undergoes tip stall making the control surfaces ineffective. At $\alpha = 12°$, it can be seen that the wing undergoes trailing edge stall. As the α is increased the reversed flow area becomes larger and moves towards the leading edge. However, due to the small chord length at the tip this results in stalled flow over the entire wing tip region. This tip stall will induce a rolling moment as the AREND configuration approaches stall due to unsteady behavior. The degree of control that the ailerons can exert over the roll becomes less and aileron control authority is lost.

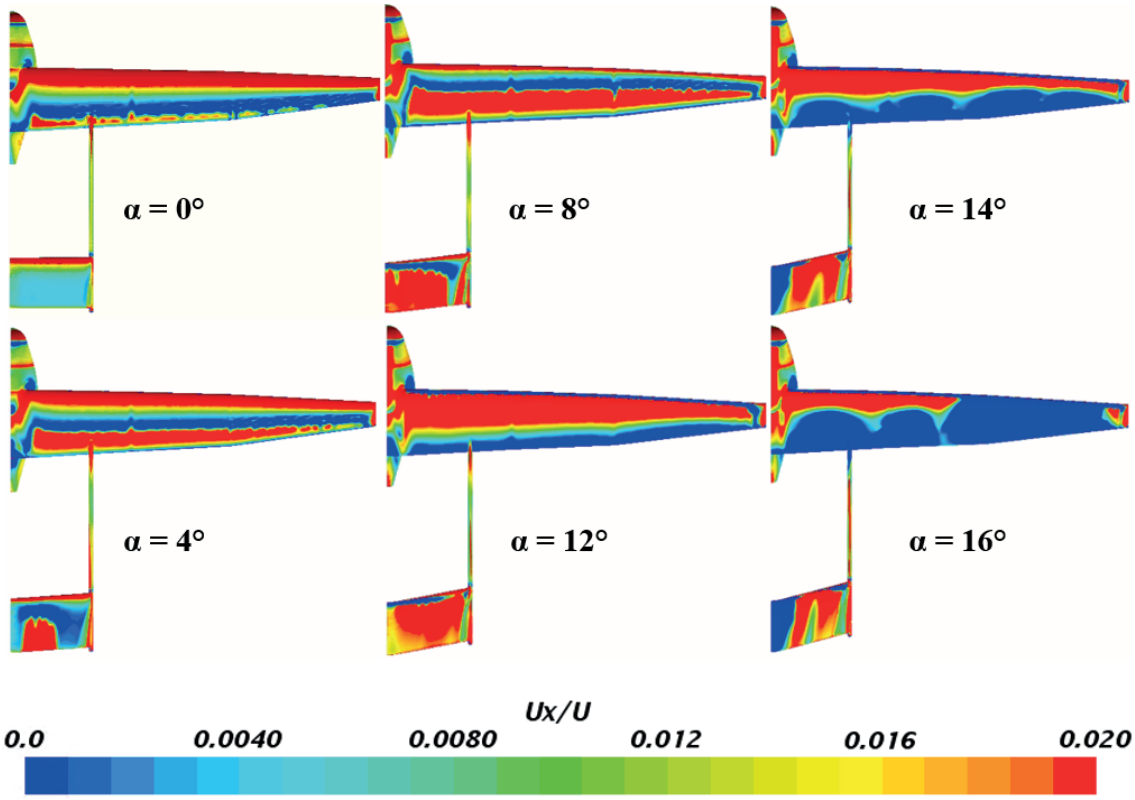

Figure 4.9: Flow over AREND over range of α showing stall patterns.

Figure 4.10 shows the wake of the fuselage which has two flow features: Features A and B which highlight flow physics over different parts of the drone. Note that the actual aircraft has a pusher propeller that effectively creates a low pressure sink. This would pull the upstream air and twist the streamlines. The elongated streamlines would form a twisted conical shape. However, the CFD simulation here only represents the unpowered AREND configuration. Feature A, shows the vortices at the aft of fuselage, whereas Feature B is the wake from the wing. It shows the separation effects due to wing separation and wing fuselage interaction.

In Feature B, as the α increases, the flow over the top of the airfoil starts to decelerate more. This contrasts observations in Feature A where the flow starts to shift down with α. This happens mainly due to the flow over bottom of the fuselage that starts to accelerate which gives the boundary layer greater momentum. We also see that the wake area increases (length in one D) as the α is increased. On increasing α, the gap between Features A and B becomes bigger as the flow over the wing starts to separate as shown in Figure 4.11. This is due to the stall effects over the wing that starts to dominate the overall flowfield as compared to the aft fuselage body. A well-designed aerodynamic cowling could potentially reduce the wake profile.

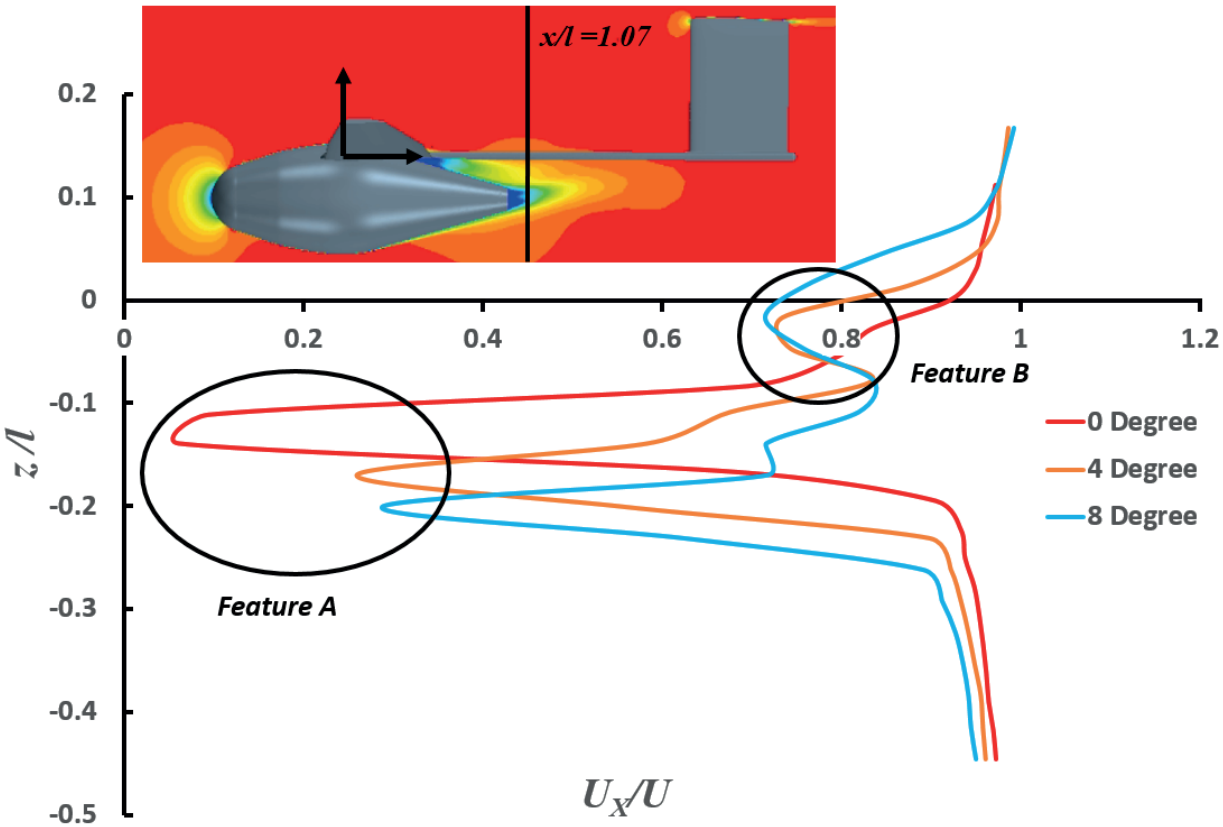

Figure 4.10: Normailzed wake velocity profile of AREND for different α.

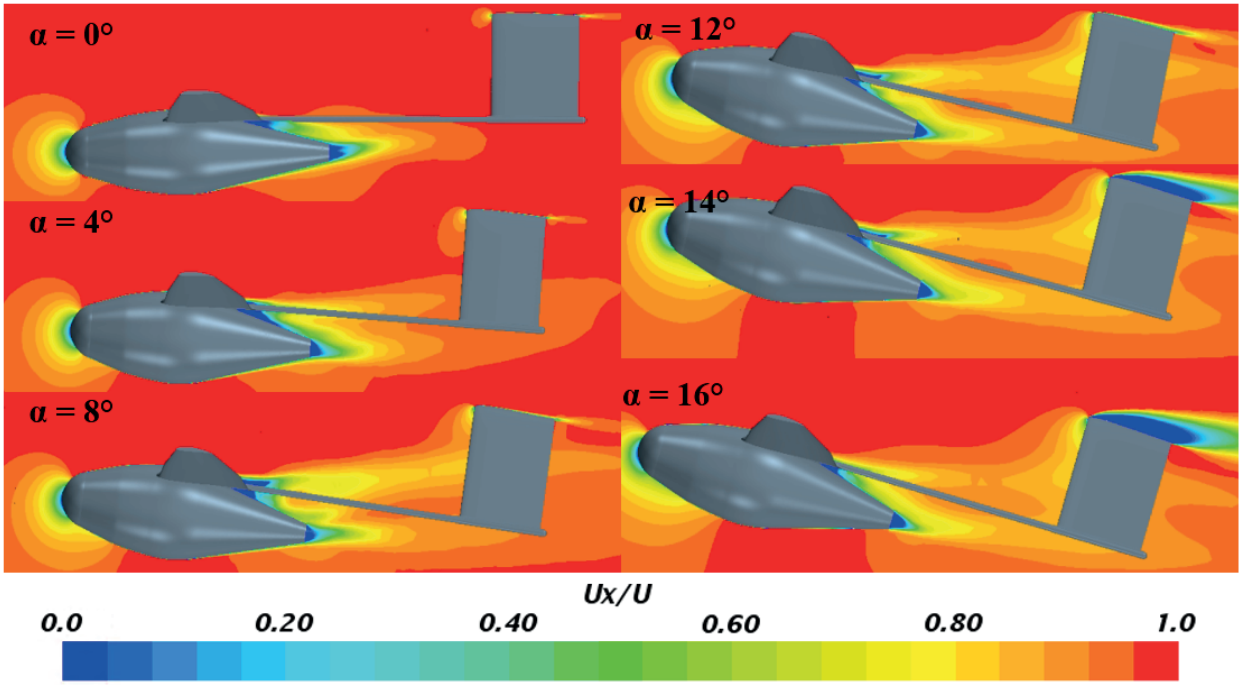

Figure 4.11: Normalized U_X/U velocity contour plot centerline of AREND fuselage visual representation of two wake features.

4.6.2 Downwash due to the wing

Figure 4.12 and 4.13 show the vertical flow velocities through flow field visualisation along a slice taken over the fuselage centreline and spanwise variation of downwash (taken at $x/l = 1.19$ and $z/r = -1.44$) respectively. In Figure 4.12 it is evident that the flow field aft of the fuselage is dominated by upwash at low α. With increasing α, this upwash region is gradually squeezed by regions of flow separation over the wing and the aft fuselage. Figure 4.13 shows that the expected increase in spanwise downwash velocities only occur upto the point where the aircraft begins to stall ($\alpha = 8°$). After the stall point, there is no significant increase in the downwash velocity.

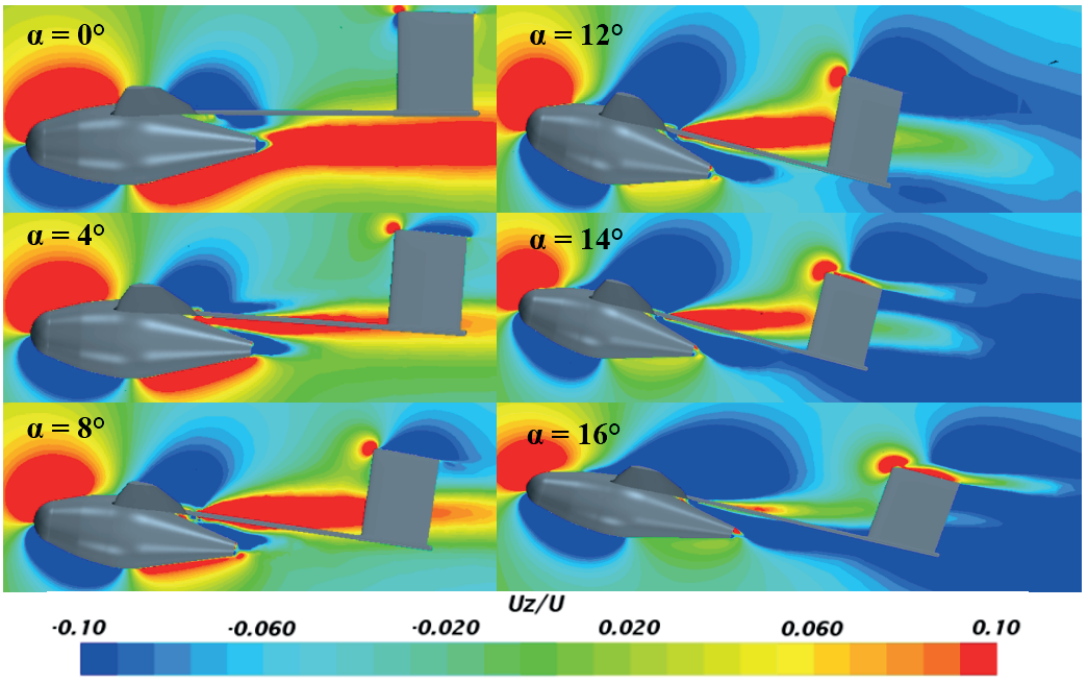

Figure 4.12: Normalized U_Z/U velocity contour plot centerline of AREND fuselage visual representation of upwash and downwash regions.

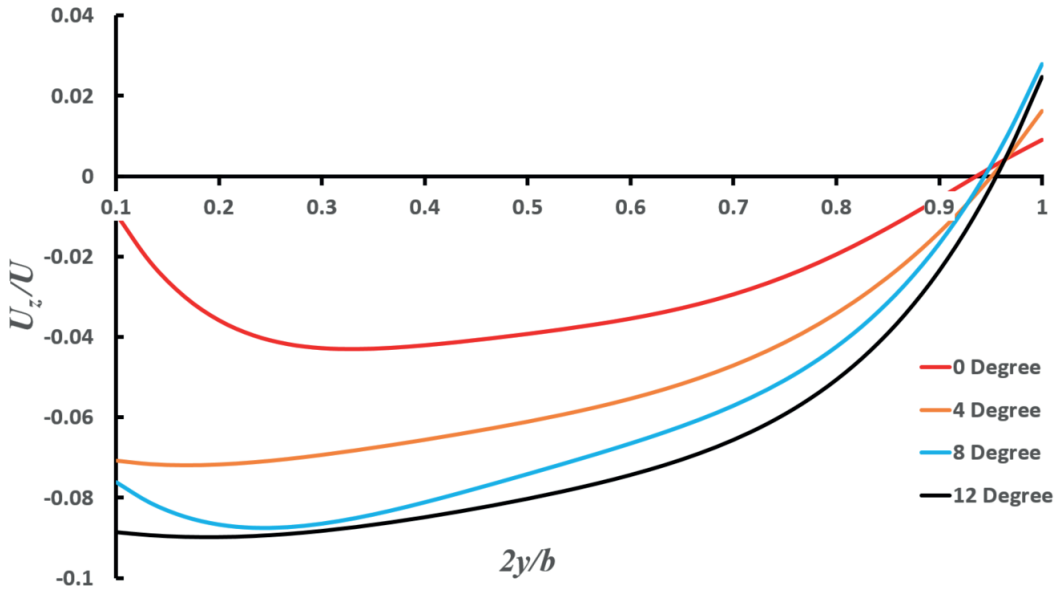

Figure 4.13: Downwash profile over normalized $2y/b$ of the AREND wing plotted for different α.

4.6.3 Global aerodynamics

4.6.3.1 Lift coefficient curve The AREND C_L and its variation with α and β in Figure 4.14 shows that stall occurs at $\alpha = 12°$ for small β where the stall point changes from $\alpha = 12°$ to $\alpha = 10°$ at higher β. The lift curve slope, $C_{L\alpha}$ is $0.0921/°$ or $5.28/rad$ and $C_{L0} = 0.4524$. It is seen that the $C_{L\alpha}$ is linear until $\alpha = 8°$ and non-linear after that. The non-linear $C_{L\alpha}$ is an indicative of flow separation prevailing on the body. The $C_{L\alpha}$ decreases by $4.63/rad$ at $\beta = 15°$ which is approximately 12%. β influences the $C_{L\alpha}$ especially at high α. It is seen that the $C_{L\alpha}$ remains the same for $\beta = 5°$ as it can still be considered to be a small angle. The effect of the β can only be seen after the stall point which is due to the flow coming at an angle resulting in a decrease in the lift component and increase in the drag component.

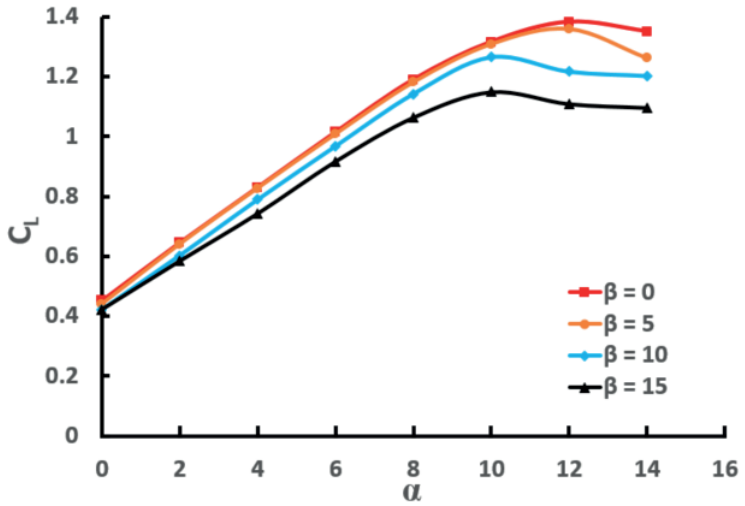

Figure 4.14: C_L versus α with different β for AREND at $Re = 5 \times 10^5$.

4.6.3.2 Drag polar The minimum C_D is at $\alpha = 0°$. In Figure 4.15 it is seen that the C_D follows the same trend as that at $\beta = 0°$. It is also seen that the stall starts at $C_L = 1.4$ for $\beta = 0°$ and $\alpha = 12°$ until $\beta = 5°$, whereas for higher angles of β it is seen that the stall angle shifts which can be spotted clearly when the lift decreases and the drag increases. The laminar bucket gets smaller and smaller as the β increases. The laminar bucket is essentially where the flow remains attached to the body and the onset of stall drastically increases drag.

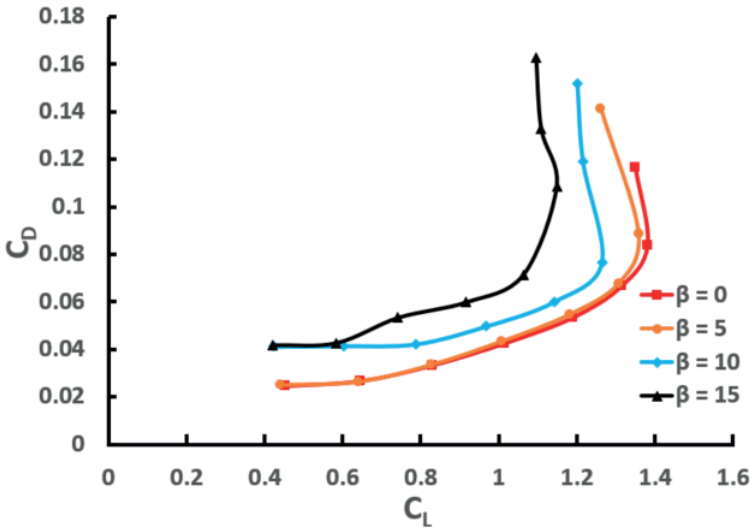

Figure 4.15: C_D versus α with different β for AREND at $Re = 5 \times 10^5$.

4.6.4 Static stability analysis

4.6.4.1 Longitudinal static stability In Figure 4.16 it can be seen that the $C_{m,\alpha}$ slope is$-1.112/rad$ to $-0.94/rad$. This decreases by 15.46% when $\beta = 15°$. Therefore, as β increases the aircraft becomes less statically stable but it is still far from becoming unstable. It is seen that the β does not change the C_m until there is flow separation at very large side slip angles; especially after stall. It is noted that β does not influence the $C_{m\alpha}$ gradient but influences C_{m0}. It is clear that the AREND configuration is robust to side slip in terms of longitudinal stability. The fact that the curves are in the negative C_m zone indicates that response to any atmospheric disturbance is to return back to trim conditions. The negative slope of the graph satisfies the second condition for the longitudinal static stability as stated in Equation 2.40. The C_{m0} of the aircraft is -0.059.

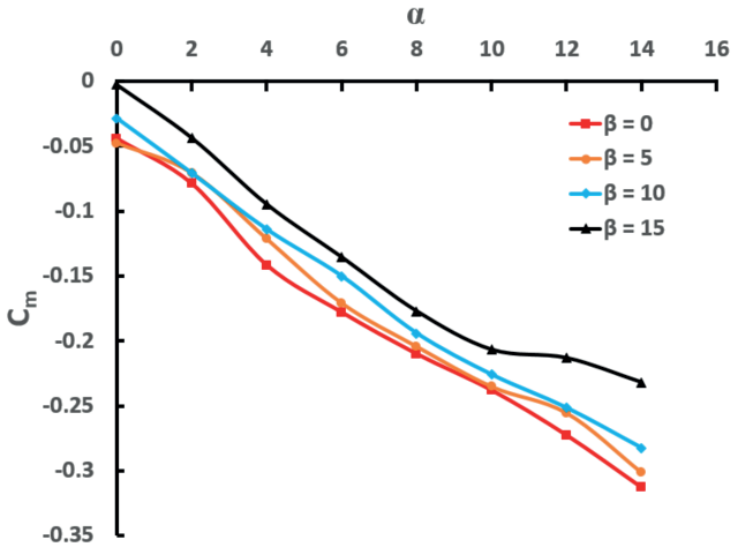

Figure 4.16: C_m versus α with different β for AREND at $Re = 5 \times 10^5$.

4.6.4.2 Lateral static stability (a) Yaw derivative: In the yawing moment coefficient graph, Figure 4.17, it is seen that the slope $C_{n,\alpha}$ is positive which is required to have a statically stable airplane. It is noted that the lateral static stability decreases only for the higher post stall α. It is also seen that the UAV retains directional stability even after stall.

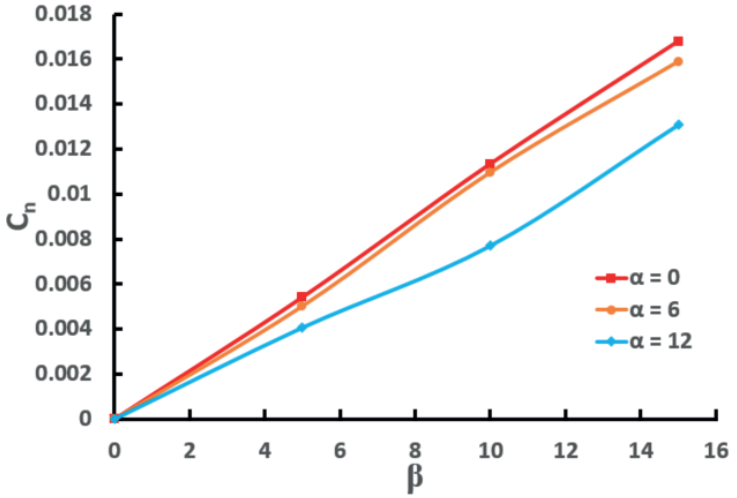

Figure 4.17: C_n versus β with different α for AREND at Re =5×10^5.

(b) Roll derivative: A first glance at Figure 4.18 shows that the rolling moment, $C_{l,\beta}$ due to β at $\alpha = 12°$ is concerning due to the sign change. However, at stall the magnitude of instability is small and at $\alpha = 12°$ the flow is separated resulting in large residuals in the CFD simulations which introduces a lot of uncertainties. Moreover, for $\alpha < 6°$, the UAV has enough roll stability.

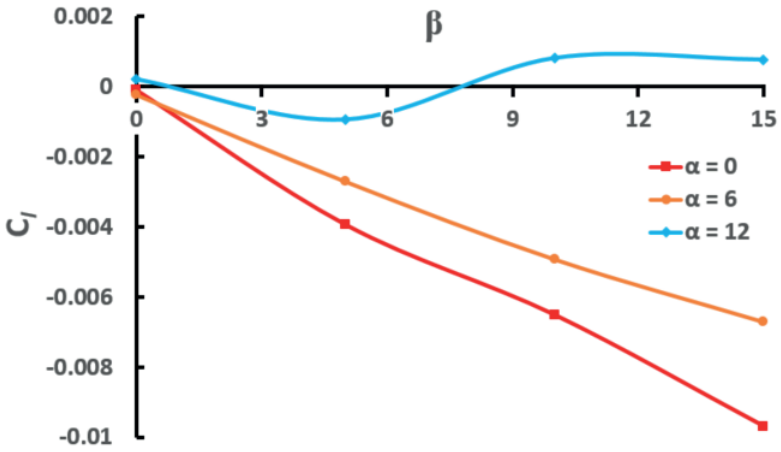

Figure 4.18: C_l versus β with different α for AREND at $Re = 5 \times 10^5$.

(c) Side force coefficient: For completeness, the side force with respect to β at different α is plotted in Figure 4.19 to indicate how much the aircraft may drift in side wind conditions. It is seen that as α increases, $C_{Y,\beta}$ decreases which means that the UAV displacement is higher for the same side wind conditions.

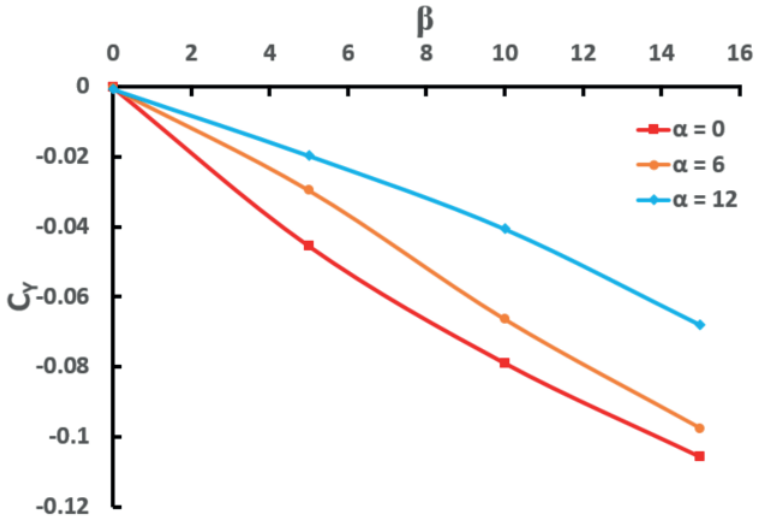

Figure 4.19: C_Y versus β with different α for AREND at $Re = 5 \times 10^5$.

4.7 Conclusion

A computational domain size has been identified with the relevant boundary condition. A validated mesh was used for the relatively complex AREND UAV geometry along with a suitable turbulence model (SST $k-\omega$) coupled with transition model ($\gamma - Re_\theta$). The CFD was for steady state conditions only so there would be limitations for results at high α. The results are presented here as an evaluation of trends rather than exact estimates. CFD data was compared with AVL and the difference was under 10% before stall. The fuselage geometry needs to be optimized to avoid local separations zones, and minimize wing fuselage interaction. Aerodynamic cowling can be used to reduce the wake profile. Simulation results show that the UAV undergoes wing trailing edge stall that leads to the tip stall starting at $\alpha = 12°$. Considering the behaviour of aerodynamic moments with variations in angle of attack and sideslip, it was found that the design is static stable. However, this work effectively established the specifications for the aerodynamic coefficients (as shown in Figure 4.14-4.19) which were needed to design a new wing. The two main specifications were that cruise lift coefficient, $C_{L,Cruise} \geq 0.66$ and $C_{m\alpha} \leq -1.112/rad$ for the new wing.

5 Design of wing with non-elliptic lift distribution

5.1 Introduction

The objective of the work presented in this chapter is to design a fuselage-wing configuration that produces a non-elliptic lift distribution. The new aircraft must meet, if not exceed, the flying performance of AREND. Prandtl and Horten brothers derived the equations independently with its limitations, Bragado Aldana and Lone (2019) developed the MATLAB code which is used in this study. The aerodynamic and flight dynamic properties were extracted using modified lifting line theory without span limitation (coded by Bragado Aldana and Lone (2019)). The study uses the original AREND wing with elliptic loading as a baseline and compares its characteristics to new wing designs with non-elliptic lift distributions using the method developed by Prandtl in 1933. Thereafter, a wing planform was generated with variable twist and chord lengths. To achieve the required longitudinal static stability, a sweep study was conducted that highlighted the effect of sweep on stability and compared the static margin for sweep angles with different CG locations using AVL.

5.2 Requirements

The new configuration aims to reduce drag and improve stability while removing the need for empennage and booms. The new configuration is required to carry $20kg$ MTOW which allows for extra weight and fly at $120m$ ASL, with a cruise velocity of $20m/s$. The wing span of new configuration is restricted to $4.25m$. The NELD wing location is $346mm$ away from the nose and the CG point is also kept the same as AREND.

5.3 Airfoil selection for NELD

A pre-selection of airfoils was made and the listed airfoils were analysed in XFLR5 (which uses XFOIL for airfoil analysis) with simulation conditions of velocity $20m/s$, a characteristic length of $0.4m$, a density of $1.18415kg/m^3$ and dynamic viscosity μ of $1.8046 \times 10^{-5}Pa.s$ which yields a low Reynolds number of $Re = 5.25 \times 10^5$. The analysis was performed between $-8° \leq \alpha \leq 16°$ in $2°$ intervals. A general criteria was laid out for selection of airfoils: The most crucial for just the fuselage-wing configuration, is airfoils with small C_{m0} or zero is preferable (Nickel and Wohlfahrt, 1994). The design for flying wing depends on the longitudinal stability as there is no tail to provide the necessary pitching moment in trim. C_m value of airfoil should be between $-0.03 \leq C_m \leq 0.01$ for the range of $0° \leq \alpha \leq 12°$. The $C_{l,max}$ should be between 1.2 and 1.4 and it will reduce in a 3D wing, hence higher $C_{l,max}$ values are favourable. Stall angle of the airfoil should be more than $12°$. The airfoils with low $C_{d,min}$, and a broad laminar bucket are preferred.

Note that Drela (1989) states that XFOIL does not work effectively over Reynolds number of $Re = 5 \times 10^5$ due to the simplified panel method based solver used in the interest of cheap computational cost. This means complex flow features such as laminar separation bubbles which cause instabilities in the flow are not modeled.

Comparing data from the Table 5.1, four airfoils were chosen, the driving criteria was C_{m0} between the range $-0.03 \leq C_{m0} \leq 0.01$ were selected as longitudinal stability parameter is the most important. The four airfoils selected in order of preference were, MH45, MH46, FX-05H-126 and Marske. Only the graphs for selected airfoils are shown here. Figure 5.1 shows the lift coefficient curve, MH 45 has the maximum $C_{l,max}$ of 1.28 at $14°$, FX-05H-126 has a $C_{l,max}$ of 1.27 at $9°$, MH 60 has $C_{l,max}$ of 1.23 at $12°$ and Marske has a $C_{l,max}$ of 1.07 at $9°$. MH 45 and MH 60 have high $C_{l,max}$ and also stall after $12°$, where as FX-05H-126 and Marske stall early at $9°$. Figure 5.2 shows the $C_m - \alpha$ curve. Upon comparison, it is clear that MH 45 and MH 60 satisfy the criteria ($-0.03 \leq C_m \leq 0.01$ for the entire $0° \leq \alpha \leq 12°$). Figure 5.3 shows the drag polar,

Table 5.1: Airfoil analysed using XFLR–5 at $Re = 5.25 \times 10^5$.

Airfoil	$C_{l,max}$	C_{m0}	Stall[°]
E186	1	0.025	11
Fauvel	1.33	0.04	12
FX-05H-126	1.27	-0.016	9
GOE 744	1.54	-0.035	14
MH 45	1.28	-0.0026	14
MH49	1.1	0.1	12
MH 60	1.23	-0.005	12
MH70	1.4	-0.04	14
MUE139	1.5	-0.04	14
Marske	1.07	0.0084	9

the laminar drag bucket of MH 45 is slightly larger as compared to MH 60. After comparing all the data it was concluded that MH 45 should be the airfoil used for further analysis.

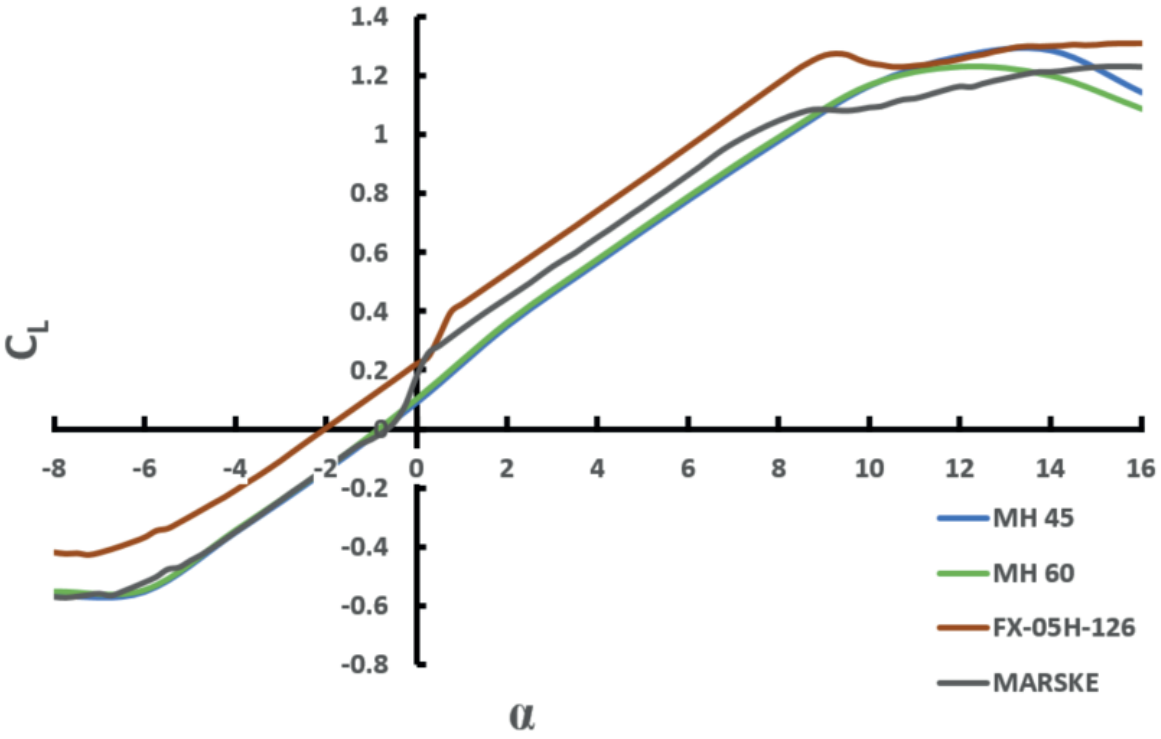

Figure 5.1: $C_{l\alpha}$ curves for airfoils at $Re = 5.25 \times 10^5$.

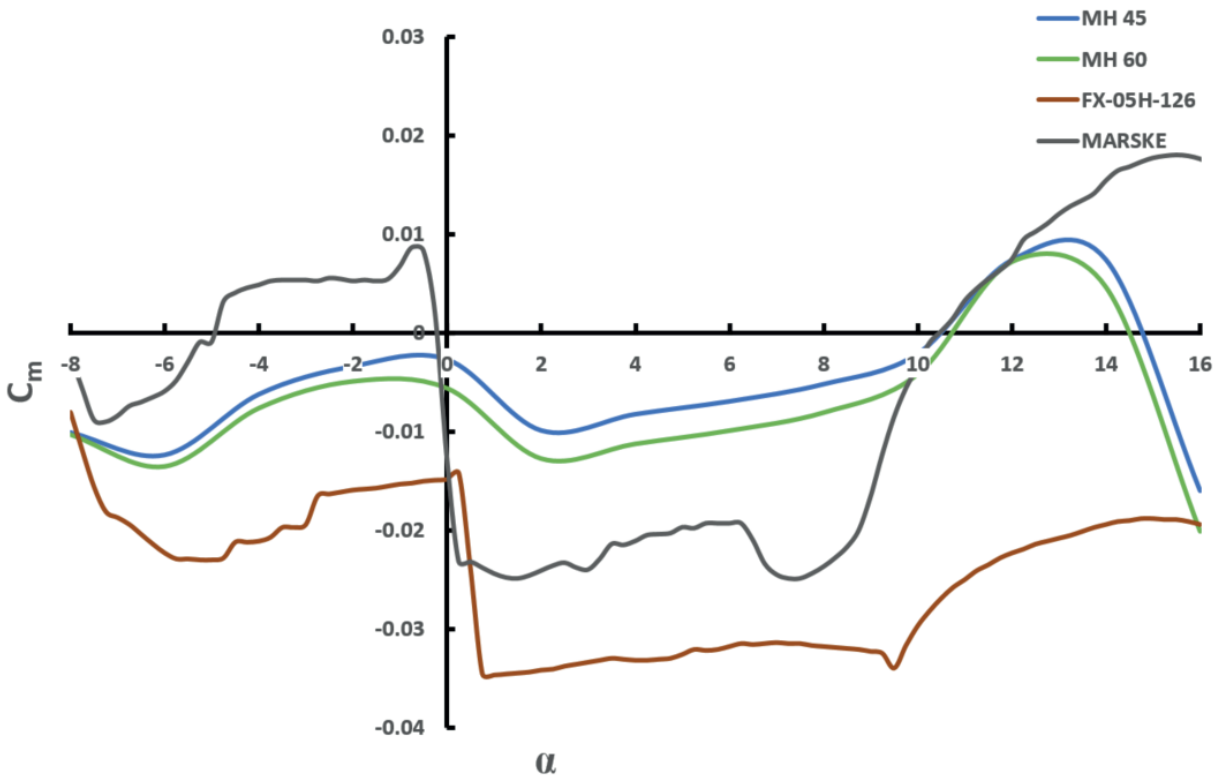

Figure 5.2: C_m against α for airfoils at $Re = 5.25 \times 10^5$.

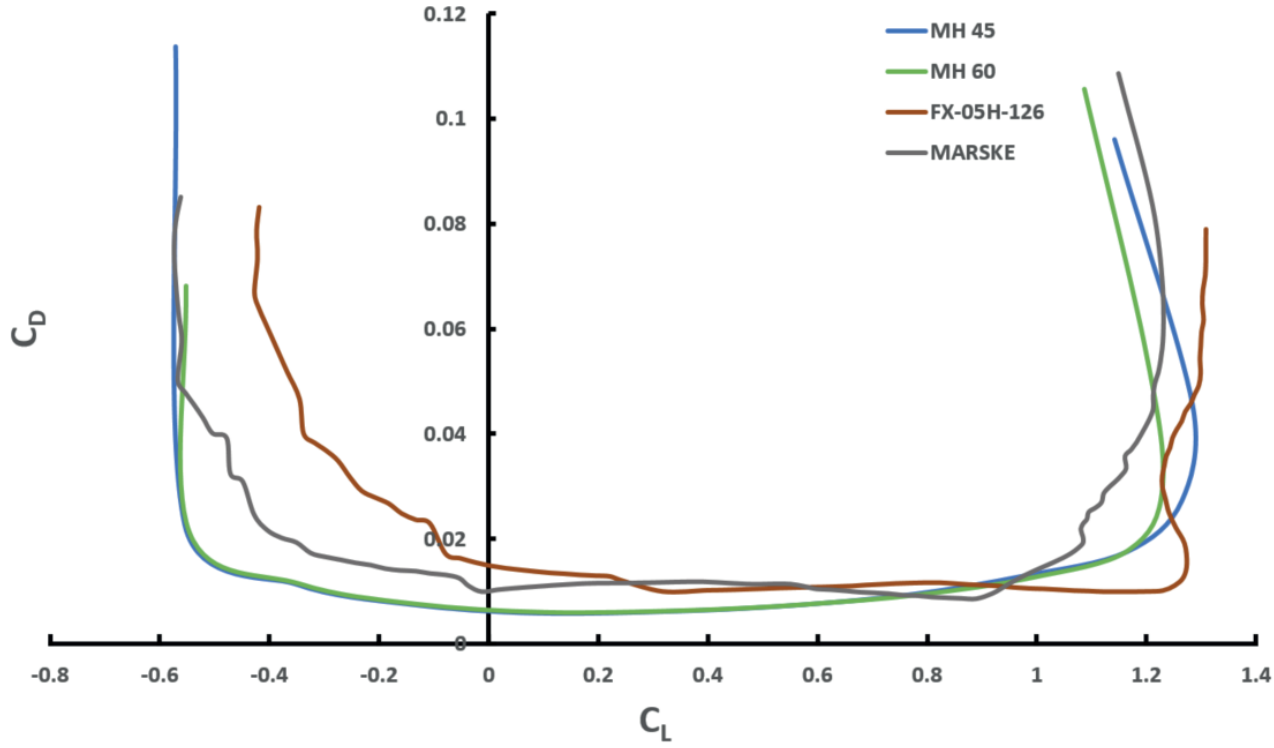

Figure 5.3: Drag polar curves for airfoils at $Re = 5.25 \times 10^5$.

5.4 Design methodology for NELD

5.4.1 Mathematical model

MH 45 is selected as the airfoil for the non-elliptic lift distribution wing. Now a wing planform is required, from the discussion of Prandtl's non-elliptical lift distribution derivations in Section 2.3, the main outcomes are listed here to show how the modifications to the lifting line equations (modified LLT) can incorporate them. Prandtl's circulation equation is:

$$\Gamma(y) = \Gamma_{max}\left(1 - \mu_P\left(\frac{2y}{br_P}\right)^2\right)\sqrt{1 - \left(\frac{2y}{br_P}\right)^2} \tag{5.1}$$

where μ_P is the shape of the distribution. Note that $\mu_P = 0$ for elliptic lift distribution and $\mu_P = 1$ for non-elliptic distribution therefore,

$$\Gamma(y) = \Gamma_{max}\left(1 - \left(\frac{2y}{br_P}\right)^2\right)^{3/2} \tag{5.2}$$

The mathematical model requires maximum circulation, Γ_{max} at the center which is obtained via the lift equation:

$$L = \int_{-\frac{br}{2}}^{-\frac{br}{2}} \rho U \Gamma(y) dy \tag{5.3}$$

after integrating we get,

$$L = \frac{3\pi}{8}\left(\rho U \Gamma_{max}\frac{br_P}{2}\right) \tag{5.4}$$

$$\Gamma_{max} = \frac{16L}{3\pi\rho U b r_P} \tag{5.5}$$

Now the circulation derivative $\frac{d\Gamma(y)}{dy}$ can be extracted as:

$$\frac{d\Gamma(y)}{dy} = -3\Gamma_{max}\frac{y}{\left(\frac{br_P}{2}\right)^2}\left(1 - \left(\frac{2y}{br_P}\right)^2\right)^{1/2} \tag{5.6}$$

Induced downwash and twist distribution are then obtained:

$$w_i = \frac{L^2}{9\pi\rho U^2 r_P^2} \tag{5.7}$$

$$\alpha_t(y) = \frac{2\Gamma(y)}{m_0(y)c(y)U} + \frac{1}{4\pi U}\int_{-b/2}^{b/2}\frac{\frac{d\Gamma(y_0)}{dy}dy_0}{y - y_0} + \alpha_{L0}(y) \tag{5.8}$$

After modifying the lifting line equations to incorporate the non-elliptic lift distribution, it is executed in Matlab R2018. The code will be tested with values similar to AREND case in order to make comparisons. It means that the values of lift, speed, aspect ratio and taper ratio are taken similar to the AREND geometry.

5.4.2 Algorithm implementation

The code first converts the AREND wing geometric parameters into an elliptic lift distribution and then computes its aerodynamic characteristics which is used as a baseline. Next, the boundary conditions for NELD are checked. Then the number of stations and valid span ratio is set after which number of stations, $n = 500$ is set.

Modified lifting line theory is applied to compute circulation distributions that create the resulting downwash distributions. This is used to calculate induced angle of attack. After which, the twist distribution and chord lengths for each station are computed. Local and global aerodynamic characteristics are then computed from circulation and induced drag. The algorithmic flow chart implemented here is shown in Figure 5.4.

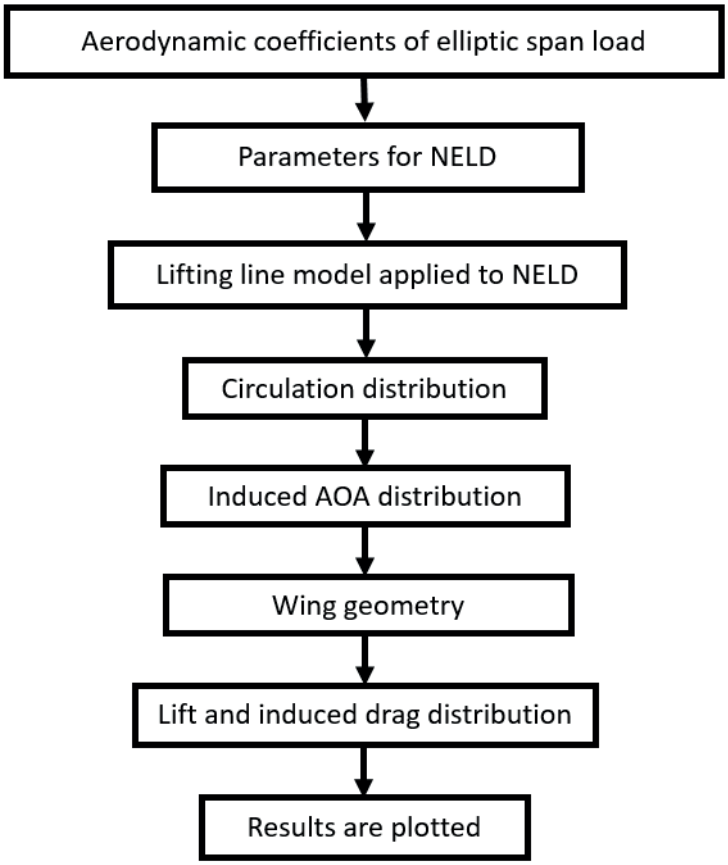

Figure 5.4: Flow chart for Non-elliptic lift distribution.

Now that a twist distribution is obtained along with the chord length for the wing planform, sweep needs to be added for static longitudinal stability. Figure 5.5 shows the flow chart used for sweep analysis. Firstly, all input variables are defined such as geometry, mass and flight condition. Secondly, the twist distribution from the NELD code is used and sweep angle is defined ranging from $5° \leq \alpha \leq 25°$ (Nickel and Wohlfahrt, 1994) with 5° intervals and the CG was moved from 20% MAC to 100% of the MAC. An effective chord length was used in the analysis.

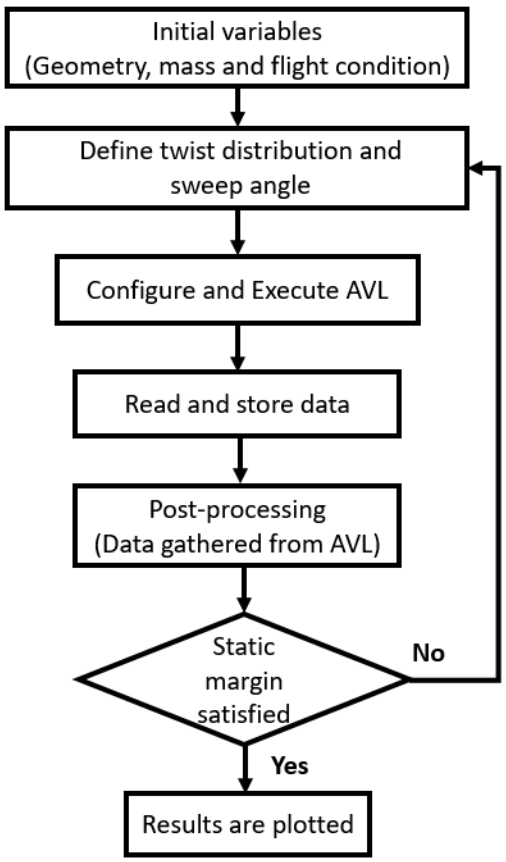

Figure 5.5: Flow chart for sweep analysis using AVL.

5.5 Results

The following subsection compares the code with AVL and shows the aerodynamic and geometric characteristics of the non-elliptic lift distribution. In Figures 5.6 to 5.9 the normalised span length of the elliptic wing is 1 whereas for NELD it is 1.22. The latter is due to the span extension required for applying the Prandtl (1933) method. It should also be noted that the span of the new NELD wing is required to be the same as that of the baseline AREND wing. Therefore, Prandtl's (1933) method was applied to a version of the AREND wing that was scaled down by 22%. This ensured that after applying the span extension prescribed by Prandtl, a wing with the required span is generated.

5.5.1 Verification with AVL

This section presents verification of the code with AVL. In Figure 5.6, lift distributions over the span are presented for both NELD algorithm and the AVL output. The maximum difference is 6.25% at inboard wing with high twist angles. The difference is mostly due to the techniques utilized, since AVL separates the wing's surface into panels in both span and chord directions, with a horseshoe vortex in each panel whereas, the code uses Prandtl's linear lifting line equations modified for non-elliptic lift distribution.

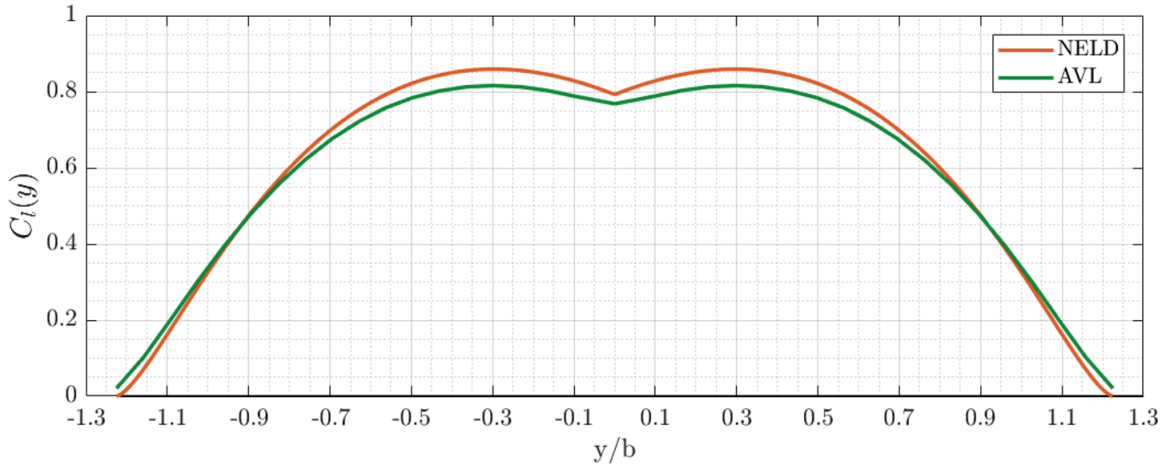

Figure 5.6: Verification of non-elliptic lift distribution code with AVL.

5.5.2 Induced downwash

The observed upwash for NELD as shown in Figure 5.7 at the outboard wing creates an induced thrust, which tilts the resultant aerodynamic force forwards and produces negative local induced drag (Bowers et al., 2016). The upwash happens at 70% half span which correlates with observations from both Prandtl (1933) and Horten brothers (1984).

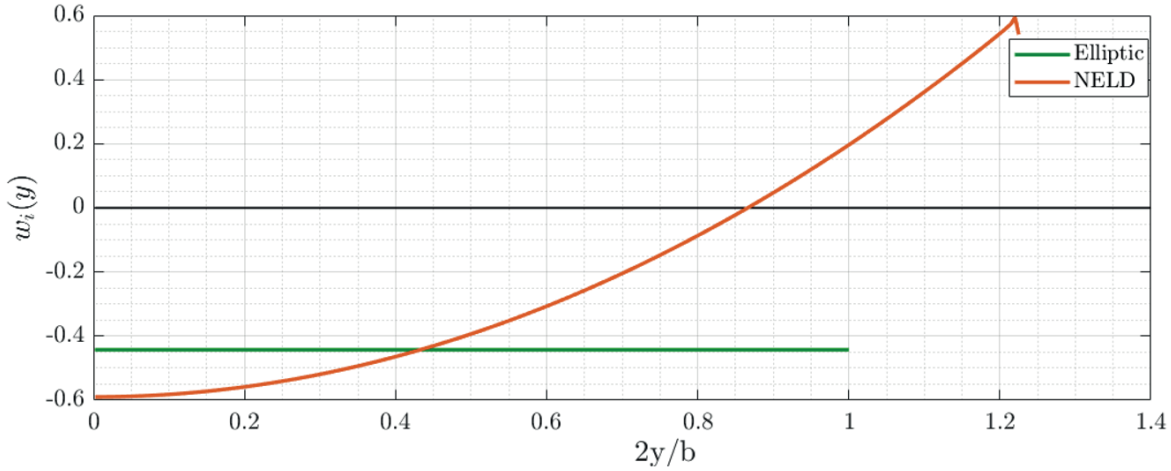

Figure 5.7: Induced downwash over half span for elliptic and non-elliptic lift distribution (NELD).

5.5.3 Twist distribution

The twist distribution over the NELD wing is shown in Figure 5.8. The twist varies from 8.5° to −1.6° over the span. The inboard 40% of the half span has the highest wing twist and after that the twist decreases almost exponentially until −1.6° at the tip. Here, the upper and lower limits of twist angles were defined by the total C_L specification and the spanwise variation of twist is an output of Prandtl's (1933) method.

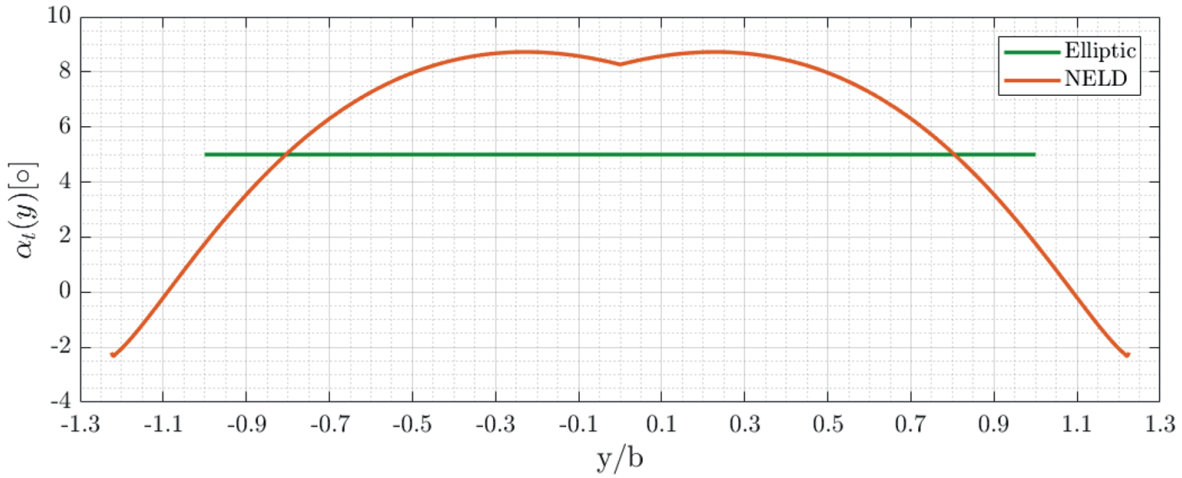

Figure 5.8: Twist over the wing span.

5.5.4 Chord distribution

The chord distribution is maximum at the root and mimimum at the wing tip, as seen in Figure 5.9. When this is inspected in conjunction with the twist distribution (Figure 5.8) it can be concluded that the inboard wing (upto 40% half span) produces the maximum lift while the smallest amount of force is generated at the wing tips. This is beneficial for aerodynamics and structural considerations. Low lift coefficient translates to low pressure gradients between the upper and the lower surfaces. Thus reducing the strength of the tip vortex and reducing the aerodynamic forces at the wing tips. This helps in shedding some structural weight as the overall wing root bending moment is reduced.

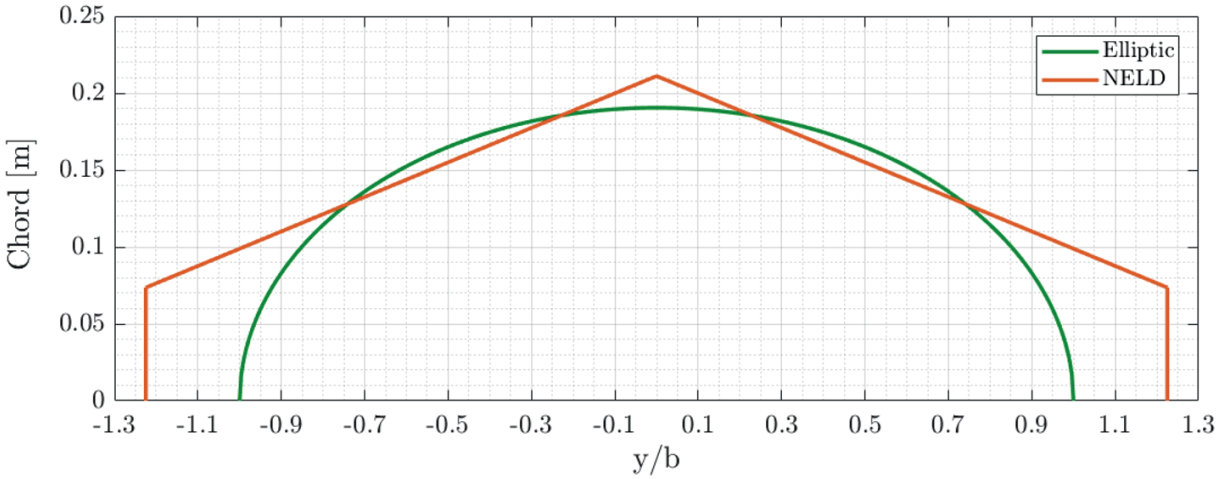

Figure 5.9: Planform for Elliptic and Non-elliptic lift distribution.

5.5.5 Stability analysis with wing sweep

The AREND UAV has a limited CG range due to which extra weights are added to have a nose down pitching moment during flight tests. To extend the CG range for the NELD configuration, it is important to select a suitable sweep angle for the wing to ensure longitudinal static stability. The wider CG range will also help to trim the UAV as it does not have a tail boom. Nickel and Wohlfahrt (1994) recommend that for a flying wing the desirable sweep is between $10° \leq \Lambda \leq 25°$ and desired static margin between $16\% \leq K_n \leq 18\%$. If the UAV has too much static margin it becomes sluggish during manoeuvers. Typical range of CG is 10% to 40% of mean chord or

MAC (Cook, 2013). Design requirements were defined for selecting a desirable sweep angle. One of the requirements was that the range of the CG can be anywhere from 0 to 100% of MAC with a minimum of 5% static margin while ensuring overall lift does not decrease by more than 10%.

In Figure 5.10, it is evident that a sweep of 15° sits in the goldilocks region. Anything below 15° will be unsuitable and anything higher than 15° will have a significant impact on aerodynamics. Hence, a sweep of 15° was chosen with the least static margin of 5.42% when CG was at 100% MAC and the maximum static margin of 95.43% when CG was at 10% MAC. It gives us a wide range of CG to choose from and does not require the need for adding extra weight as we do currently on AREND during flight tests to ensure a sufficient static margin. The advantage of extending the CG range is two folds: firstly, it makes the UAV stable and secondly, it helps with trimming the UAV.

AVL analysis produced pitch, yaw and roll stability parameters as $C_{m\alpha} = -3.5223/rad$ $C_{n\beta} = 0.000643/rad$ and $C_{l\beta} = -0.070692/rad$ respectively for the NELD wing geometry.

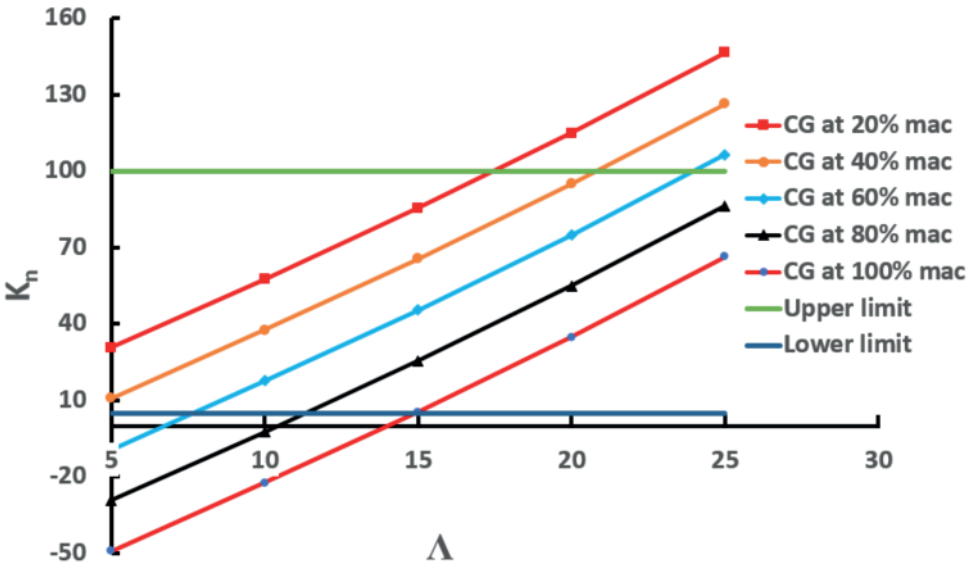

Figure 5.10: Static margin, K_n against sweep, Λ for different CG positions.

5.6 Conclusion

MH 45 airfoil was selected for the NELD wing design. After using Prandtl's 1933 theory, a twist distribution was generated and upwash was observed in the induced downwash plot at 70% of the normalized half span which corresponds with both Prandtl (1933) and Horten brothers (1984). This upwash creates induced thrust by tilting the aerodynamic force forward and produces a local negative induced drag (Bowers et al., 2016). A sweep of 15° was chosen to provide a static margin of 5.42% when CG was set at 100% MAC and 95.43% when the CG at 10% MAC. This gives a wide CG range and does not require users to add extra weight during flight test to ensure sufficient static margin. A stable wing planform was generated that was used for the computational studies discussed in the following chapter.

It should be highlighted that the sensitivity of the twist bounds and the removal of the span constraint should be investigated, which could yield further aerodynamic benefits as claimed by Prandtl.

6 CFD on new wing-body configuration (NELD)

6.1 Introduction

In the previous chapter, a novel wing design was developed using Prandtl's non-elliptic wing design methodology and the requirements of the AREND UAV. This Prandtl wing was designed with a varying non-linear twist and sweep and AVL was used (without the fuselage) to show that the wing had a non-elliptic lift distribution. In this chapter, the NELD wing is attached to the AREND fuselage keeping the wing location 346mm away from the nose and the CG point is also kept same as AREND for comparison purposes. The maximum Reynolds number of the flow over the root of the wing of chord $0.396m$ was found to be 5.2×10^5. The analysis was done for $-3^\circ \leq \alpha \leq 9^\circ$ and $0^\circ \leq \beta \leq 9^\circ$ in 3° intervals. The airflow was modeled as steady and incompressible and the wall $y^+ < 1$ criterion was satisfied for all simulations. The aim of this chapter is to carry out an investigation into the aerodynamics and flight mechanics benefits of the NELD configuration as claimed in Prandtl's (1933) paper.

6.2 Geometry

NELD uses the same F2-49 low drag body as fuselage as shown in Figure 6.1. The wings use MH45 airfoil with maximum thickness to chord ratio , t/c is 9.85% at 26.9% chord. The aspect ratio, $AR = 15.74$ is a high aspect ratio with wing area, $S_W = 1.15m^2$. The wing has a twist distribution which goes from 8° at the root, reaching the maximum of 8.5° at $2y/b = 0.16$, which then gradually decreases to -1.6° washout at the tips. It has a small sweep angle $\Lambda = 15^\circ$ with a truncated trailing edge for RANS convergence purposes. The main wing dimensions are provided in Table 6.1.

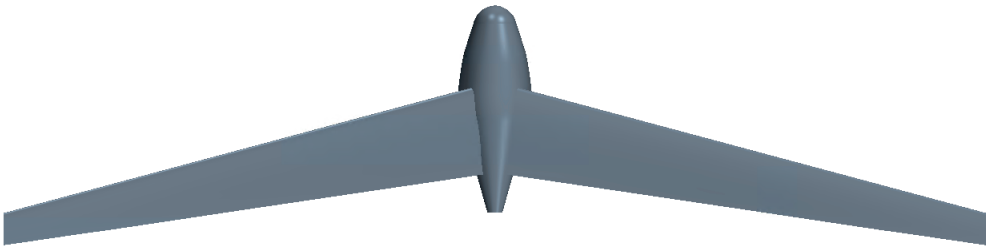

Figure 6.1: NELD configuration after cleaning the geometry.

Table 6.1: Defining the geometry of NELD.

Element	Length	Units
UAV length	898	mm
Wing-Span	4254	mm
Wing Root chord	396	mm
Wing Tip chord	140	mm
Sweep	15	°
MAC	288	mm

6.3 Domain sizing and boundary conditions

The computational domain and boundary conditions for NELD was kept the same as for AREND. A cylindrical domain is used and all the dimensions are measured from origin of the UAV. The inlet was fixed at around $16c$, the outlet at $82c$ and the farfield was set to $16c$ diameter. The domain was defined by a constant velocity inlet boundary condition, outlet was set to atmospheric

pressure boundary condition and the outer surface had a symmetric boundary condition. The boundaries at the surface of the UAV were specified as viscous wall (no-slip) boundary conditions. The boundaries at the symmetry plane were specified as an inviscid wall boundary condition.

6.4 Mesh independence study

All bodies were meshed and refined in the same way as in Chapter 4 using the same mesh functions and boundary layer growth layer. Due to the omission of booms and the inverted V-tail, the geometry has been simplified with just the fuselage and wing. The refinement zones include wing-fuselage interaction zone, nose of the fuselage and the wake region. A finer density region compared to the far field is created around the UAV. Figure 6.2 (a) shows the overall surface mesh with prism layers and their transition to polyhedral cells. The cells at the interface of the two meshes have similar aspect ratios, whereas the magnified view in Figures 6.2 (b) and (c) show the prism layers around the complex flow regions.

The leading edge and trailing edge of the wing as seen in Figure 6.2(d) have densely packed small cells to capture the complex flows. The local growth factor was 1.05 and maximum cell size was $3mm$. Another important feature that needs to be captured in the flow are the tip vortices. The maximum element size was fixed not to exceed $10mm$. The local growth ratio of 1.1 was used for the control domain beyond this region, which ensures that the tip vortex is captured properly. The wake refinement region extends from $5c$ top and bottom of the fuselage and $57c$ downstream. Using flat plate theory, the displacement thickness at the leading edge resolved using twenty five prism layers with advancing layer mesher, the boundary layer thickness $11mm$ and the size of the first cell is $0.02mm$. ($y^+ = 0.8$, $\Delta s = 0.015mm$ and $\delta = 0.005$). The wall $y^+ < 1$, criterion is the most preferred to capture the viscous sub-layers.

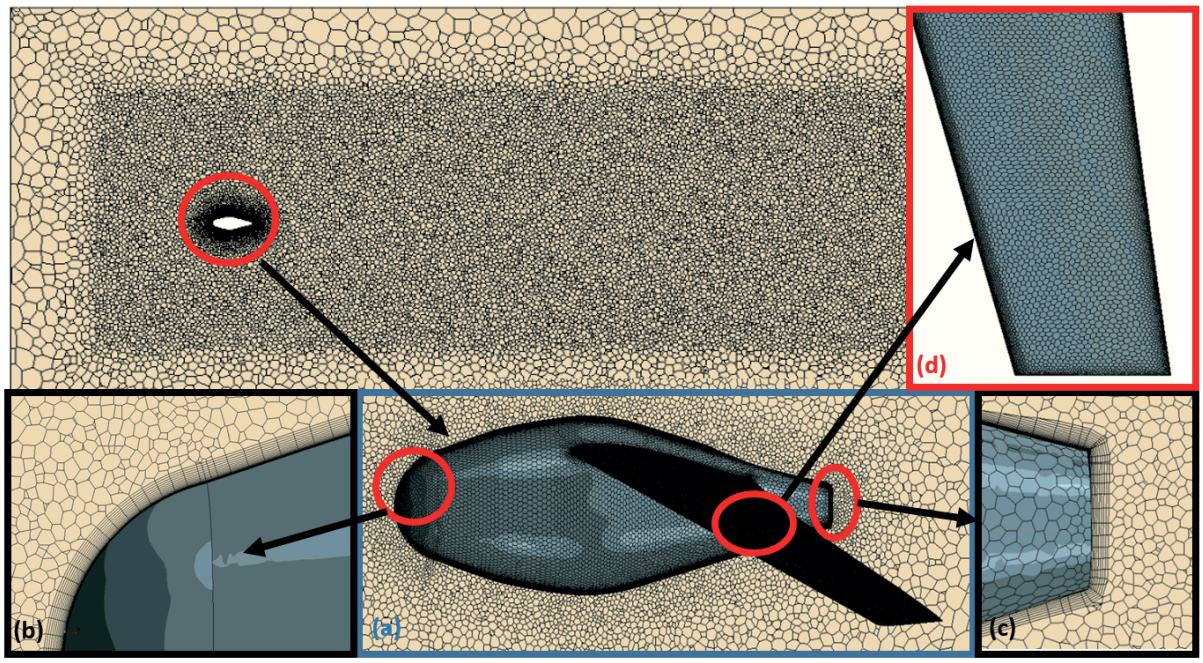

Figure 6.2: Mesh refinement on NELD (a) Surface mesh (b) prism layer around the nose (c) prism layers aft fuselage (d) surface mesh over the wing.

Grid convergence study is carried out to ensure that the solution obtained is independent of the grid density and is the optimum grid required for the simulation. The mesh independent study is carried out for three different meshes for varying density of elements as shown in Figure 6.3.

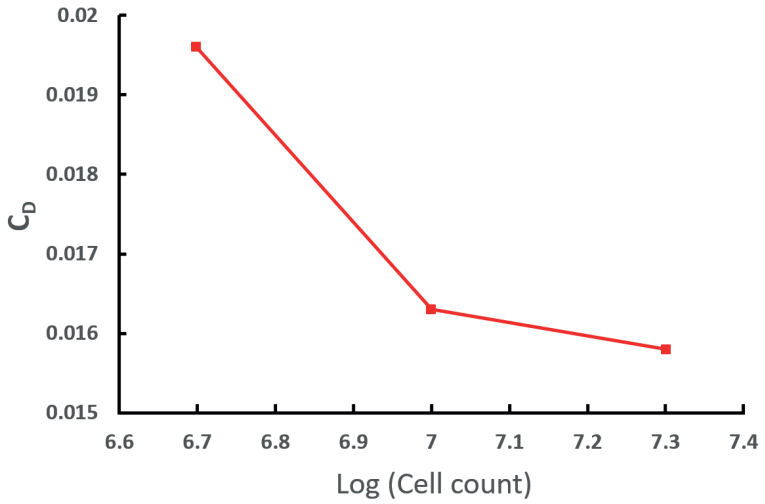

Figure 6.3: C_D against log of cell count for NELD at $\alpha = 0°$.

6.5 Flow over wing and fuselage

The flow over the NELD wing, shows presence of laminar separation bubbles. In Figure 6.4, it is seen that the bubble is thin and long at $\alpha = 0°$. As the α is increased, the separation bubble moves towards the leading edge and becomes shorter. Further increasing the α causes the bubble to move towards the leading edge until at $\alpha = 9°$, it results in leading edge separation (one of the causes for stall). This behaviour was expected due to transitional Reynolds number and the airfoil used here MH45 is a thin airfoil which is expected to undergo leading edge separation induced stall. Bubble bursting at the leading edge is an undesired feature of a wing because the stall is abrupt and can prejudice the take-off and landing operation.

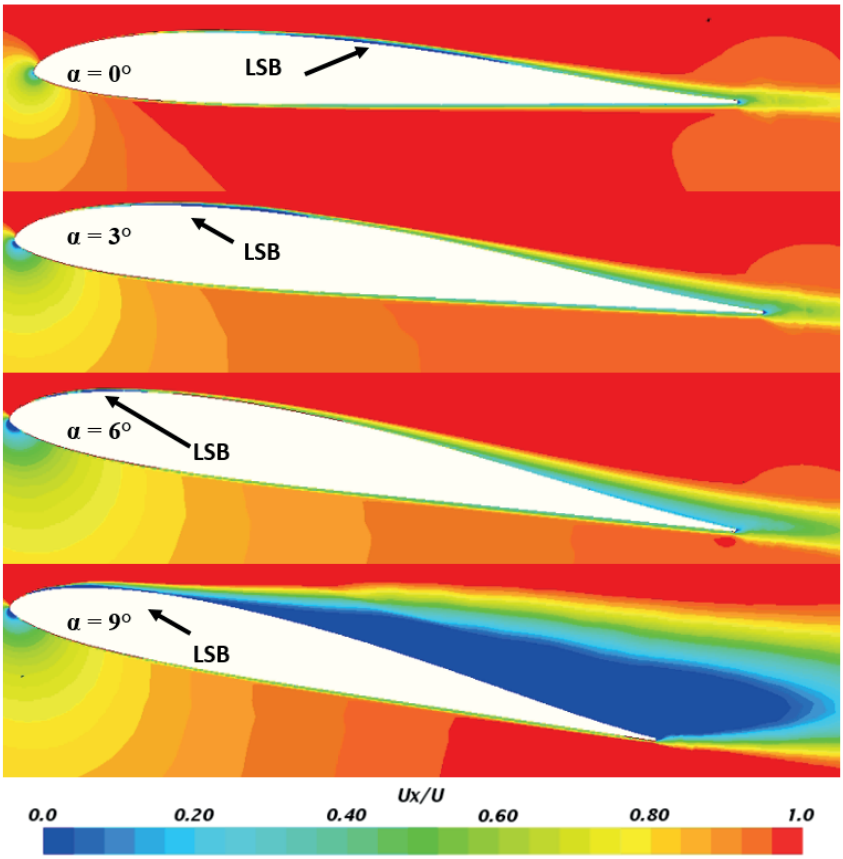

Figure 6.4: Laminar separation bubbles over the wing causing leading edge stall.

This leading edge stall is seen on the whole wing as shown in Figure 6.5. Stall occurs at $2y/b = 0.35$ where the twist is the highest and spreads towards the root and the tip of the wing. The inboard wing is at a high local α as compared to the outboard wing. The root wing stalls first before the tip therefore, the ailerons retain control authority in stall as compared to AREND where it is a tip stall.

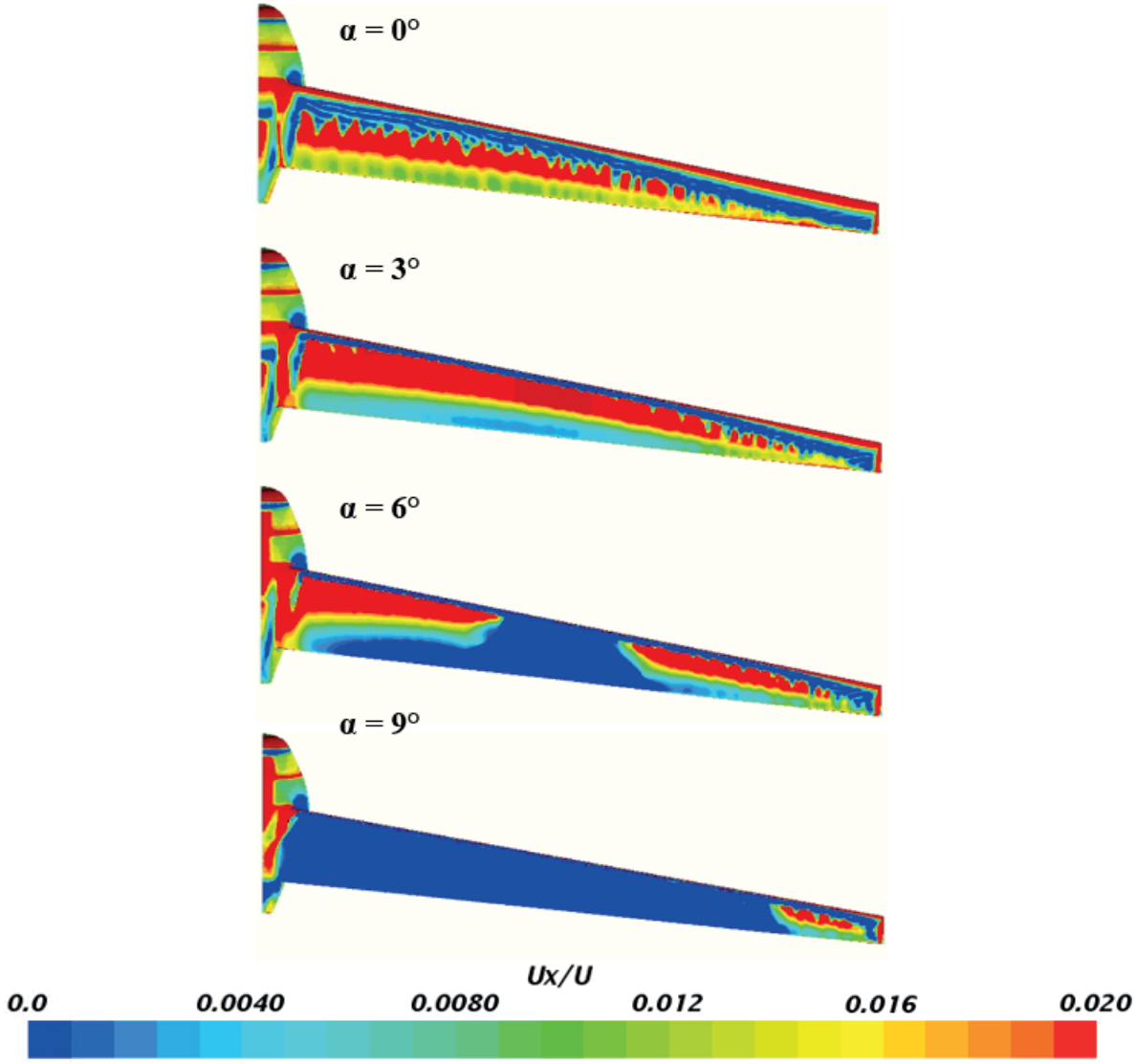

Figure 6.5: Flow over NELD over range of α showing stall patterns.

Figure 6.6 shows the wake of the fuselage which has two flow features similar to that seen for the AREND configuration. Features A and B highlight flow physics over different parts of the drone. Feature A, shows the vortices at the aft of fuselage, whereas feature B is the wake from the wing. It shows the separation effects happening forward due to wing separation and wing fuselage interaction. Figure 6.7 shows the visual side of the wake for different α. It also shows how the wake region widens but not as drastically as compared to the AREND UAV. This is because the wing is fully blended into the fuselage without gaps.

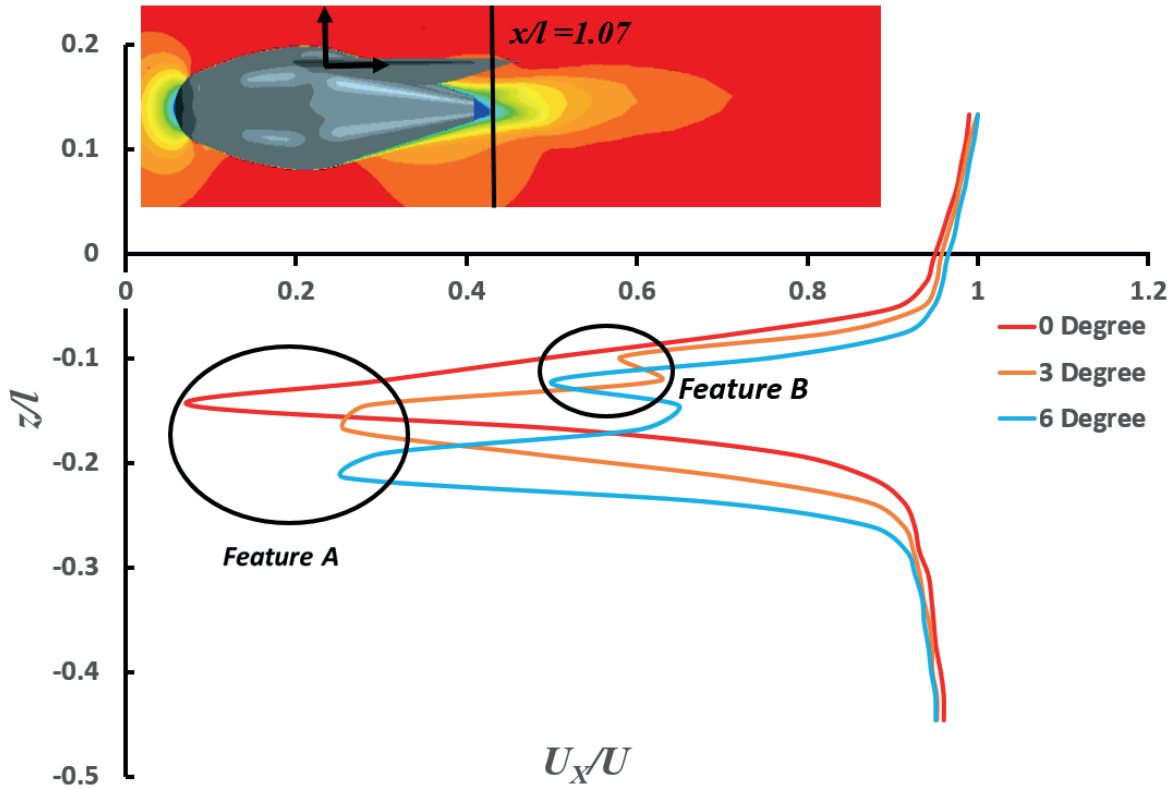

Figure 6.6: Normalized wake velocity profile of NELD for different α.

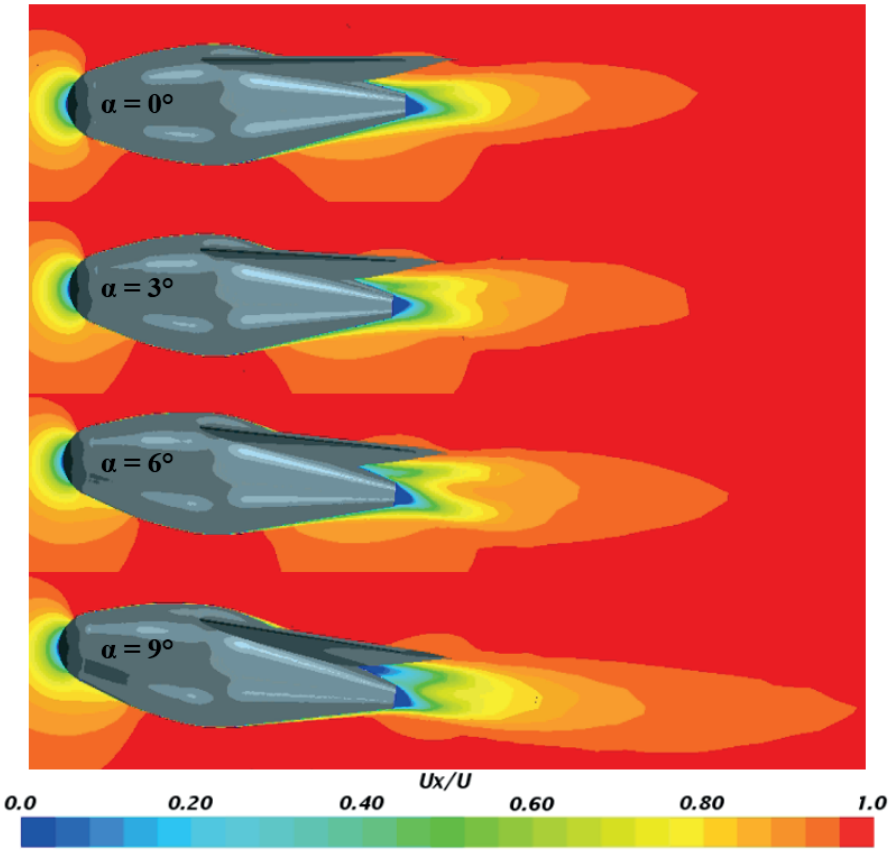

Figure 6.7: Normalized U_X/U velocity contour plot centerline of NELD fuselage visual representation of two wake features.

Figure 6.8 shows the vertical flow velocities through flow field visualisation along a slice taken over the fuselage centreline and spanwise variation of downwash (taken at $x/l = 1.19$ and $z/r = -1.44$) respectively. It is evident that the flow field aft of the fuselage is dominated by upwash at low α. With increasing α, this upwash region is gradually squeezed by regions of flow separation over the wing and the aft fuselage.

Figure 6.8 shows the expected increase in spanwise downwash velocities. It is interesting to see that there is upwash at $2y/b = 0.85$ for $\alpha = 0°$ as Prandtl predicted. It shows the presence of induced thrust at the wing tips and the spanwise induced downwash (from AVL simulation) yields the curve shown in Figure 5.7, which predicts the upwash occurring at $2y/b = 0.7$ which correlates with both Prandtl (1933) and Horten brothers (1984). It follows the same form described by Bowers et al. (2016) : a strong downwash at the root that tapers outboard until upwash is created at the outer wing. This demonstrates the formation of induced thrust as Horten brothers (1984) suggested, where the downwash at the core of the vortices transform into upwash at the wingtips. This only occurs upto the point where the aircraft begins to stall ($\alpha = 6°$).

It should also be noted that in Figure 6.8 we can also see the spanwise positions where the wing stalls locally (at $\alpha = 6°$). Here, the local stall positions are infact shifted towards the right because of the line of measurement defined in the postprocessing of the CFD results. It is thus possible that the inboard vortex occurring at $2y/b = 0.85$ for $\alpha = 0°$, has indeed shifted inwards and as stall occurs around $2y/b = 0.35$.

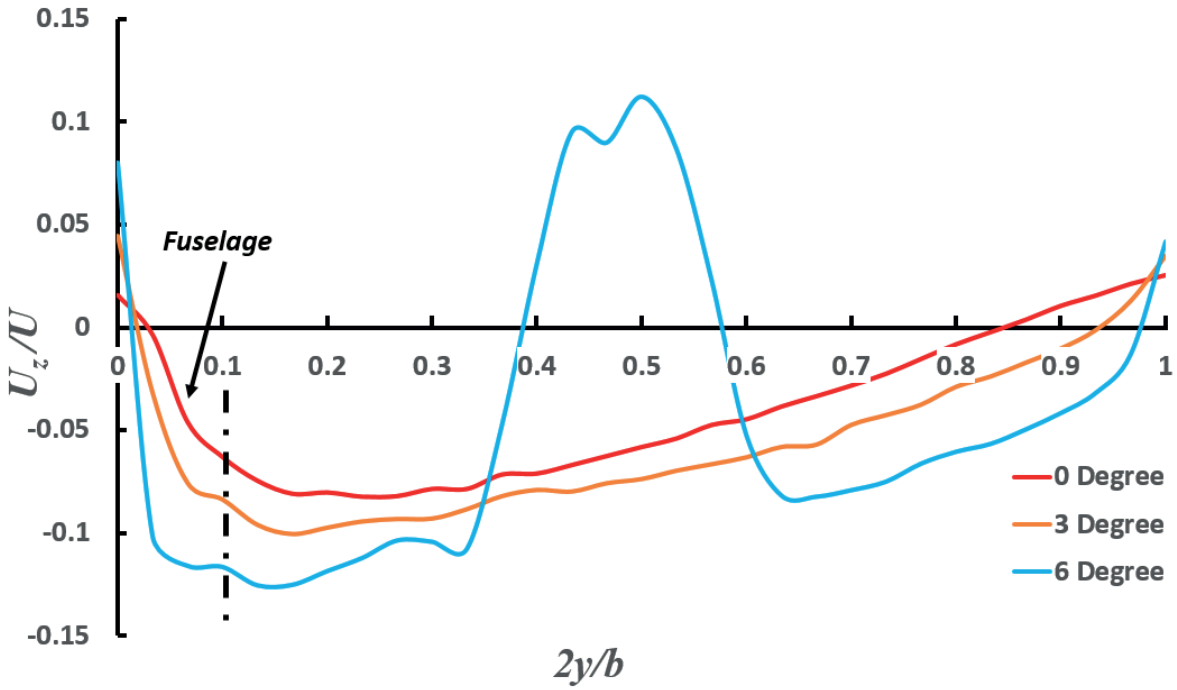

Figure 6.8: Downwash profile of the NELD wing plotted for different α.

6.6 Comparison with AVL

In order to verify the data from CFD it was compared with results from the AVL which, given the theoretical basis of AVL should provide similar results to the CFD data for low α.

6.6.1 Lift coefficient curve

The C_L is plotted against α for CFD and AVL data respectively in Figure 6.9. The difference is 6.9% for small angles of attack (from$-3°$ to $3°$). The NELD configuration stalls at $6°$ and therefore, AVL is not able to provide accurate predictions as it does not model viscous effects. The results from AVL are only valid for small angles and inviscid flows. Moreover, AVL does not take the effects of airfoil thickness into account.

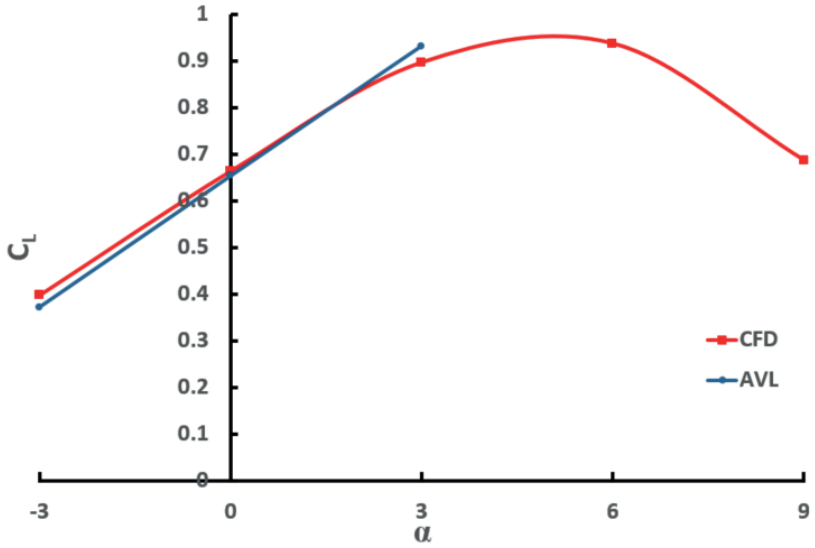

Figure 6.9: Comparison between AVL and CFD results of C_L versus α at Re $= 5.2 \times 10^5$.

6.6.2 Pitching moment curve

Another parameter which can be compared with the AVL is the C_m and its variation with respect to α. From Figure 6.10, it is seen that the maximum difference between the AVL and CFD results is 7.9% from $-3°$ to $3°$. At $6°$, the difference becomes 26.6% which clearly shows that the AVL data is not valid anymore.

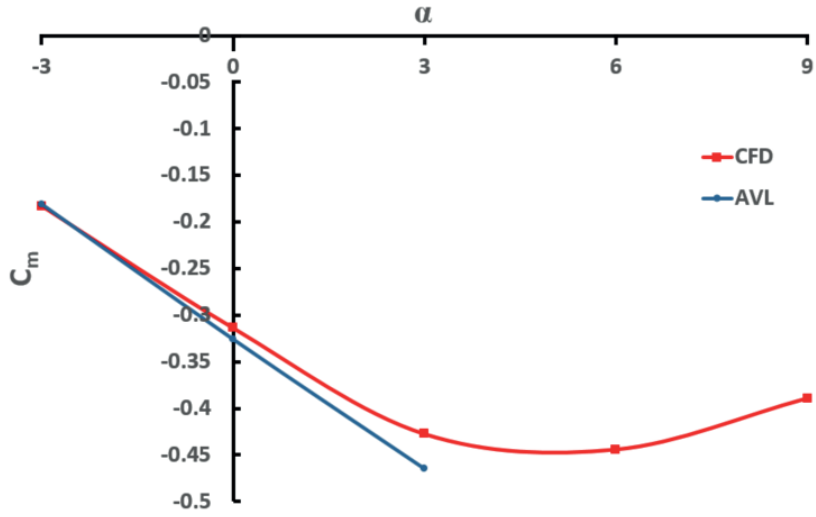

Figure 6.10: Comparison between AVL and CFD results of C_m versus α at Re $= 5.2 \times 10^5$.

The results were compared with the AVL output for small α and β and the difference was under 10%. This comparative analysis therefore, verifies CFD results for small α.

6.7 Results

6.7.1 Aerodynamics

In Figure 6.11, the C_L is plotted against α. It is noted that the $C_{L,max}$ is 0.94 at $\alpha = 5°$ and $C_{L\alpha} = 4.751/rad$. For small β the $C_{L\alpha}$ does not change but it is seen that for $\beta = 9°$, $C_{L,max}$ reduces to 0.88 which translates to a 6.38% reduction in lift coefficient. Once the forces are resolved into three components, the lift component is decreased where as the drag and side force components increase. Stall in this case is caused due to the formation of a laminar separation bubble which reattaches itself at small α. However, as α increases the laminar separation bubble moves forward and the bubble contracts, reattachment may not occour for large α and at the critical angle of $\alpha = 6°$ the NELD configuration stalls. Stall occurs at the root and moves towards the tip due to the non-linear twist distribution. The inboard wing is at a higher α as compared to the outer wing. It is seen that NELD lift coefficient is insensitive to β changes except after stall. The wing upper and lower limitations for twist distribution should be carefully chosen since having large differences between the bounds might lead to a profile with early stall characteristics. Preference should be given to airfoils with a high C_l and higher stall angles, whereas thin airfoils should be avoided owing to leading edge stall as shown in Figure 6.5.

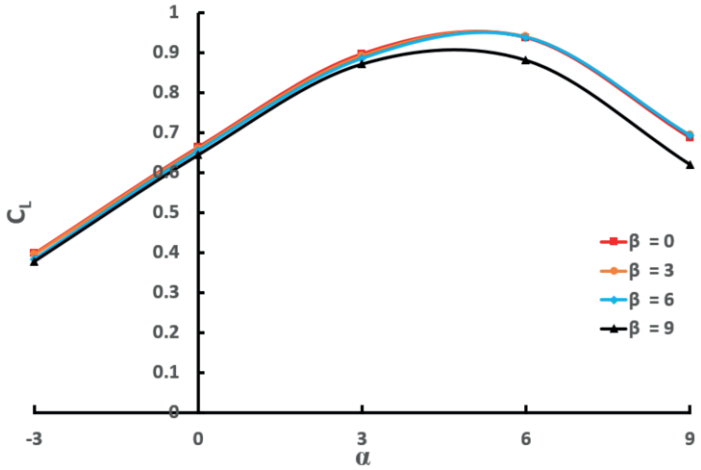

Figure 6.11: C_L versus α with different β for NELD at Re $= 5.2 \times 10^5$.

In Figure 6.12, the C_D increases with α. As the β increases the C_D also increases, especially after stall occurs. The drag bucket was found to be insensitive to small changes in β.

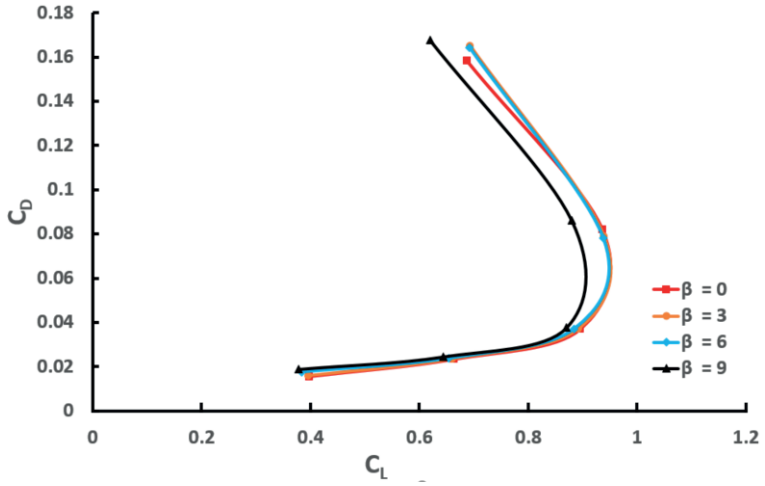

Figure 6.12: C_D versus α with different β for NELD at Re $= 5.2 \times 10^5$.

6.7.2 Stability

The C_m does not change much at small β as shown in Figure 6.13. However, a significant change in the slope can be seen at $\beta = 9°$ indicating that the configuration becomes less stable albeit remaining in a flyable condition. The major difference is seen in post stall recovery where for small β angles the aircraft recovers quickly but there is slower recovery for $6° \leq \beta \leq 9°$. Due to the early stall at $\alpha = 6°$ and the high levels of separation and instability in the flow, more accurate interpretations could be produced by time-dependent analysis. However, these were beyond the scope of this study. This also shows that longitudinal static stability can be achieved even if C_{m0} is not close to zero because adding a little sweep can aid in stabilizing $C_{m\alpha}$.

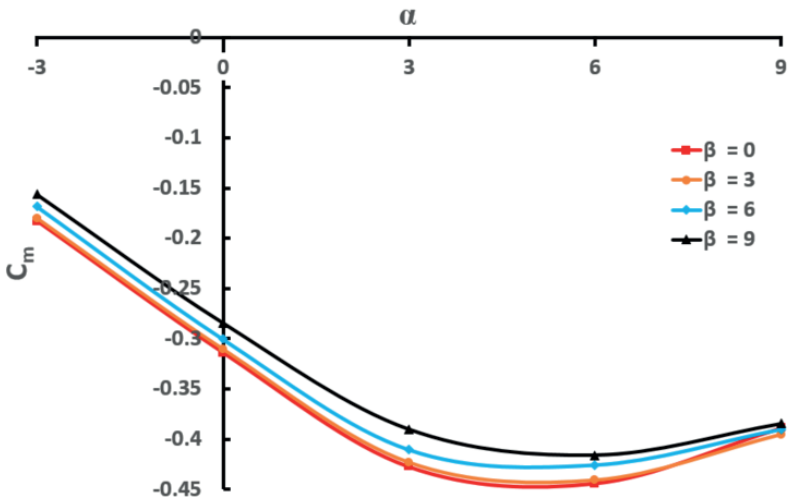

Figure 6.13: C_m versus α with different β for NELD at Re $= 5.2 \times 10^5$.

In Figure 6.14, directional stability governed by the $C_{n\beta}$ can be seen to decrease with β. It is seen that the UAV becomes unstable at $\beta = 6°$. The slope of this derivative decreases from positive to negative as the β is gradually increased eventually becoming unstable. This happens due to the lack of a tailboom to generate a stabilising yawing moment. The slight stability observable in Figure 6.14 is due to fuselage effects. Winglets at the tip of a NELD wing could work as the moment arm will depend of the sweep angle. Positive sweep angle helps lateral and directional stability as both are coupled.

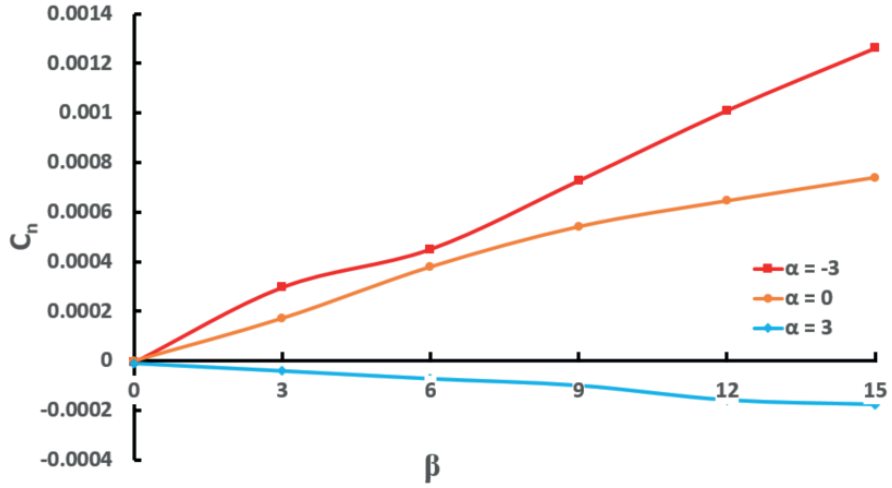

Figure 6.14: C_n versus β with different α for NELD at Re $= 5.2 \times 10^5$.

Coordinated flight was one of the benefits claimed by Prandtl (1933). Figure 6.15 plots the lift distribution for $\alpha = 0°$ with $\beta = 0°$ and $\beta = 3°$. It is seen that the lift distribution is symmetric when at $\beta = 0°$ as expected but as soon as the vehicle turns port (left; positive sideslip), the NELD configuration produces more lift on the starboard wing to produce a roll in the same direction. The right side wing generates greater lift as compared to the left side, and so the aircraft rolls into a coordinated turn.

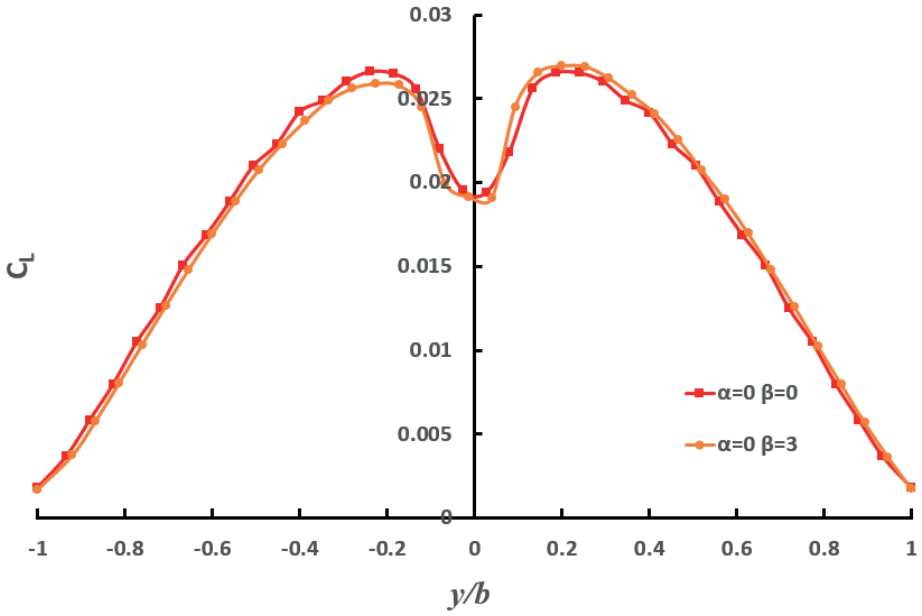

Figure 6.15: C_L distribution over the wing span for different β for NELD at Re $= 5.2 \times 10^5$.

The $C_{l\beta}$ decreases as the β is increased making it more stable as shown in Figure 6.16. This shows that if the aircraft is subjected to a β, the aircraft will roll in the same direction due to proverse yaw. This type of behaviour helps avoid adverse yaw and assists in coordinated turn.

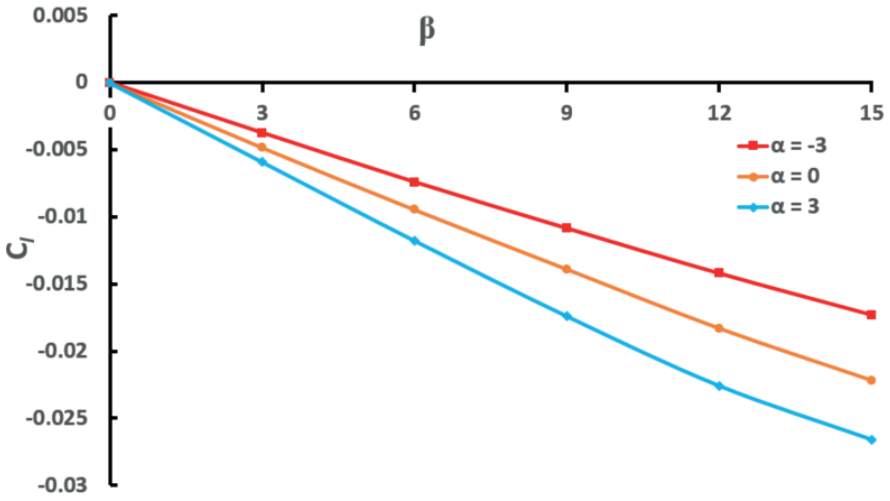

Figure 6.16: C_l versus β with different α for NELD at Re $= 5.2 \times 10^5$.

The side force with respect to β at different α is plotted in Figure 6.17 to indicate how much the aircraft may drift in side wind conditions. It is seen that as angle of attack increases, $C_{Y,\beta}$ decreases which means that the UAV displacement is higher for the same side wind conditions.

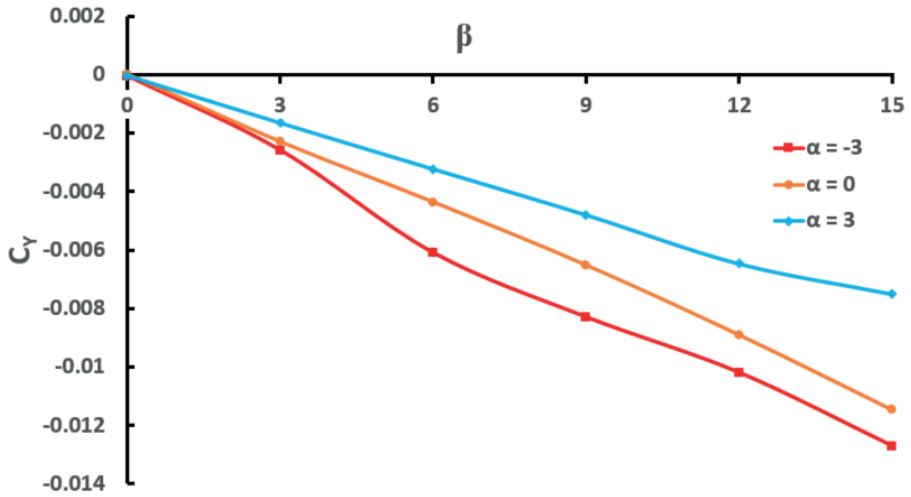

Figure 6.17: C_Y versus β with different α for NELD at Re $= 5.2 \times 10^5$.

6.8 Conclusion

The computational study of NELD wing quantified the aerodynamic and flight dynamic parameters for different α and β. The results were compared with the AVL output for small α and β and the difference was under 10%. It was found that the NELD configuration undergoes leading edge separation which leads to stall due to the thin MH45 airfoil. Stall begins inboard at $2y/b = 0.35$ and then spreads towards root and tip. Upwash was seen to occur at $2y/b = 0.85$ indicating the presence of induced thrust as predicted and shown by Prandtl (1933) and the Horten Brothers (1984) in their studies respectively. The change in lift distribution over the wing due to sideslip also shows that the NELD configuration can indeed perform a coordinated turn.

The wing upper and lower limitations for twist distribution should be carefully chosen since having large differences between the bounds might lead to a profile with early stall characteristics. Preference should be given to airfoils with a high c_l and higher stall angles, whereas thin airfoils should be avoided owing to leading edge stall. Longitudinal static stability can be achieved even if C_{m0} is not close to zero because adding a little sweep can aid in stabilizing $C_{m\alpha}$.

7 Comparison of AREND and NELD configuration

7.1 Introduction

This chapter compares performance metrics of the AREND and NELD configurations. It provides insight into the differences between the two configurations. However, note that the results are limited to cruise condition, and are divided into aerodynamics, static stability and performance.

7.2 Aerodynamics

Here comparison is made through the lift curve slopes (as a function α) and the drag polar. Drag is decomposed into its various components and finally, aerodynamic efficiency is compared. The lift distribution over the span for AREND and NELD wing is compared.

7.2.1 Lift coefficient curve

Figure 7.1 shows the relationship between C_L and α. It is worth noting that the $C_{L,max}$ for the NELD configuration is 0.94 but the $C_{L,max}$ for AREND is 1.38. This is because the NELD configuration stalls at 5°, whereas the AREND stalls at 12°. The required $C_{L,Cruise} \geq 0.66$ (20kg weight at 400m ASL), which implies that the NELD configuration can fly at $\alpha = 0°$ and therefore, can be mounted at 0° wing setting angle (with respect to the fuselage). The AREND configuration generates the required lift at 2.5° and is currently mounted at 0.5° with respect to fuselage and cruises at $\alpha = 2°$. The linear region covers a total of 6°angle of attack for the NELD wing whereas for AREND, this is 8° when the baseline C_L is kept constant. NELD undergoes leading edge stall whereas AREND undergoes trailing edge stall coupled with tip stall. For the same change in angle of attack the lift curve slope of NELD $4.751/rad$ which is less than AREND's $5.359/rad$. It is seen that the NELD has a drastic decrease in lift when compared to AREND. It is also seen that if the wing setting angle is set to $-3°$ for NELD similar lift values are obtained as that of AREND at 0°.

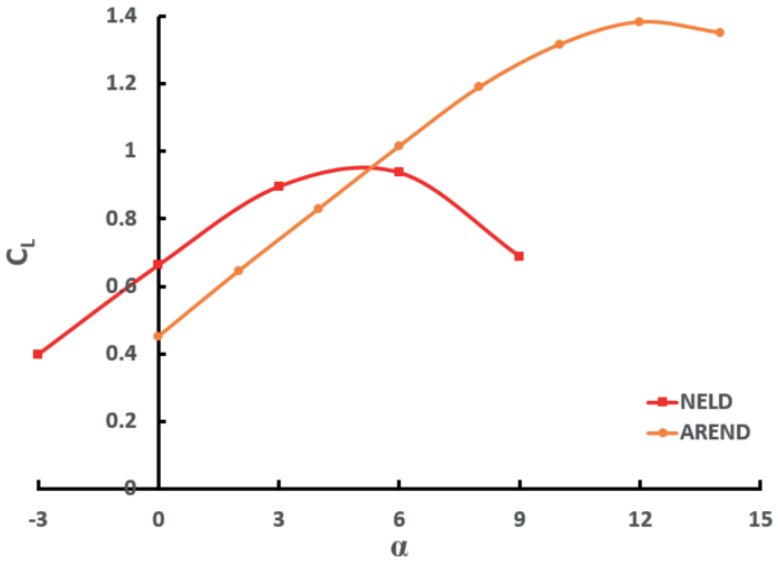

Figure 7.1: $C_L - \alpha$ curve comparing the AREND and NELD configuration.

7.2.2 The drag polar

The drag polar in Figure 7.2 shows that the total drag in cruise for the NELD configuration is 6.74% lower than that of AREND. This decrease is due to reduction in pressure drag and skin friction drag before separation. It is seen that at 3° the drag coefficients for AREND and NELD

are equal. After that, the C_D for the NELD configuration increases rapidly as flow separation leads to stall. The laminar bucket for NELD is very small when compared to AREND and this is due to the early stall of the NELD wing which is caused by the twist distribution of the wing defined using Prandtl's theory.

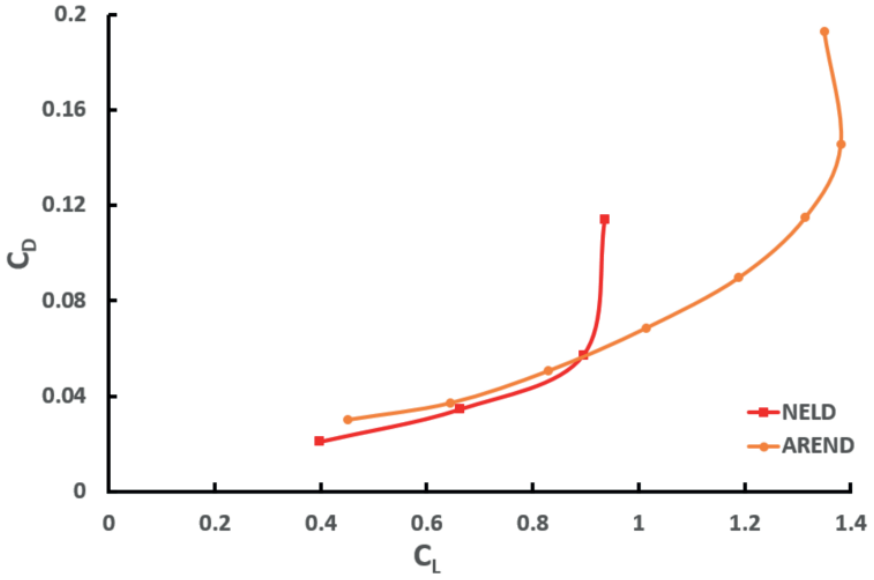

Figure 7.2: Drag polar for AREND and NELD configuration.

7.2.3 Drag breakdown

The drag polar shows decrease in total drag for the NELD configuration. Hence, to investigate the decrease in drag at cruise, the drag components were plotted against lift. The C_{Di} in Figure 7.3 for the NELD configuration is 1.85% higher as compared to AREND for cruise condition. This is due to the fact that the span for AREND and the span of NELD is kept the same, hence the advantage of reduction in induced drag is not seen which agrees with Prandtl's theory. AVL is used to get C_{Di} and its deemed acceptable since its an inviscid code, and CFD is used separately for pressure and friction terms because it includes viscous effects.

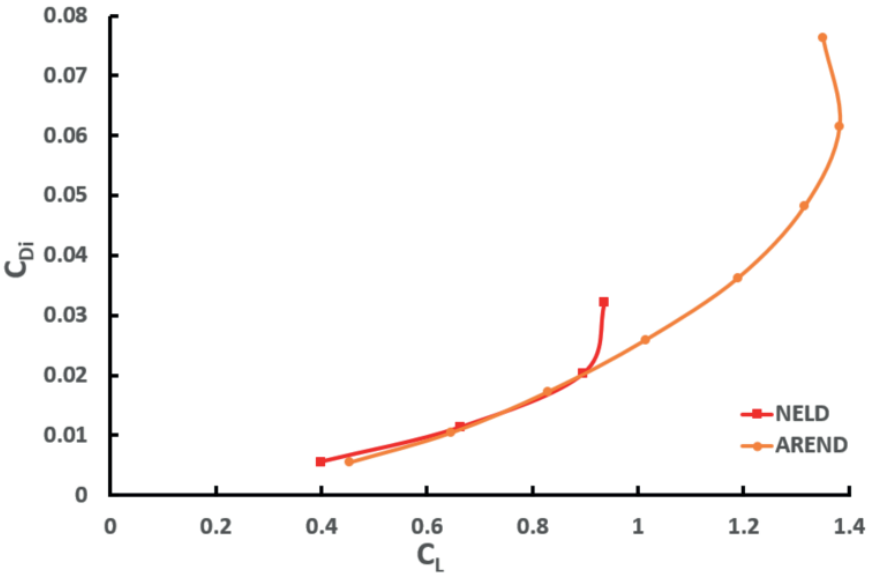

Figure 7.3: Induced drag polar for AREND and NELD configuration.

The pressure drag for NELD in cruise decreases by 16% as compared to the AREND as seen in Figure 7.4. The pressure drag coefficient remains less until 3° but due to flow separation there is a sharp increase in pressure drag after this α.

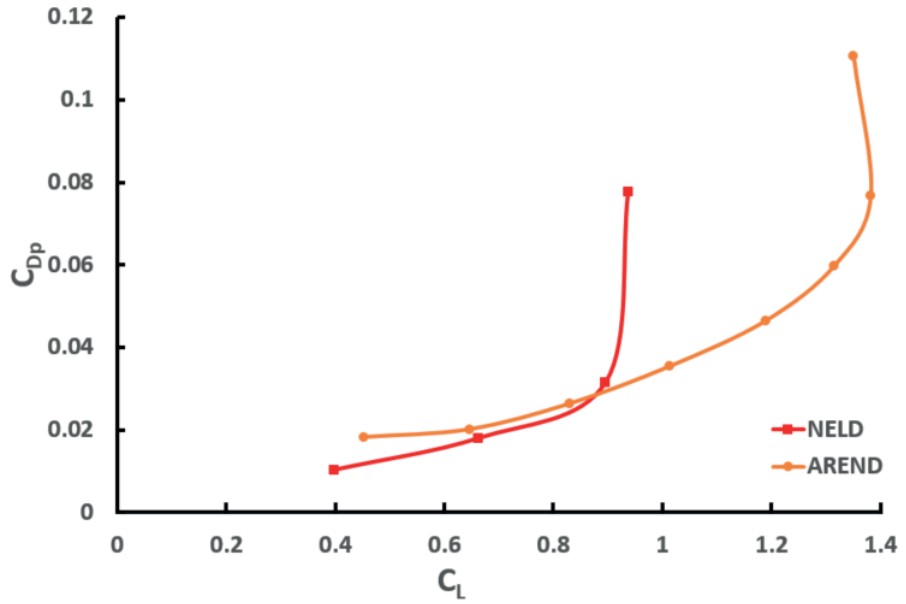

Figure 7.4: Pressure drag polar for AREND and NELD configuration.

In Figure 7.5, it is seen that skin friction drag coefficient decreases by 20% at cruise for the NELD configuration. The skin friction drag coefficient for NELD is always lower than that for AREND because of the reduction in the wetted surface area with the booms and empennage removed. After separation it is seen that the skin friction drag for AREND and NELD configurations decrease drastically.

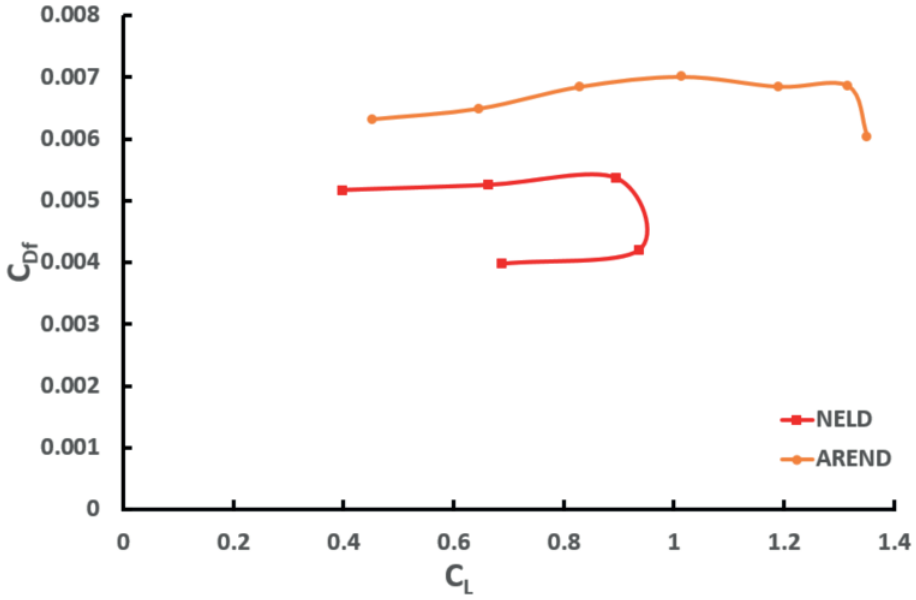

Figure 7.5: Skin friction drag polar for AREND and NELD configuration.

Now, comparing the overall C_D for NELD it was found that total drag is dominated by pressure drag that accounts for 52% and then induced drag at 33%, followed by the 15% for skin friction. However, for AREND it was 54% pressure drag, 28% induced drag and 18% skin friction drag. Therefore, it is concluded that the overall reduction in drag is because of the removal of booms and empennage.

7.2.4 Efficiency

Figure 7.6 shows that efficiency at cruise point increases by 9.87% for the NELD configuration, but this decreases as the NELD configuration reaches the stall angle. It is also seen that the efficiency at $C_{L,max}$ is the same for both AREND and NELD ($C_L/C_D = 10$). As discussed above, the stall for NELD is drastic as compared to AREND due to drastic decrease in C_L/C_D ratio with respect to α. This shows that wings designed to have non-elliptic lift distributions are highly optimised for cruise point.

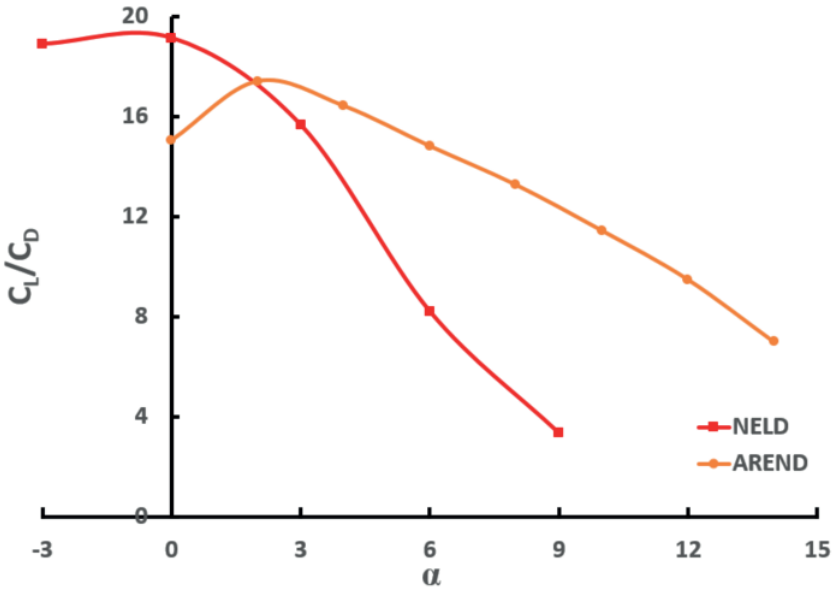

Figure 7.6: Comparison of aerodynamic efficiency for AREND and NELD configuration.

7.2.5 Lift distribution

Figure 7.7 presents lift distribution over the wing for the same lift coefficient required for cruise. It is seen that majority of the lift is generated by the inboard wing for NELD and it steeply declines towards the tip which helps in reducing the strength of the tip vortices. Comparing the lift distributions of both configurations it is seen that NELD generated much larger lift coefficients inboard wing and at the half span point both configurations generate the same amount of lift. However, the AREND has significantly higher lift coefficients in the outboard wing regions. This lift coefficient at the tip for AREND is nearly three times as for the NELD meaning that there is a higher pressure gradient at the top and the bottom of the wing which results in stronger tip vortices. NELD's reduced outboard wing loading shows that structural weight can be reduced due to reductions in wing root bending moments. It is also evident that NELD produces the same lift at a smaller angle of attack as compared to AREND due to the twist distribution.

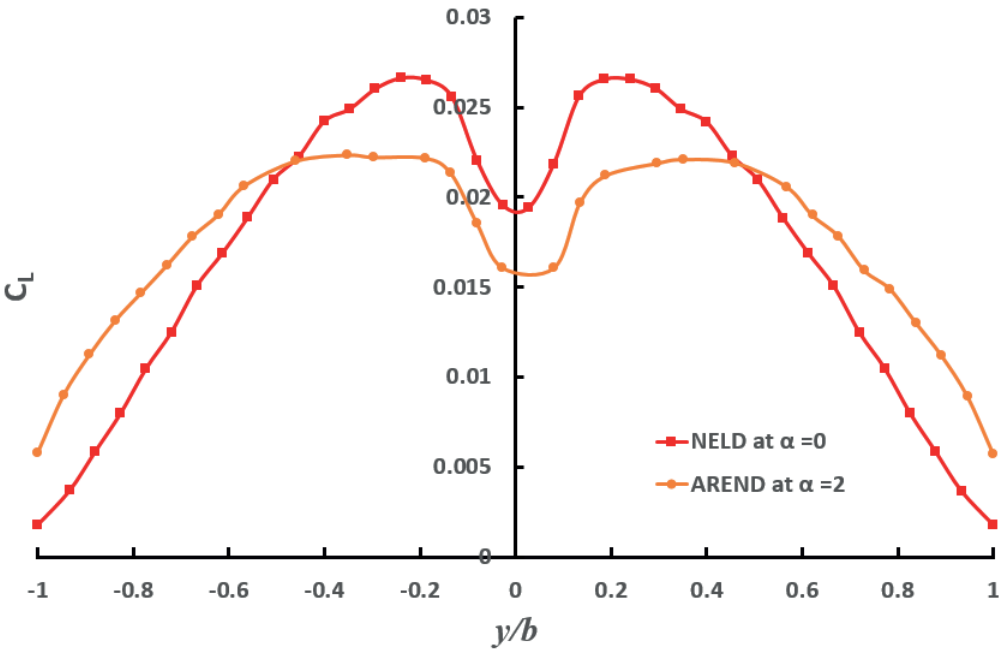

Figure 7.7: Spanwise C_L distribution for AREND and NELD at cruise.

7.3 Static stability

This section is divided into two subsections: longitudinal and lateral static stability. Lateral static stability is divided further into yaw, roll and side force derivatives.

7.3.1 Longitudinal static stability

Pitch stability defined by $C_{m\alpha}$ is computed and compared for the AREND and NELD configurations. Considering the results presented in Figure 7.8, NELD has a $C_{m\alpha} = -2.54/rad$ before stall. It is seen that the pitch stability has increased by 128% for the NELD design but it is also noted that the behaviour of AREND remains stable even after stall. Even though C_{m0} is negative for NELD, it should be noted that the CG can be placed over a much bigger range. Furthermore, given that the C_{m0} is significantly negative, the nose down load is not needed and the NELD configuration can be trimmed when the CG is placed towards the wing trailing edge. Nickel and Wohlfahrt (1994) recommend using fairly large static margins to ensure acceptable handling qualities. However, this leads to trim drag penalty and a sub-optimal lift distribution leading to higher induced drag. A swept back wing combined with relatively large twist gives a longer moment arm and more pitch damping. The NELD configuration is highly stable in the longitudinal axis therefore, the fuselage mounting point can be shifted as long as the CG lies in the stable zone.

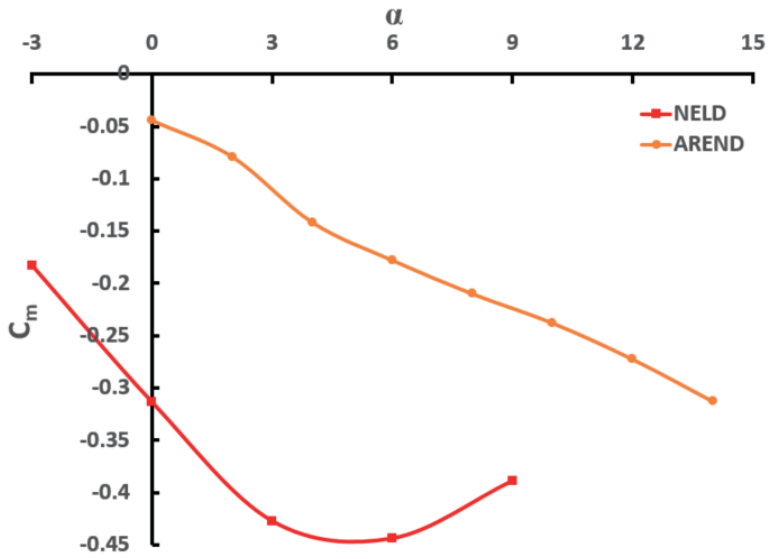

Figure 7.8: $C_m - \alpha$ for AREND and NELD configuration.

7.3.2 Lateral Stability

The yaw stability derivative should be positive to ensure directional stability. Phillips (2004) recommends that for a typical aircraft configuration, $0.06/rad \leq C_{n\beta} \leq 0.15/rad$ and an ultimate lower limit of $0.03/rad$ is suggested, with no actual upper limit. The yaw stability derivative for AREND is $C_{n\beta} = 0.063/rad$ and NELD is $C_{n\beta} = 0.002/rad$ as seen in Figure 7.9. The latter is very low as compared to the recommended value so a vertical stabilizer with appropriate moment arm is required for NELD. Winglet reduces induced drag without increasing span or adding an unacceptable amount of profile and interference drag at low lift coefficients. It also helps improve handling qualities.

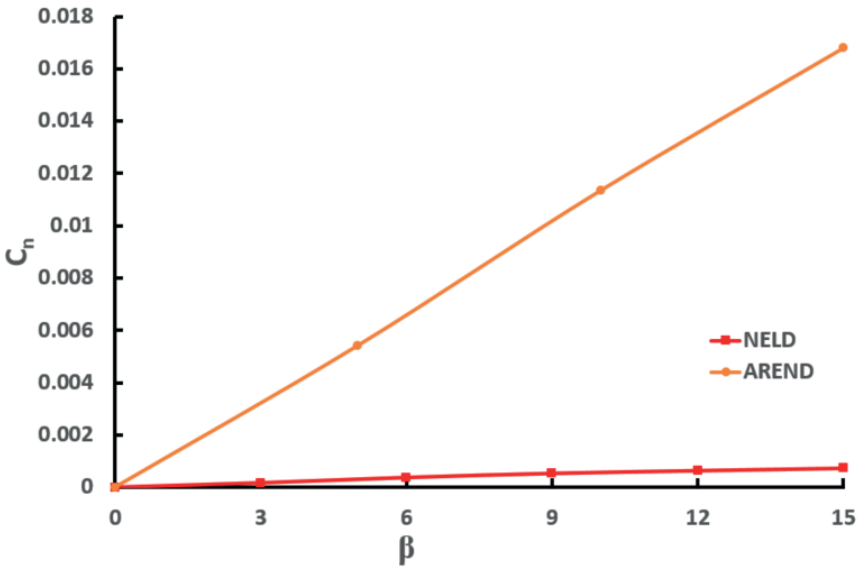

Figure 7.9: $C_n - \beta$ curves for AREND and NELD configuration.

Figure 7.10 shows the roll stability derivative $C_{l\beta}$ which should be negative for a stable configuration. Phillips (2004) recommends a value $-0.1/rad \leq C_{l\beta} \leq 0.0/rad$, but these are very rough guidelines for starting values and should only be used for that purpose. The slope for the AREND is $C_{l\beta} = -0.0344/rad$ which is less than the NELD configuration $C_{l\beta} = -0.0859/rad$.

The roll stability is better in NELD configuration is because of the proverse yaw component of NELD which ensures coordinated turns.

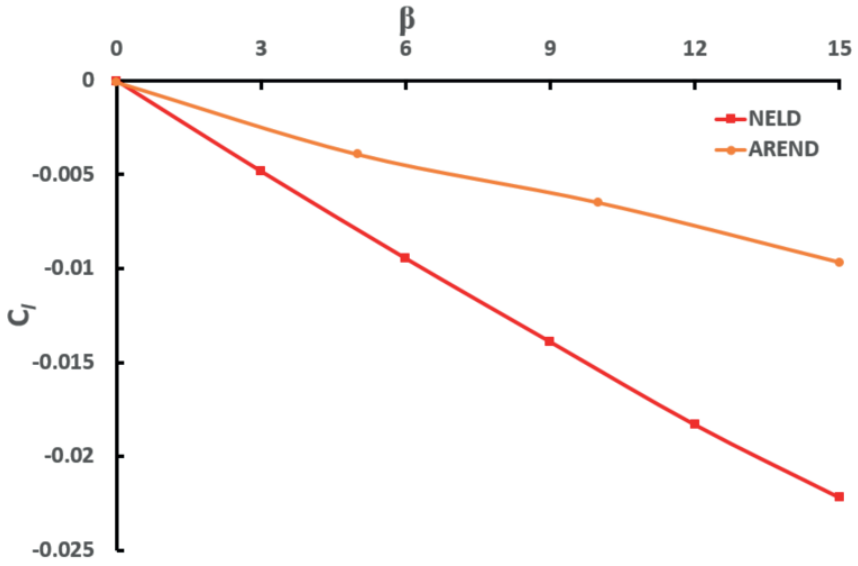

Figure 7.10: $C_l - \beta$ for AREND and NELD configuration.

Figure 7.11 compares the side force derivative generated by the configurations. NELD has a low $C_{Y\beta}$ which makes it easier to control in a side wind as it will not drift much as compared to AREND.

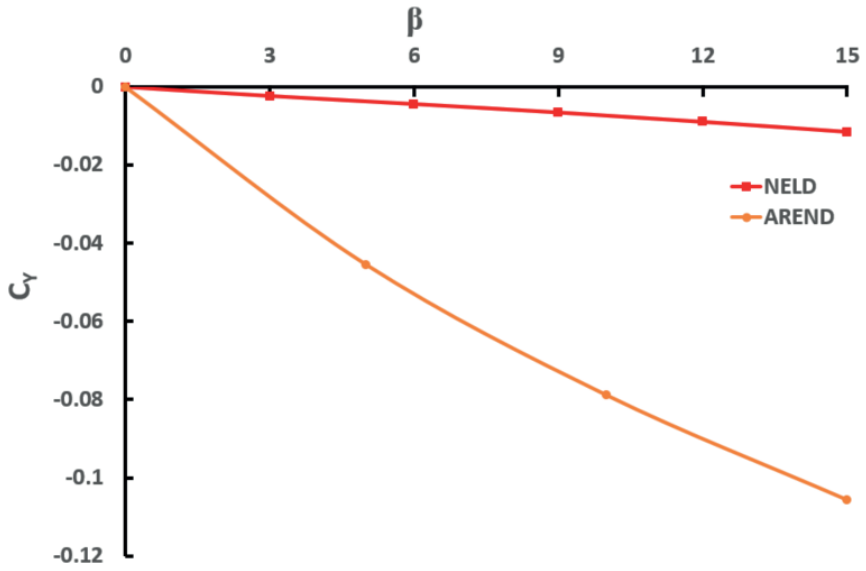

Figure 7.11: $C_Y - \beta$ for AREND and NELD configuration.

7.4 Flight performance

In the previous sections, AREND and NELD configurations were compared in terms of aerodynamic and flight dynamic characteristics. This sections compares the performance of the two configurations in terms of range, stall speed and unpowered glide angle. Power required and turning radius are also considered.

7.4.1 Range estimates

For a steady level flight, the range can be defined by the Breguet Range Equation as follows:

$$R = \frac{\eta}{c}\frac{C_L}{C_D} ln \frac{W_0}{W_1} \tag{7.1}$$

where R is range in m and c is specific fuel consumption in $N/(J/s)(s)$. Assuming that the specific fuel consumption is same for both configurations, the percentage change in range of the NELD configuration to the AREND can be calculated as follows:

$$R_{NELD} = \frac{\eta}{c}\frac{C_{L,NELD}}{C_{D,NELD}} ln \frac{W_{0,NELD}}{W_{1,NELD}} \tag{7.2}$$

$$R_{AREND} = \frac{\eta}{c}\frac{C_{L,AREND}}{C_{D,AREND}} ln \frac{W_{0,AREND}}{W_{1,AREND}} \tag{7.3}$$

$$\frac{R_{NELD}}{R_{AREND}} = \left(\frac{\left(\frac{C_{L,NELD}}{C_{D,NELD}} ln \frac{W_{0,NELD}}{W_{1,NELD}}\right)}{\left(\frac{C_{L,AREND}}{C_{D,AREND}} ln \frac{W_{0,AREND}}{W_{1,AREND}}\right)} \right) \tag{7.4}$$

Assuming that the weight ratios are the same, hence only considering aerodynamic benefit, we get

$$\frac{R_{NELD}}{R_{AREND}} = \left(\frac{\left(\frac{C_{L,NELD}}{C_{D,NELD}}\right)}{\left(\frac{C_{L,AREND}}{C_{D,AREND}}\right)} \right) \tag{7.5}$$

$$\frac{R_{NELD}}{R_{AREND}} = \left(\frac{(19.16)}{(17.45)} \right) \tag{7.6}$$

$$\frac{R_{NELD}}{R_{AREND}} = 1.10 \tag{7.7}$$

Breguet range equation is not as applicable to electric powered UAVs as the equation takes into account change of weight due to fuel consumption over time . It can be concluded that based purely on aerodynamic parameters the range of the NELD aircraft is increased by 10%. However, given that the NELD configuration does not require a tailplane, a range benefit of upto 22% can be obtained using Equation 7.2.

7.4.2 Stall speed

Stall speed is defined as the minimum speed required to maintain lift in a steady level flight. Assuming that the empannage, including servos, carbon rods, and connection points, was at least 10% of the overall weight of AREND. Therefore, it is taken as $1.8kg$.

$$V_{stall} = \sqrt{\frac{2mg}{\rho S C_{L,max}}} \tag{7.8}$$

$$\frac{V_{stall,NELD}}{V_{stall,AREND}} = \sqrt{\frac{\frac{m_{NELD}}{C_{L,max\ \ NELD}}}{\frac{m_{AREND}}{C_{L,max\ \ AREND}}}} \tag{7.9}$$

Assuming the mass of empennage was 1.8kg, and the NELD configuration does not have an empennage therefore, there is a decrease in total weight.

$$\frac{V_{stall,NELD}}{V_{stall,AREND}} = \sqrt{\frac{\frac{16.2}{0.94}}{\frac{18}{1.38}}} \tag{7.10}$$

$$\frac{V_{stall,NELD}}{V_{stall,AREND}} = 1.15 \tag{7.11}$$

Equation 7.11 compares the stall speed of both configurations and it is seen that the stall speed of NELD increases by 15%. This happens due to a lower maximum lift coefficient. It concludes that the $C_{L,max-NELD}$ plays a very important role in performance regarding stall speed. The lower the stall speed the better because it is the slowest speed at which the aircraft can fly in a steady level flight or trimmed flight.

7.4.3 Glide flight

This aspect was considered in case the UAV runs out of power. For unpowered glide flight equation represents glide angle which is a function of lift to drag ratio. The higher the lift to drag ratio, the shallower the angle which inturn implies a higher range in unpowered flight. Inevitably, the aerodynamic performance translates to the glide flight performance as follows:

$$tan\theta = \frac{1}{C_L/C_D} \tag{7.12}$$

$$tan\theta_{AREND} = \frac{1}{17.45} \tag{7.13}$$

$$\theta_{AREND} = 3.28° \tag{7.14}$$

$$tan\theta_{NELD} = \frac{1}{19.16} \tag{7.15}$$

$$\theta_{NELD} = 2.99° \tag{7.16}$$

From the above calculations it was concluded that the glide angle decreases by approximately 10%.

7.4.4 Power required

Power required to maintain unaccelerated steady level flight is defined as follows:

$$P_R = T_R V \tag{7.17}$$

$$P_R = \frac{W}{C_L/C_D} V \tag{7.18}$$

$$\frac{P_{R,NELD}}{P_{R,AREND}} = \frac{\frac{W_{NELD}}{C_{L,NELD}/C_{D,NELD}}}{\frac{W_{AREND}}{C_{L,AREND}/C_{D,AREND}}} \tag{7.19}$$

Assuming the weight is the same for both configurations (even though we know that the NELD configuration is at least 10% lighter and is designed for full load capacity of $20kg$), this gives us purely aerodynamic performance gains.

$$\frac{P_{R,NELD}}{P_{R,AREND}} = \left(\frac{\left(\frac{C_{L,AREND}}{C_{D,AREND}} \right)}{\left(\frac{C_{L,NELD}}{C_{D,NELD}} \right)} \right) \tag{7.20}$$

$$\frac{P_{R,NELD}}{P_{R,AREND}} = \frac{17.45}{19.16} \tag{7.21}$$

$$\frac{P_{R,NELD}}{P_{R,AREND}} = 0.91 \tag{7.22}$$

It is concluded that the power required for NELD is 9% less when compared to AREND for carrying the same weight.

7.4.5 Turning radius and turning rate

Turning radius and turning rate are important for manoeuver. The UAV with low turning radius and high turning rate has an advantage. A nearly level coordinated turn, with small climb angle approximations can be calculated using the following equations:

$$R_T = \frac{L}{0.5\rho g C_L S \sqrt{(L/W)^2 - 1}} \tag{7.23}$$

$$\omega = \frac{g\left(\sqrt{(L/W)^2 - 1}\right)}{V} \tag{7.24}$$

Table 7.1: Comparison of turning radius and turning rate for AREND and NELD configurations.

UAV	Turning radius (m)	Turning rate ($^\circ/s$)
AREND	142	8.1
NELD	108	10.7

A significant change is seen in the turning radius and turning rate due to generation of lift at cruise condition in Table 7.1. The turning radius decreases by approximately 32% and the turning rate increases by $\approx$ 32%. It is primarily due to increase in the lift to weight ratio of NELD.

7.5 Conclusion

The AREND and NELD comparison shows that the NELD configuration does increase the efficiency of the configuration by 9.87% due to cruise point optimization and the removal of the booms and empennage. Table 7.2 compares all the performance parameters. NELD stalls much earlier as compared to AREND due to the high twist distribution on the wing. Overall stability of NELD is better except in yaw which can be addressed through winglets. The range is directly proportional to aerodynamic efficiency but due to the added weight benefits the range can be improved by upto 22%. NELD's stall speed is greater, which means it cannot fly at low speeds like AREND, reducing its operating speed range. NELD glides at a lower angle (glides further), requires 10% less power, and can turn 32% quicker than AREND. A smaller turning radius facilitates manoeuvrability.

Table 7.2: Comparison of AREND and NELD parameters.

Parameters	AREND	NELD
Efficiency	*	+9.87%
Stall	12°	5°
Drag	*	-6.74%
$C_{m\alpha}$	*	+
$C_{n\beta}$	*	-
$C_{l\beta}$	*	+
Range	*	+10% but can be upto +22%
Stall speed	*	+15%
Glide angle	*	-10%
Power required	*	-9%
Turning rate	*	+32%
Turning radius	*	-32%

It can be concluded that the NELD configuration is better than AREND in overall stability and performance at cruise. The NELD configuration is effectively a result of a cruise point optimization study, as its performance becomes worse with increasing angle of attack. It was observed that the NELD configuration is not very robust but highly optimal at the cruise point. It does however, provide some weight reduction. We cannot make a strong recommendation for NELD yet due to lack of wind tunnel or fight test results.

8 Conclusions and future work

8.1 Conclusions

An alternative wing-body-tail configuration was proposed by Huyssen et al. (2012) inspired from bird wings, which are stable and do not require a tail section with vertical and horizontal control surfaces. This new configuration can remove the need for an empennage and hence, reduce structural weight and drag. These two aspects can greatly increase fuel efficiency and aerodynamic performance. The aim of this project was to redesign the AREND UAV using Prandtl's 1933 approach as the basis for wing design and to quantify potential benefits in flight dynamics and aerodynamic performance. In doing so, a tailless configuration (NELD) for the AREND UAV was developed.

A computational domain size with the relevant boundary conditions was established for the study. A validated mesh was adopted for the relatively complex geometry. A benchmark CFD study was conducted on the NACA0012 airfoil and wing geometries at $Re = 10^5$ similar to the two configurations. A steady, incompressible RANS with $SSTk-\omega$ turbulence model including $\gamma - Re_\theta$ transition model was used. The steady state RANS simulations was able to predict the aerodynamic flow features to reasonable certainty. In some cases where separation takes place, certainty is less.

Prandtl's 1933 wing design approach (NELD) was adopted to develop an alternative wing that satisfies the AREND performance targets. The MH 45 airfoil was selected for the NELD wing design. A sweep of 15° was chosen to provide a static margin of 5.42% when CG was set at 100% MAC and 95.43% when the CG at 10% MAC which gives a wide CG range.

CFD data was compared with AVL and the difference was under 10% before stall. The AREND UAV undergoes wing trailing edge stall that leads to the UAV exhibiting tip stall behaviour starting at $\alpha = 12°$. The NELD configuration undergoes leading edge separation at $\alpha = 6°$ which, leads to stall due to the thin MH45 airfoil. Stall begins inboard at $2y/b = 0.35$ and then spreads towards the root and tip. NELD stalls substantially sooner than AREND owing to the wing's strong twist distribution.

Upwash was seen in the modified LLT at $2y/b = 0.70$, while it was observed in the CFD at $2y/b = 0.85$, suggesting the existence of induced thrust as anticipated and shown by Prandtl (1933) and the Horten Brothers (1984), respectively. The CFD simulations were for steady state conditions only, so there would be uncertainty in results at high α where unsteady effects are expected.

The NELD configuration improved the aerodynamic efficiency by 9.87% due to cruise point optimization and the removal of the booms and empennage. Range is directly related to aerodynamic efficiency, although range may be increased by up to 22% with the extra weight savings. NELD glides at a lower angle (glides longer), consumes 10% less energy, and turns 32% faster than AREND. A smaller turning radius facilitates manoeuvrability. The NELD configuration also exhibits proverse yaw and therefore, can indeed perform a coordinated turn. NELD also has a higher stall speed, which means it cannot fly at low speeds like AREND, limiting its operating speed range. NELD is more stable in general, except for yaw, which can be addressed through winglets.

It can be concluded that the NELD configuration is better than AREND in overall stability and performance at cruise. The NELD configuration serves as a cruise point optimization as its performance becomes worse with increasing α. It was observed that the NELD configuration is not very robust but highly optimal at the cruise point. A strong recommendation for NELD cannot be made due to lack of wind tunnel or fight test results. From a practical perspective, the NELD wing has the potential to enable further weight saving, ease of transportation due to reduction of system components and a wider CG range.

8.2 Recommendations for future work

Wind tunnel or flight tests should be conducted on the NELD UAV to validate the CFD results. This study concentrated only on cruise aerodynamic performance and used steady-state models in both CFD and AVL. Thus, future research should concentrate on non-cruise flying situations and on unsteady aerodynamic features, including propeller effects. Aspects such as dynamics during manoeuvers and when the UAV is subjected to atmospheric disturbances were not assessed here but should also be investigated.

Fuselage geometry needs to be optimized to avoid local separation zones, and minimize wing fuselage interaction. An aerodynamic cowling can be used to reduce the wake. Preference should be given to airfoils with a high c_l and higher stall angles, whereas thin airfoils should be avoided owing to leading edge stall. Longitudinal static stability may be obtained even if C_{m0} is not close to zero, since a little amount of sweep can assist in stabilizing $C_{m\alpha}$. A winglet must be designed to increase yaw stability.

The sensitivity of the twist bounds and the removal of the span constraint should be investigated, which could yield further aerodynamic benefits as claimed by Prandtl or might lead to a profile with undesirable stall characteristics.

References

Agenbag, D.S., Theron, N.J., Huyssen, R.J., 2009. Pitch handling qualities investigation of the tailless gull-wing configuration. Journal of Aircraft 46, 683–691.

Almutairi, J.H., Jones, L.E., Sandham, N.D., 2010. Intermittent bursting of a laminar separation bubble on an airfoil. AIAA journal 48, 414–426.

Anderson Jr, J.D., 2010. Fundamentals of aerodynamics. Tata McGraw-Hill Education.

ASME, V., 2009. Standard for verification and validation in computational fluid dynamics and heat transfer. American Society of Mechanical Engineers .

Bansal, R.K., 2005. Fluid Mechanics and Hydraulic Machines. Laxmi Publication.

Bowers, A.H., Murillo, O.J., Jensen, R.R., Eslinger, B., Gelzer, C., 2016. On wings of the minimum induced drag: Spanload implications for aircraft and birds. Technical Report.

Bragado Aldana, E., Lone, M.M., 2019. Aerodynamic and flight dynamic study of non-elliptic wing lift distributions, in: AIAA Scitech 2019 Forum, p. 0820.

CD-Adapco, 2016. Instruction Manual of Star CCM+ 11.02.009.

Cebeci, T., 2004. Analysis of Turbulent Flows. Oxford.

Cook, M.V., 2013. Flight Dynamics Principles. Elsevier.

Denisov, V.E., Bolsunovsky, A.L., 1998. Recent investigations of the very large passenger blended wing body aircraft. ICAS .

Drela, M., 1989. XFOIL An Analysis and design system for Low Reynolds Number Airfoils. 1-12, Springer Berlin Heidelberg.

Horten, R., Horten, W., 1984. Towards the theory of Flying Wings. Technical Report.

Huyssen, R.J., Spedding, G.R., Mathews, E.H., Liebenberg, L., 2012. Wing body circulation control by means of a fuselage trailing edge. Journal of Aircraft .

Katz, J., Plotkin, A., 2001. Low-Speed Aerodynamics. Cambridge University Press.

Kier, T.M., 2005. Comparison of unsteady aerodynamic modelling methodologies with respect to flight loads analysis. AIAA-Atmospheric Flight Mechanics Conference .

Koster, J.N., Buysse, A., Smith, L., Huyssen, J., Hotchkiss, J., Malangoni, J., Schneider, J., 2016. Arend: A sensor aircraft to support wildlife rangers, in: 57th AIAA/ASCE/AHS/ASC Structures, Structural Dynamics, and Materials Conference, p. 0827.

Langtry, R.B., 2006. A Correlation-Based Transition Model Using Local Variables for Unstructured Parallelized CFD Codes. Ph.D. thesis. University of Stuttgart.

McCormick, B.W., 1995. Aerodynamics, aeronautics, and flight mechanics .

McLean, D., 2012. Understanding aerodynamics: arguing from the real physics. John Wiley & Sons.

Menter, F.R., 1994. Two-equation eddy-viscosity turbulence models for engineering applications. AIAA journal 32, 1598–1605.

Menter, F.R., Langtry, R.B., Likki, S., Suzen, Y., Huang, P., Völker, S., 2006. A correlation-based transition model using local variables - part i: model formulation. Journal of Turbomachinery 128, 413–422.

Modise, A., 2021. The department report back on rhino poaching in South Africa in 2020. Technical Report. Department of forestry, fisheries & the environment.

Molewa, B.E.E., 2021. Question 2761. Technical Report. Department of Environmental Affairs.

Nickel, K., Wohlfahrt, M., 1994. Tailless aircraft in theory and practice. AIAA.

Pereira, E., 2021. Impact report 2021. Technical Report. Save the Rhino.

Phillips, W.F., 2004. Mechanics of flight. John Wiley & Sons.

Prandtl, L., 1923. Applications of modern hydrodynamics to aeronautics.[in two parts] .

Prandtl, L., 1932. Uber tragflugel kleinsten induzierten widerstandes. Zeitschrift fur Flugtecknik und Motorluftschiffahrt .

Prandtl, L., 1935. On airfoils with minimum induced drag - translated by a.i.t, air ministry. Journal of aeronautical engineering and engine aviation , 10.

Raymer, D.P., 2012. Aircraft design: a conceptual approach (aiaa education series). Reston, Virginia .

Roache, R.J., 1997. Quantification of uncertainty in computational fluid dynamics. Annual Review of Fluid Mechanics 29, 123–160.

Rom, J., 2012. High angle of attack aerodynamics: subsonic, transonic, and supersonic flows. Springer Science & Business Media.

Smith, L., 2017. Investigation of a modified low-drag body for an alternative wing-body-tail configuration. Ph.D. thesis. University of Pretoria.

Smith, L., Craig, K.J., Meyer, J.P., Spedding, G.R., 2017. Modifying low-drag bodies to generate lift: a computational study. Journal of Aircraft 54, 1150–1161.

Smith, L., Craig, K.J., Meyer, J.P., Spedding, G.R., 2019. Numerical investigation of the aerodynamic performance for an alternative wing-body-tail configuration. Journal of Aircraft 56.

Smith, L., Koster, J.N., Schneider, J., 2018. Experience with international collaborative aircraft design education: Arend uav, in: 31st Congress of the International Council of the Aeronautical Sciences.

Tank, J., Smith, L., Spedding, G.R., 2017. On the possibility (or lack thereof) of agreement between experiment and computation of flows over wings at moderate reynolds number. Interface focus 7, 20160076.

Torenbeek, E., 2013. Advanced aircraft design: conceptual design, analysis and optimization of subsonic civil airplanes. John Wiley & Sons.

White, F.M., 2011. Fluid mechanics. 7 ed., Tata McGraw-Hill Education.